

Научном већу Института за физику Београд  
Београд

Предмет: реизбор у звање истраживач-сарадник

### Молба

Молим да ми се одобри покретање поступка за реизбор у звање истраживач-сарадник.

У прилогу достављам:

- мишљење руководиоца пројекта
- уверење о завршеним дипломским студијама
- потврду о уписаним докторским студијама
- стручну биографију
- списак и копије објављених радова
- одлуку о избору у истраживачко звање
- одлуку о пријављеној теми

у Београду,

19.12.2016. год.

С поштовањем,

Наташа Томић, истраживач-сарадник

*Наташа Томић*

## Мишљење руководиоца пројекта

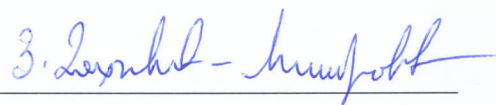
Наташа Томић је од 1.09.2011. године запослена у Центру за физику чврстог стања и нове материјале Института за физику Београд, у Београду, где ради на пројекту ON 171032 “Физика наноструктурних оксидних материјала и јако корелисаних система” које финансира Министарство за просвету и науку Републике Србије.

Пошто испуњава све услове предвиђене Правилником за изборе у научно - истраживачка звања, сагласна сам са покретањем поступка за реизбор Наташе Томић.

За састав комисије за избор Наташе Томић у звање истраживач-сарадник предлажем:

1. др Зорана Дохчевић-Митровић, научни саветник Института за физику Београд, Београд
2. др Соња Ашкрабић, научни сарадник Института за физику Београд, Београд
3. др Никола Цвјетићанин, редовни професор на Факултету за физичку хемију, Београд

Руководилац пројекта



др Зорана Дохчевић-Митровић,

у Београду, 19.12.2016.

научни саветник Института за физику Београд

РЕПУБЛИКА СРБИЈА



УНИВЕРЗИТЕТ У БЕОГРАДУ  
ФАКУЛТЕТ ЗА ФИЗИЧКУ ХЕМИЈУ

# ДИПЛОМА

О СТЕЧЕНОМ ВИСОКОМ ОБРАЗОВАЊУ

## Томини Миодрага Наташа

РОЂЕНА 20-II-1981. ГОДИНЕ У БЕОГРАДУ, САВСКИ БЕНАЦ,  
СРБИЈА, УПИСАНА 2001/2002 ШКОЛСКЕ ГОДИНЕ,  
А ДАНА 14. ФЕБРУАРА 2011. ГОДИНЕ, ЗАВРШИО-ЛА ЈЕ СТУДИЈЕ НА  
ФАКУЛТЕТУ ЗА ФИЗИЧКУ ХЕМИЈУ

СА ОПШТИМ УСПЕХОМ 9,60 (ДЕСЕТ И 60/100) У ТОКУ СТУДИЈА И ОЦЕНОМ  
10 (ДЕСЕТ) НА ДИПЛОМСКОМ ИСПИТУ.

НА ОСНОВУ ТОГА ИЗДАЈЕ МУ-ЈОЈ СЕ ОВА ДИПЛОМА О СТЕЧЕНОМ ВИСОКОМ  
ОБРАЗОВАЊУ И СТРУЧНОМ НАЗИВУ

**ДИПЛОМИРАНИ ФИЗИКОХЕМИЧАР**

РЕДНИ БРОЈ ИЗ ЕВИДЕНЦИЈЕ О ИЗДАТИМ ДИПЛОМАМА 232011

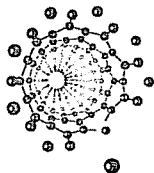
У БЕОГРАДУ, 14-II-2011. ГОДИНЕ

ДЕКАН

проф. др Милан Станић

РЕКТОР

проф. др Франко Кузмановић



Република Србија  
Универзитет у Београду  
Факултет за физичку хемију  
Д.Бр.2010/0320  
Датум: 08.12.2016. године

На основу члана 161 Закона о општем управном поступку и службене евиденције издаје се

## УВЕРЕЊЕ

**Томић (Миодраг) Наташа**, бр. индекса 2010/0320, рођена 20.02.1981. године, Београд, Београд-Савски Венац, Република Србија, уписана школске 2016/2017. године, у статусу: самофинансирање; тип студија: докторске академске студије; студијски програм: Физичка хемија.

Према Статуту факултета студије трају (број година): три године.  
Рок за завршетак студија: у двоструком трајању студија.

Ово се уверење може употребити за регулисање војне обавезе, издавање визе, права на дечији додатак, породичне пензије, инвалидског додатка, добијања здравствене књижице, легитимације за повлашћену возњу и стипендије.



Овлашћено лице факултета

## Стручна биографија



Наташа Томић је рођена 20.02.1981. године у Београду, општина Савски Венац, Република Србија. Основну школу и гимназију (V београдска гимназија) је похађала у Београду. Основне студије на Факултету за Физичку Хемију, Универзитет у Београду, Србија уписала је 2001. године. У фебруару 2011. године је дипломирала са просечном оценом 9.60 и оценом 10 на дипломском испиту са темом “Примена (0,0) спектралне траке Свановог система за одређивање температуре гаса”. У марту 2011. године је уписала докторске студије на Факултету за Физичку Хемију, Универзитет у Београду, Србија. Од 1.09.2011. године је запослена у Центру за физику чврстог стања и нове материјале Института за физику Београд у Београду, као истраживач-приправник на пројекту ON 171032 “Физика наноструктурних оксидних материјала и јако корелисаних система”. У марту 2014. године је изабрана у звање истраживач - сарадник. Од 2013. до 2015. године је учествовала на билатералном пројекту са Италијом - "Нове оксидне наноструктуре за пречишћавање воде", под руководством др Зоране Дохчевић - Митровић.

У Београду,

19.12.2016.

## Библиографија

### Радови у врхунским међународним часописима (M21):

1. M. Grujić-Brojčin, S. Armaković, **N. Tomić**, B. Abramović, A. Golubović, B. Stojadinović, A. Kremenović, B. Babić, Z. Dohčević-Mitrović, M. Šćepanović, *Surface modification of sol-gel synthesized TiO<sub>2</sub> nanoparticles induced by La-doping*, Materials Characterization 88 (2014) 30-41.
2. A. Golubović, **N. Tomić**, N. Finčur, B. Abramović, I. Veljković, J. Zdravković, M. Grujić-Brojčin, B. Babić, B. Stojadinović, M. Šćepanović, *Synthesis of pure and La-doped anatase nanopowders by sol-gel and hydrothermal methods and their efficiency in photocatalytic degradation of alprazolam*, Ceramics International 40 (2014) 13409-13418.
3. **Nataša M. Tomić**, Zorana D. Dohčević-Mitrović, Novica M. Paunović, Dušan Ž. Mijin, Nenad D. Radić, Boško V. Grbić, Sonja M. Aškračić, Biljana M. Babić, and Danica V. Bajuk-Bogdanović, *Nanocrystalline CeO<sub>2-δ</sub> as Effective Adsorbent of Azo Dyes*, Langmuir 30 (2014) 11582-11590.
4. **N. Tomić**, M. Grujić-Brojčin, N. Finčur, B. Abramović, B. Simović, J. Krstić, B. Matović, M. Šćepanović, *Photocatalytic degradation of alprazolam in water suspension of brookite type TiO<sub>2</sub> nanopowders prepared using hydrothermal route*, Materials Chemistry and Physics 163 (2015) 518-528.
5. Zorana Dohčević-Mitrović, Stevan Stojadinović, Luca Lozzi, Sonja Aškračić, Milena Rosić, **Nataša Tomić**, Novica Paunović, Saša Lazović, Marko G. Nikolić, Sandro Santucci, *WO<sub>3</sub>/TiO<sub>2</sub> composite coatings: Structural, optical and photocatalytic properties*, Materials Research Bulletin 83 (2016) 217-224.

### Зборници саопштења са међународних научних скупова:

### Саопштења са међународних скупова штампана у изводу (M34):

1. **Nataša Tomić**, Aleksandar Golubović, Marko Radović, Jelena Tanasijević, Ivana Veljković, *Influence of La<sup>3+</sup> -dopant on anatase nanopowders synthesized by sol-gel and hydrothermal methods*, First International Conference on Processing, characterization and application of nanostructured materials and nanotechnology Nano Belgrade, Belgrade, Serbia, P-15, page 93, September 2012.

2. M. Radović, B. Stojadinović, **N. Tomić**, I. Veljković, S. Aškrabić, A. Golubović, B. Matović, Z. Dohčević-Mitrović, *Investigation of defect electronic states in CeO<sub>2</sub> nanocrystals synthesized by SPRT, Hydrothermal and Precipitation method*, 2<sup>nd</sup> Conference of The Serbian Ceramic Society, Belgrade, Serbia, O-3, page 42, June 2013.
3. **Nataša Tomić**, Nina Finčur, Ivana Veljković, Maja Šćepanović, Aleksandar Golubović, Biljana Abramović, *The efficiency of pure and La-doped anatase nanopowders synthesized by sol-gel and hydrothermal method in photocatalytic degradation of alprazolam*, 2<sup>nd</sup> Conference of The Serbian Ceramic Society, Belgrade, Serbia, P-20, page 71, June 2013.
4. Sasa Lazovic, Dejan Maletic, **Natasa Tomić**, Gordana Malovic, Uros Cvelbar, Zorana Dohcevic-Mitrovic, Zoran LJ. Petrovic, *Decolorization of azodyes using the atmospheric pressure plasma jet*, 66th Annual Gaseous Electronics Conference, Princeton, New Jersey, CT1 68, page 29, September-October, 2013.
5. **Nataša Tomić**, Sonja Aškrabić, Vinicius Dantas de Araújo, Marijana Milićević, Saša Lazović, Zoran Petrović, Zorana Dohčević-Mitrović, *Efficient photocatalytic degradation of azo-dye RO16 by pure and Eu-doped Pr(OH)<sub>3</sub> nanostructures*, 3<sup>rd</sup> Conference of The Serbian Society for Ceramic Materials, Belgrade, Serbia, P-14, page 89, June (15-17), 2015.

На основу члана 82. Закона о научноистраживачкој делатности ("Службени гласник Републике Србије", број 110/2005, 50/2006 - испр. и 18/2010), члана 33. тачка 5. Статута Института за физику и захтева који је поднела

НАТАША ТОМИЋ

на седници Научног већа Института за физику одржаној 18.03.2014. године,  
донета је

## ОДЛУКА О СТИЦАЊУ ИСТРАЖИВАЧКОГ ЗВАЊА

НАТАША ТОМИЋ

стиче истраживачко звање  
*Истраживач сарадник*

### ОБРАЗЛОЖЕЊЕ

Наташа Томић је 30.01.2014. године поднела захтев за стицање истраживачког звања истраживач сарадник. Научно веће Института за физику је на седници одржаној 04.02.2014. године образовало Комисију за спровођење поступка у саставу др Зорана Дохчевић Митровић, научни саветник у Институту за физику, др Мирјана Грујић Бројчин, виши научни сарадник у Институту за физику и проф. др Никола Цвјетићанин, ванредни професор на Факултету за физичку хемију, Универзитет у Београду. Научно веће је на седници од 18.03.2014. године утврдило да именована испуњава услове из члана 70. став 3. Закона о научноистраживачкој делатности за стицање истраживачког звања **истраживач сарадник**, па је одлучило као у изреци ове одлуке.

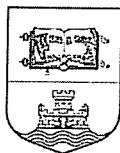
Одлуку доставити подносиоцу, архиви Института за физику, кадровској служби Института за физику и рачуноводственој служби Института за физику.

  
Председник Научног већа  
др Љубинко Игњатовић



  
Директор Института за физику  
др Александар Белић





## УНИВЕРЗИТЕТ У БЕОГРАДУ

Адреса: Студентски трг 1, 11000 Београд, Република Србија  
Тел.: 011 3207400; Факс: 011 2638818; E-mail: officebu@rect.bg.ac.rs

ВЕЋЕ НАУЧНИХ ОБЛАСТИ  
ПРИРОДНИХ НАУКА

Београд, 15.09.2016.  
02-07 Број: 61206-4301/2-16  
МЦ

На основу члана члана 47. став 5. тачка. 3. Статута Универзитета у Београду ("Гласник Универзитета у Београду", број 186/15-пречишћени текст и 189/16) и чл. 14. – 21. Правилника о већима научних области на Универзитету у Београду ("Гласник Универзитета у Београду", број 134/07, 150/09, 158/11, 164/11 и 165/11), а на захтев Факултета за физичку хемију, број: 889/2 од 12.07.2016. године, Веће научних области природних наука, на седници одржаној 15.09.2016. године, донело је

### О Д Л У К У

ДАЈЕ СЕ САГЛАСНОСТ на предлог теме докторске дисертације НАТАШЕ ТОМИЋ, под називом: „Адсорпциона и фотокаталитичка својства наноматеријала на бази церијум(IV)-оксида и титан(IV)-оксида“.

ЗАМЕНИК ПРЕДСЕДНИКА ВЕЋА

Проф. др Душан Сладић

Доставити:

- Факултету
- архиви Универзитета

Available online at [www.sciencedirect.com](http://www.sciencedirect.com)

ScienceDirect

[www.elsevier.com/locate/matchar](http://www.elsevier.com/locate/matchar)

# Surface modification of sol–gel synthesized TiO<sub>2</sub> nanoparticles induced by La-doping

M. Grujić-Brojčin<sup>a,\*</sup>, S. Armačević<sup>b</sup>, N. Tomić<sup>a</sup>, B. Abramović<sup>b</sup>, A. Golubović<sup>a</sup>,  
B. Stojadinović<sup>a</sup>, A. Kremenović<sup>c</sup>, B. Babić<sup>d</sup>, Z. Dohčević-Mitrović<sup>a</sup>, M. Šćepanović<sup>a</sup>

<sup>a</sup>Institute of Physics, University of Belgrade, Pregrevica 118, 11080 Belgrade, Serbia

<sup>b</sup>Department of Chemistry, Biochemistry and Environmental Protection, Faculty of Sciences, University of Novi Sad, Trg D. Obradovića 3, 21000 Novi Sad, Serbia

<sup>c</sup>Faculty of Mining and Geology, Laboratory for Crystallography, University of Belgrade, Đušina 7, 11000 Belgrade, Serbia

<sup>d</sup>Institute of Nuclear Sciences “Vinča”, University of Belgrade, 11001 Belgrade, Serbia

## ARTICLE DATA

### Article history:

Received 3 June 2013

Received in revised form

17 November 2013

Accepted 3 December 2013

### Keywords:

TiO<sub>2</sub> nanopowder

La-doping

STM/STS

Optical spectroscopy

Photocatalysis

## ABSTRACT

The influence of La-doping in the range of 0.5–6.0 mol% on structural and morphological properties of TiO<sub>2</sub> nanopowders synthesized by sol–gel routine has been investigated by XRPD, AFM, EDS and BET measurements, as well as Raman spectroscopy. The XRPD and Raman measurements have revealed the anatase phase as dominant in all nanopowders, with crystallite size decreasing from ~15 nm in pure TiO<sub>2</sub> to ~12 nm in La-doped samples. The BET data suggest that all samples are fully mesoporous, with mean pore diameters in the range of ~6–8 nm. The specific surface area and the complexity of pore structure are greater in doped samples than in pure TiO<sub>2</sub> sample. The spectroscopic ellipsometry has apparently shown that the band gap has been gradually increased with the increase of La content. The STM and STS techniques have been used successfully to evaluate the surface morphology and electronic properties of La-doped nanopowders. All investigated properties have been related to photocatalytic activity, tested in degradation of a metoprolol tartrate salt (0.05 mM), and induced by UV-radiation. All doped samples showed increased photocatalytic activity compared to pure TiO<sub>2</sub>, among which the 0.65 mol% La-doped sample appeared to be the most efficient.

© 2013 Elsevier Inc. All rights reserved.

## 1. Introduction

Among the semiconductors investigated for the purpose of the degradation of pollutants in the water, titanium dioxide (TiO<sub>2</sub>) is the most preferable material for the photocatalytic processes, due to its high photosensitivity, non-toxic nature, large band gap and stability ([1] and the references therein). In recent research, doping TiO<sub>2</sub> with lanthanum (La<sup>3+</sup>) ions has been found to improve the activity of TiO<sub>2</sub> photocatalysts [2–4]. The reasons for such improvement in photocatalytic activity have been generally related to increasing surface area and pore

volume, capacity for adsorption of organic compounds, as well as suppressing electron–hole recombination rates in La-doped TiO<sub>2</sub> photocatalyst during the photocatalytic reaction [2–4]. However, the variety of experimental conditions, sample preparation and determination of photoreactivity, as well as a lack of information on electronic structure, still make it difficult to explain the formation mechanism of lanthanum oxides and the changing of band gap energy with La-doping [5,6]. Namely, most of the literature is in agreement with the fact that La-doping is able to red shift the adsorption edges of TiO<sub>2</sub> to longer wavelengths, usually attributed to the La<sup>3+</sup> replacing Ti<sup>4+</sup>

\* Corresponding author at: Institute of Physics, University of Belgrade, Pregrevica 118, 11080 Belgrade, Serbia. Tel.: +381 113713023; fax: +381 113162190.

E-mail address: [myramyra@ipb.ac.rs](mailto:myramyra@ipb.ac.rs) (M. Grujić-Brojčin).

ions in the TiO<sub>2</sub> lattice [6,7], but some recent studies have reported either a blue shift [8] or an absence of any shift [6]. This may be due to different synthesis conditions, and more insight is needed to determine which conditions are responsible for the specific behavior of the adsorption edge.

The sol-gel process appears to be the most popular doping technique since it is a low-cost, simple, and versatile method that can be easily manipulated. However, this process, followed by calcination at high temperature, can allow for lanthanum ions either to form oxides dispersed on the surface of the TiO<sub>2</sub> nanoparticles, or to incorporate in the titania lattice, as a less frequent outcome [7]. Therefore one of the goals of this research was to estimate which form of La<sup>3+</sup> ions is dominant in TiO<sub>2</sub> nanopowders synthesized under the specified sol-gel synthesis conditions.

The TiO<sub>2</sub> mesoporous nanopowders, pure and doped with La<sup>3+</sup> in the range of 0.5 to 6.0 mol% have been prepared by sol-gel routine using titanium tetrachloride (TiCl<sub>4</sub>) as a precursor [9–11]. The effects of La-doping on the crystallite size, structure and phase composition of the synthesized samples have been investigated by X-ray powder diffraction (XRPD), energy-dispersive X-ray spectroscopy (EDS), and Raman scattering measurements.

The morphological properties have been studied by atomic force microscopy (AFM) and the Brunauer-Emmett-Teller (BET) measurements. The BET data have been analyzed by BJH (Barrett-Joyner-Halenda) and CPSM (corrugated pore structure model) methods to estimate the specific surface area and pore size distribution. Also, the pore structure tortuosity factor, as a feature of primary importance in catalysis, has been calculated by CPSM to obtain the information on the connectivity among the pores, which is essential to describe transport dynamics in porous media, and consequently determine the time of the catalytic reaction [12,13].

The electronic properties of nanopowders have been studied by scanning tunneling spectroscopy (STS) and spectroscopic ellipsometry (SE), to reveal the influence of doping on band gap energy and the energies of electronic transitions.

Experimentally observed structural, morphological and surface modifications of TiO<sub>2</sub> nanoparticles induced by La-doping have been related to the photocatalytic activity under ultraviolet (UV) irradiation. The efficiency of La-doped TiO<sub>2</sub> nanopowders have been tested in photocatalytic degradation of metoprolol tartrate salt, and compared to the performance of pure nanopowder under the same conditions [10,11,14]. Metoprolol tartrate salt (1-[4-(2-methoxyethyl)phenoxy]-3-(propan-2-ylamino)propan-2-ol tartrate (2:1), CAS no. 56392-17-7, (C<sub>15</sub>H<sub>25</sub>NO<sub>3</sub>)<sub>2</sub> C<sub>4</sub>H<sub>6</sub>O<sub>6</sub>, M<sub>r</sub> = 684.81, MET) is commonly used as selective β<sub>1</sub>-blocker in treatment of cardiovascular diseases. Its continuous input and persistence in the aqueous system, even in trace concentrations, may result in an emerging environmental pollution [15].

## 2. Experimental Details

### 2.1. Synthesis

Anatase nanoparticles have been prepared by using a sol-gel procedure with TiCl<sub>4</sub> (99.0% pure, Merck) as a titanium precursor.

The 5 ml of TiCl<sub>4</sub> was dissolved in 150 ml of distilled water under vigorous stirring on the ice-bath. In order to obtain the hydrogel, the aqueous solution of ammonium hydroxide (29%, Carlo Erba) has been added under careful control of the pH value of the solution (9.3). After aging in the mother liquor for 5 h, as-prepared hydrogel has been filtered and washed out with distilled water until complete removal of chloride ions. Obtained hydrogel has been converted to alcogel by repeated exchange with anhydrous ethanol for several times. To convert into nanoparticles, the alcogel was placed in a vessel, dried at 280 °C and calcined at a temperature of 550 °C for 7 h [9]. Also, an appropriate amount of LaCl<sub>3</sub>·7H<sub>2</sub>O (Merck) had been dissolved in water prior to the hydrolysis of TiCl<sub>4</sub>, to obtain La-doped TiO<sub>2</sub> nanoparticles. The pure TiO<sub>2</sub> nanopowder and those doped with 0.5, 0.65, 1, 2, 3, 4, 5, and 6 mol% of La are labeled as TL(0), TL(0.5), TL(0.65) and from TL(1) to TL(6), respectively.

### 2.2. Characterization Methods

Powder X-ray diffraction has been used for the identification of crystalline phases, quantitative phase analysis and estimation of crystallite size and strain. The XRPD patterns for pure titanium dioxide nanopowder and those doped with 0.65 and 1 mol% of lanthanum ions have been collected on a Philips diffractometer (PW1710) employing Cu K<sub>α1,2</sub>, in the scanning range of 2θ between 20 and 80° with the step size of 0.06° and the counting time of 41 s/step. The patterns of the samples doped with higher La concentration have been collected in the same range by using a Stoe Stadi MP diffractometer (Cu K<sub>α1</sub> radiation, primary beam Ge monochromator, linear PSD detector, Bragg-Brentano geometry), at every 0.01°, with a counting time of 80 s/step. The Fullprof computer program was used for the structure refinements, quantitative phase analysis and estimation of average crystallite sizes and strains [16]. For size-strain analysis the instrumental resolution function was obtained by parameterizing the profiles of the diffraction pattern of a LaB<sub>6</sub> (NIST SRM660a) standard specimen.

Composition/quality of TiO<sub>2</sub> has been analyzed on a SEM (JEOL JSM-6460LV, with the operating voltage of 20 keV) equipped with an EDS (INCAx-sight) detector and “INAX-stream” pulse processor (Oxford Instruments).

Non-contact atomic force microscopy (NC-AFM) measurements were carried out using an Omicron B002645 SPM probe VT AFM 25.

The porous structure of catalysts has been evaluated from adsorption/desorption isotherms of N<sub>2</sub> measured on TiO<sub>2</sub> samples, at –196 °C, using the gravimetric McBain method. The main parameters of the porosity such as specific surface area and pore volume have been estimated by BET method and α<sub>s</sub>-plot ([17] and references therein). The pore size distributions have been estimated from experimental nitrogen sorption data by BJH and CPSM methods [11,18].

The Raman scattering measurements of TiO<sub>2</sub> samples were performed in the backscattering geometry at room temperature in the air using a Jobin-Yvon T64000 triple spectrometer, equipped with a confocal microscope and a nitrogen-cooled charge coupled device detector. The spectra have been excited by a 514.5 nm line of Ar<sup>+</sup>/Kr<sup>+</sup> ion laser with an output power of less than 5 mW to avoid local heating due to laser irradiation.

The ellipsometric spectra of the TiO<sub>2</sub> nanopowders were measured using a SOPRA GES-5 variable angle ellipsometer in rotating polarizer configuration. The data were collected at room temperature, in the range from 1.5 to 6.5 eV with a resolution of 0.02 eV, for the incidence angle of 65°. Bulk calculations have been used to analyze the ellipsometric spectra and determine the dielectric functions of synthesized anatase nanopowders from measured SE data. The critical point (CP) method [19–21] has been applied to identify and evaluate the energy of the electronic transitions in nanopowders.

Scanning tunneling microscopy and spectroscopy (STM/STS) were employed to study the formation of La<sub>2</sub>O<sub>3</sub> on an anatase nanoparticle surface. The measurements were performed at room temperature using the Omicron VT UHV system. Topography images were taken at several bias voltages in the range of 2.0–2.3 V and set-point currents with typical value of 200 pA, or less. Spectroscopic data were acquired at various locations of the tungsten tip above chosen nanoparticles in the range of ±4 V. The data represent an average of 100 measurements performed consecutively.

### 2.3. Measurements of Photocatalytic Activity

The photocatalytic activity of the TiO<sub>2</sub> powders doped with different amounts of La was evaluated by the degradation of the solution of metoprolol tartrate salt (≥99%, Sigma-Aldrich). The photocatalytic degradation was carried out as described in our previous research [10,11]. The initial MET concentration was 0.05 mM and the TiO<sub>2</sub> loading was 1.0 mg ml<sup>-1</sup>. All experiments were performed at the natural pH. Kinetics of the MET photodegradation was monitored with liquid chromatography with diode array detection (LC–DAD) at 225 nm (wavelength of MET maximum absorption) [10]. The use of the gradient mode to follow the degradation kinetics of MET was necessary in order to separate the peaks originating from MET and intermediates, and shorten the time of the LC–DAD analysis. In order to determine the reproducibility of the results, at least duplicated runs were carried out for each condition for averaging the results, and reproducibility of kinetic measurements were 3–10%.

## 3. Experimental Results

### 3.1. X-ray Powder Diffraction

The XRPD patterns of pure and some La-doped TiO<sub>2</sub> nanopowders, are shown in Fig. 1. The most intensive diffraction peaks can be ascribed to the anatase crystal structure (JCPDS card 78-2486). Structure refinements have been performed by Rietveld method, and the lattice parameters, unit cell volume, average crystallite size and average strain in anatase are summarized in Table 1. The value of the anatase parameter *a* varies around its reference value (*a*<sub>0</sub> = 0.378479(3) nm), whereas the value of the *c* parameter is slightly smaller than the reference one (*c*<sub>0</sub> = 0.951237(1) nm). The unit cell volume of all samples is also smaller in comparison to the reference value, except in the pure TiO<sub>2</sub>. The structural refinement has revealed that the anatase crystallite size of doped samples is decreased from ~15 nm in pure TL(0) to ~12 nm in La-doped samples, whereas the strain is slightly increased with doping (Table 1).

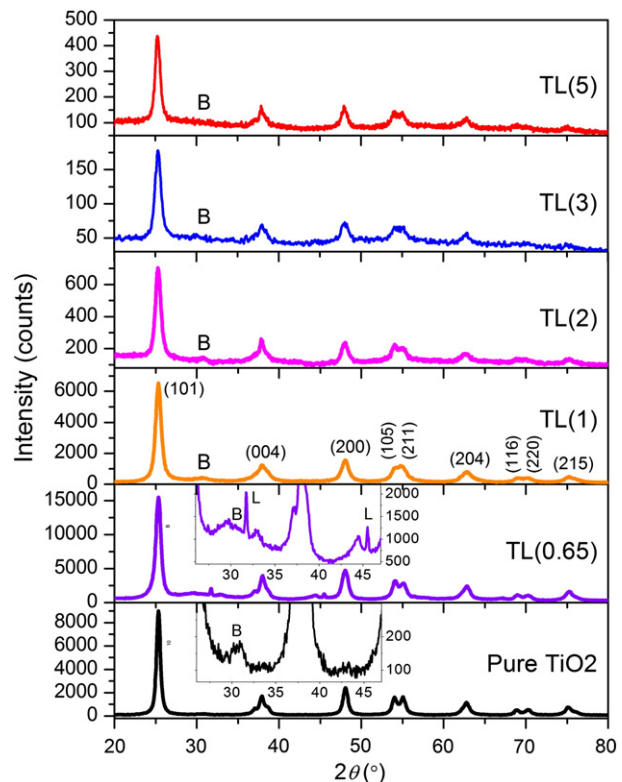


**Fig. 1 – XRPD patterns of pure and selected La-doped TiO<sub>2</sub> nanopowders, with characteristic reflections of anatase phase given in the parentheses. The enlarged parts of diffractograms of the samples TL(0.65) and pure TiO<sub>2</sub> are shown in the insets. Characteristic reflections of brookite and La<sub>2</sub>O<sub>3</sub> are denoted by “B” and “L”, respectively.**

The presence of a low intensity diffraction peak at  $2\theta \approx 30.8^\circ$  (denoted by “B” in Fig. 1), observed in all XRPD patterns, points to the brookite phase (JCPDS card 29-1360). The average crystallite size, the average strain, and the content of brookite phase have been also summarized in Table 1. The small crystallite size (down to 2 nm in TL(0.65)), as well as large values of the average strain in brookite phase indicate that this phase is highly disordered in all the samples. Therefore any attempt to obtain reliable unit cell parameters of brookite during the Rietveld refinement has failed. It also can be seen from Table 1 that brookite content, estimated from quantitative phase analysis, is greater in doped samples. A relatively large error in estimation of brookite content (defined as triple value of standard deviation, Table 1) is a consequence of the very low crystallinity of this phase followed by wide brookite diffraction peaks. Also, the lower intensity of brookite diffraction peaks in comparison to those of anatase, as well as a number of anatase and brookite reflections at very close values of diffraction angle, convoluting to one diffraction maximum, make the estimation of brookite presence even more complicated.

Moreover, very broad peaks at around 13.0, 29.5, 33.0 and 44.0° (as could be noticed from the pattern of the sample TL(0.65) shown in the upper inset of Fig. 1), which probably point to the presence of amorphous TiO<sub>2</sub> phase, as well as low signal intensity and great noise (samples TL(2), TL(3) and TL(5)), are

**Table 1 – The results of the Rietveld analyses (the unit cell parameters and unit cell volume of anatase, average crystallite size and average strain in anatase and brookite phase and content of brookite phase) for pure and La-doped TiO<sub>2</sub> (the values in parentheses represent estimated standard deviations).**

Sample	Anatase					Brookite		
	a (nm)	c (nm)	V (10 <sup>-3</sup> nm <sup>3</sup> )	Crystallite size (nm)	Strain (× 10 <sup>-3</sup> )	Content (%)	Crystallite size (nm)	Strain (10 <sup>-3</sup> )
TL(0)	0.37884(1)	0.94980(5)	136.31(1)	15	3	10(2)	58	17
TL(0.65)	0.37895(2)	0.9485(1)	136.21(2)	12	4	42(5)	2	29
TL(1)	0.37880(2)	0.94780(1)	136.01(2)	10	5	24(3)	26	22
TL(2)	0.37853(2)	0.94908(9)	135.99(2)	12	8	21(1)	12	8
TL(3)	0.37823(6)	0.9471(3)	135.49(5)	12	8	21(4)	12	8
TL(5)	0.37874(3)	0.9485(1)	136.06(2)	12	8	22(2)	12	8

Reference values: a<sub>0</sub> = 0.378479(3) nm, c<sub>0</sub> = 0.951237(1) nm, and V<sub>0</sub> = 136.26(1) (10<sup>-3</sup> nm<sup>3</sup>).

confirming that the crystallinity of synthesized materials is of extremely low degree. It seems that La-doping induces additional disorder in both anatase and brookite phases.

The diffraction peaks at ~31.7 and 45.5°, characteristic for crystalline La<sub>2</sub>O<sub>3</sub>, have been found only in the pattern of the sample doped with 0.65 mol% La (the upper inset in Fig. 1). However, it does not exclude the presence of La-oxide in the

amorphous phase in the samples doped with higher La concentration.

### 3.2. Atomic Force Microscopy

The NC-AFM images of pure, 1 mol% and 6 mol% La-doped TiO<sub>2</sub> samples are shown in Fig. 2. Note that images (a) and (c) are

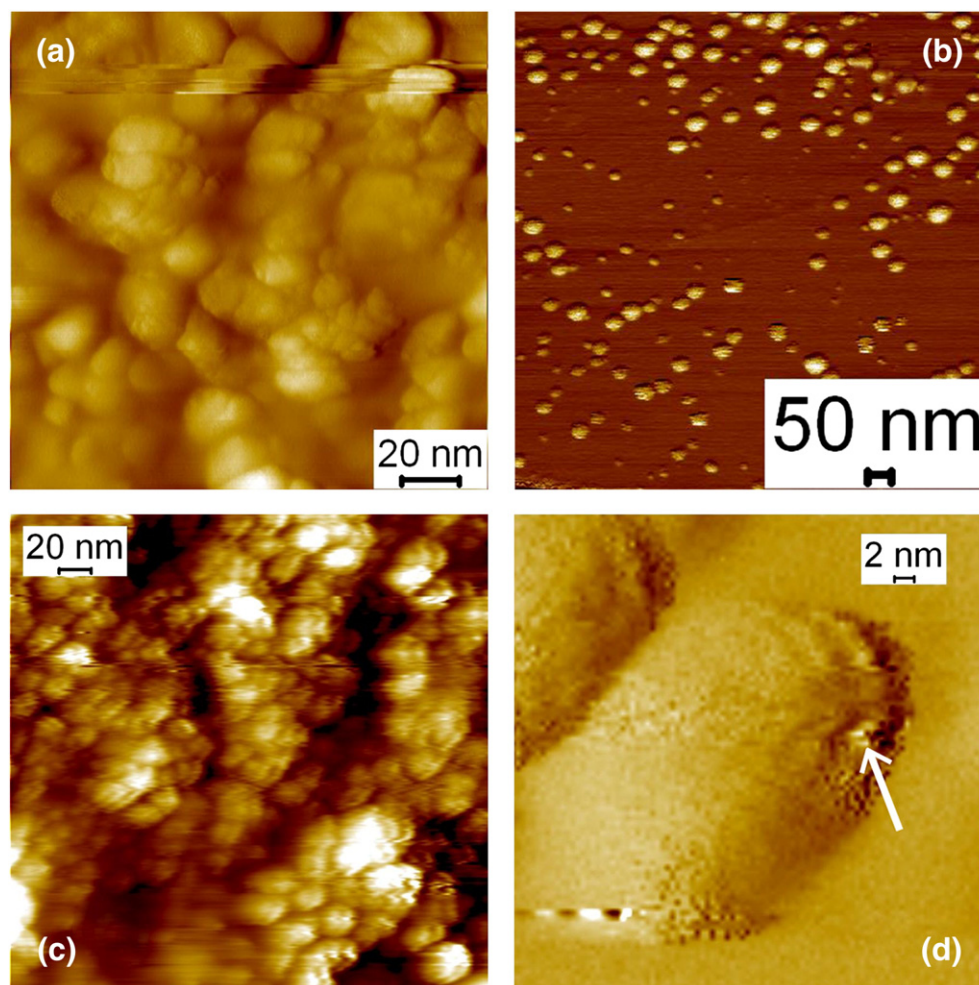


**Fig. 2 – NC-AFM images of pure (a) and La-doped TiO<sub>2</sub> samples: 1 mol% La (b), 6 mol% La (c) and close-up image of the sample with 6 mol% La (d).**

**Table 2 – EDS results for pure and some La-doped TiO<sub>2</sub> nanopowders.**

Sample	La (mol%)	EDS data			
		O (wt.%)	Ti (wt.%)	La (wt.%)	Total (wt.%)
TL(0)	0	39.46	60.54	0	100
TL(0.65)	0.65	42.91	57.09	0	100
TL(1)	1	49.71	49.44	0.85	100
TL(2)	2	44.59	53.45	1.96	100
TL(6)	6	41.71	52.39	5.91	100

taken from the pure and 6 mol% La doped nanopowders, respectively, pressed into the pellets, whereas the image (b) is recorded on nanopowder TL(1), previously dispersed in ethanol, deposited on freshly cleaved HOPG (highly oriented prolific graphite). From these images we can observe that samples consist of very small nanocrystals (up to 20 nm) and greater

agglomerated particles. However, in the close-up image of the sample with 6 mol% La, as the most interesting, one could observe a granular structure (up to 2 nm) covering the surface of some nanoparticles.

### 3.3. EDS

The chemical composition of pure and some La-doped nanopowders has been estimated by EDS method (Table 2). The micrographs of chosen samples (pure TL(0) and doped TL(0.65), TL(1) and TL(6)) are shown in Fig. 3(a), whereas the EDS spectra of pure and maximally doped sample are presented in Fig. 3(b). The oxygen weight percent in pure TiO<sub>2</sub> nanopowder sample is close to stoichiometric TiO<sub>2</sub> (40 wt.%), whereas the percent of oxygen is higher in the La-doped samples. The final molar La/Ti ratio calculated from EDS data is lower than at the beginning of the synthesis process. It is estimated at around 63% of the starting value, except in the case of the sample doped with

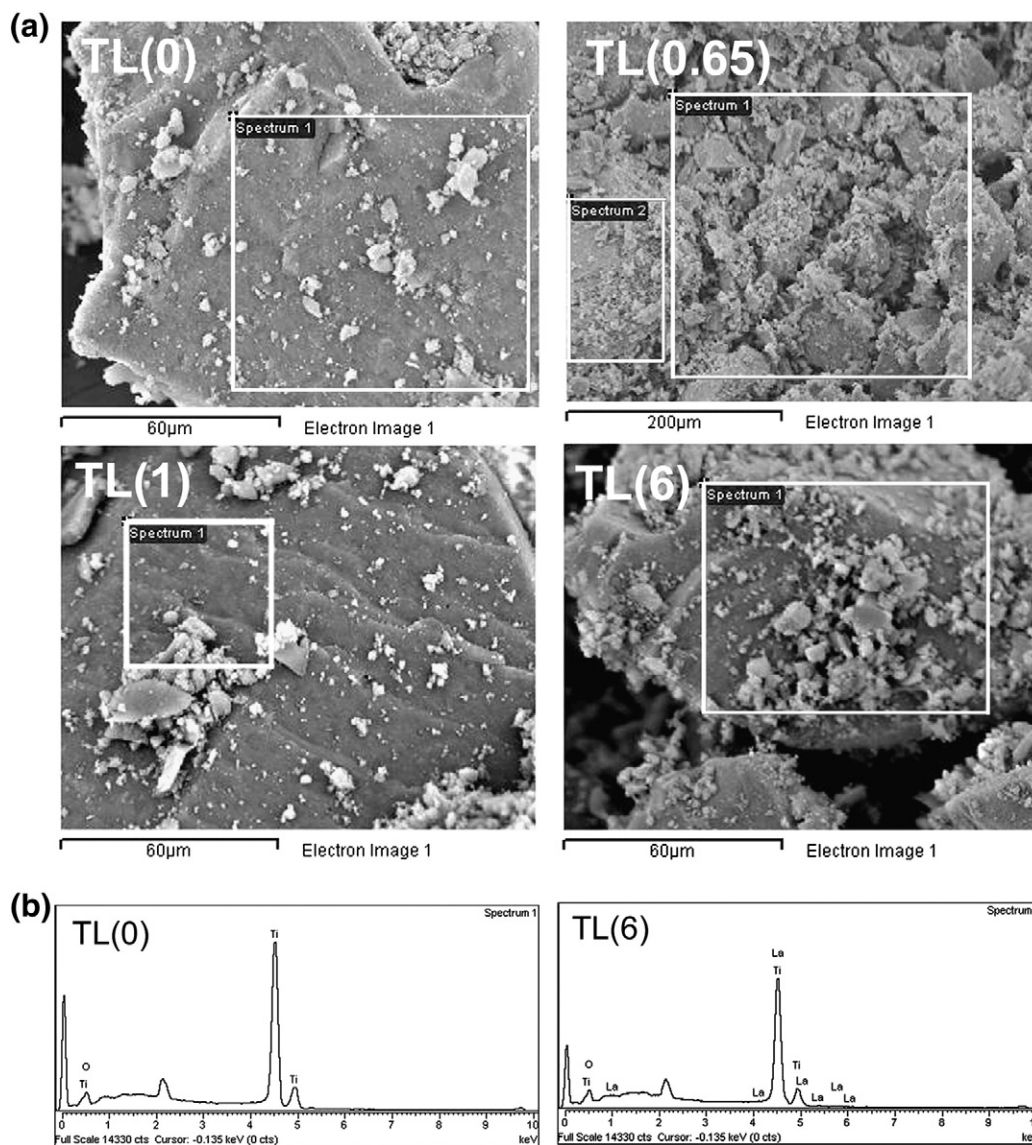


**Fig. 3 – (a) The SEM images of pure TL(0) and some La-doped nanopowders TL(0.65), TL(1) and TL(6); (b) EDS spectra of pure TiO<sub>2</sub>, TL(0), and nanopowder doped with the highest percent of La, TL(6).**

0.65 wt.% of La, where such low content of La could not be detected by EDS method.

### 3.4. BET

To investigate the effects of lanthanum doping on the pore structure and adsorption abilities of TiO<sub>2</sub> nanopowders, the nitrogen sorption isotherm measurements have been carried out. The parameters of porosity, determined from the  $\alpha_s$ -plots [17] obtained from the standard nitrogen adsorption isotherms suggest that the samples are fully mesoporous. The specific surface area ( $S_{BET}$ ) and pore volume ( $V_p$ ) obtained by BET method, and mesopore diameter calculated from both BET and BJH ( $\bar{D}_{BET}$ ,  $\bar{D}_{BJH}$ , respectively) for chosen samples are listed in Table 3. The values of  $S_{BET}$  in La-doped samples ( $\sim 80 \text{ m}^2 \text{ g}^{-1}$ ) are higher than those in pure nanopowder ( $58 \text{ m}^2 \text{ g}^{-1}$ ). Mean pore diameters, obtained from BET results as  $\bar{D}_{BET} = 4V_p/S_{BET}$  are in good agreement with the diameters obtained by BJH method.

The pore size distribution (PSD) is estimated from the desorption branch of the hysteresis isotherm loops by usually used BJH method [18]. The mean pore diameters obtained by BJH method, listed in Table 3, are comparable to the corresponding diameters obtained by BET method. The CPSM method [12,22] for PSD evaluation has been also applied. In this method the pore structure is considered as a statistically large number of independent, nonintersected corrugated pores, made of a series of  $N_s$  cylindrical segments of equal length, with randomly distributed diameters of mesopores [11,12,22]. The pore volume distributions obtained by CPSM are shown in Fig. 4 (thick lines). Note that the distributions calculated by this method are somewhat wider than those obtained by BJH, although corresponding mean pore diameters are in good agreement (Table 3). The CPSM fitting parameter  $N_s$ , mentioned above, is also listed in Table 3: higher values of  $N_s$  have been obtained for doped samples, which can be associated with a more complex pore structure in doped samples [12]. As a result of CPSM, the pore tortuosity factor  $\tau$  is also estimated (Table 3), as a measure of diffusion through porous media based on nitrogen sorption hysteresis data [11,12]. The dependence of tortuosity factor on the La-content in doped samples shows the same tendency as  $N_s$ : higher values of  $\tau$  are obtained for doped samples, with the maximum in the sample TL(0.65) ( $\tau = 5.3$ ), pointing to the most

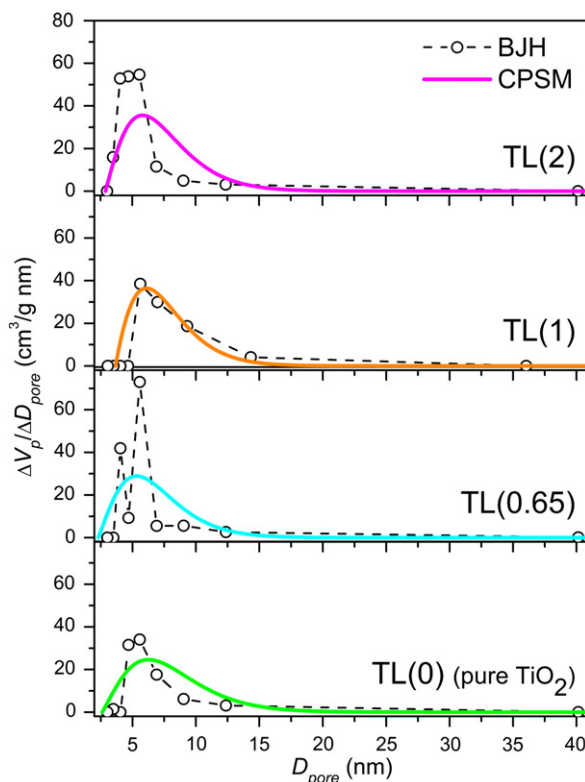


**Fig. 4 – The pore size distribution for pure TiO<sub>2</sub> and some La-doped nanopowders obtained by BJH (symbols with thin dashed lines) and CPSM (thick lines) methods.**

complex pore structure consisting of interconnected pore segments with different diameters in this sample.

### 3.5. Raman Scattering

The Raman spectra of all synthesized nanopowders are dominated by anatase Raman modes [11,23]:  $E_{g(1)}$  ( $\sim 143 \text{ cm}^{-1}$ ),  $E_{g(2)}$  ( $\sim 199 \text{ cm}^{-1}$ ),  $B_{1g}$  ( $\sim 399 \text{ cm}^{-1}$ ),  $A_{1g} + B_{1g}$  ( $\sim 518 \text{ cm}^{-1}$ ), and  $E_{g(3)}$  ( $\sim 639 \text{ cm}^{-1}$ ), as can be seen from the spectrum of TiO<sub>2</sub> nanopowder doped with 0.65 mol% La shown in Fig. 5. The  $E_{g(1)}$  Raman mode is shifted and broadened in all synthesized nanopowders in comparison with corresponding bulk value [10,11]. By applying the phonon confinement model [24] on those experimental results, the anatase crystallite size has been estimated as  $\sim 12 \text{ nm}$  in samples with 1–4 mol% of La, and  $\sim 15 \text{ nm}$  in the other doped samples, as well as pure TiO<sub>2</sub> nanopowder, which is in good accordance with XRPD results. The broadening of the experimental Raman modes, which exceed the values ascribed to the phonon confinement effect only, also suggests the presence of defects and nonstoichiometry [11,24,25].

Additional Raman features, detected in the spectra of all samples, in the range from  $210$  to  $380 \text{ cm}^{-1}$  (shown enlarged in Fig. 7), can be ascribed to the brookite phase:  $A_{1g}$  ( $\sim 247 \text{ cm}^{-1}$ ),  $B_{3g}$  ( $\sim 288 \text{ cm}^{-1}$ ),  $B_{1g}$  ( $\sim 322 \text{ cm}^{-1}$ ), and  $B_{2g}$  ( $\sim 366 \text{ cm}^{-1}$ ) [10,11,25]. Low intensities and large linewidths of these modes indicate great disorder and partial amorphization of brookite in all the samples [10,11,25].

**Table 3 – The porous properties of TiO<sub>2</sub> samples (TL(0), TL(0.65), TL(1), and TL(2)): specific surface area ( $S_{BET}$ ), pore volume ( $V_p$ ), mean pore diameters obtained from different methods ( $\bar{D}_{BET}$ ,  $\bar{D}_{BJH}$ ,  $\bar{D}_{CPSM}$ ), CPSM fitting parameter  $N_s$  and predicted tortuosity factor  $\tau$ .**

	Sample			
	TL(0)	TL(0.65)	TL(1)	TL(2)
$S_{BET}$ ( $\text{m}^2 \text{ g}^{-1}$ )	58	79	84	78
$V_p$ ( $\text{cm}^3 \text{ g}^{-1}$ )	0.160	0.185	0.258	0.215
$S_{BJH}$ ( $\text{m}^2 \text{ g}^{-1}$ )	58.2	79.4	83.8	78.1
$\bar{D}_{BET}$ (nm)	7.1	6.0	7.9	7.1
$\bar{D}_{BJH}$ (nm)	7.1	6.3	7.7	7.5
$\bar{D}_{CPSM}$ (nm)	8.1	6.9	7.7	7.5
$N_s$	8	13	12	11
$\tau$	4.1	5.3	4.4	4.6

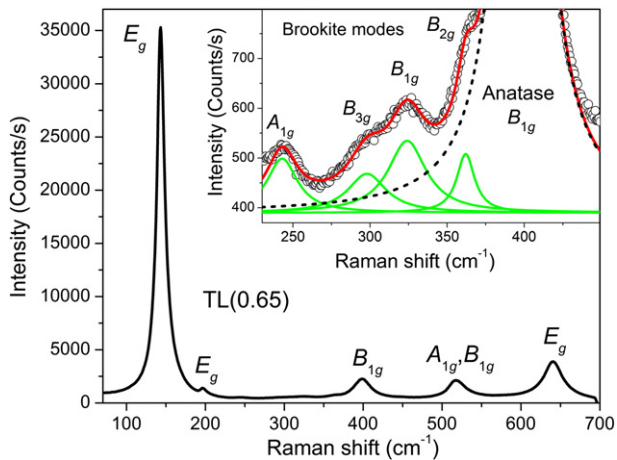


**Fig. 5** – The Raman spectrum of doped TiO<sub>2</sub> nanopowdered sample TL(0.65) with anatase modes denoted. Inset: the region of 230–450 cm<sup>-1</sup> with characteristic brookite modes.

The Raman spectra of pure and representative La-doped TiO<sub>2</sub> nanopowders (TL(0.65), TL(1) and TL(2)) in the C–H and O–H spectral region (2300–4000 cm<sup>-1</sup>) are shown in Fig. 6. Few broad features have been noticed in this region. According to many other vibrational studies, carried out to determine the characteristics of water molecules and hydroxyl groups adsorbed on anatase surfaces ([26] and references therein), broad Raman structure in the frequency range of 2800–3800 cm<sup>-1</sup> can be assigned to O–H stretching vibration of water molecules

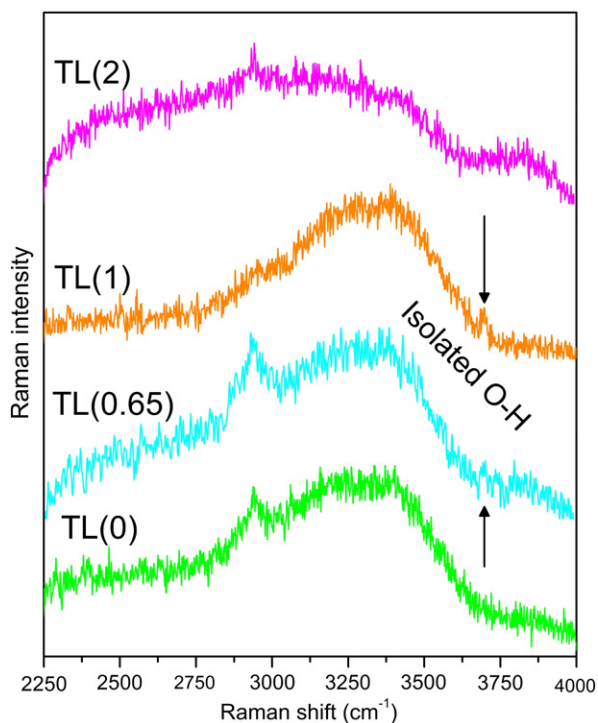


**Fig. 6** – The Raman spectra of pure TiO<sub>2</sub> and selected La-doped TiO<sub>2</sub> nanopowders in the C–H and O–H spectral region (2300–4000 cm<sup>-1</sup>). The mode ascribed to isolated OH groups in samples TL(0.65) and TL(1) is marked by the arrows. The spectra of doped samples are upshifted for clarity.

adsorbed on the surface of the particles and condensed in the pores of TiO<sub>2</sub> nanopowders [10,27], whereas the peak at ~2940 cm<sup>-1</sup> can be assigned to the stretching mode characteristic for CH– species [10,28]. Moreover, a low intensity peak located at ~3700 cm<sup>-1</sup> is noticed in the samples doped with low La content (TL(0.65) and TL(1)). This peak is assigned to the O–H stretching mode of isolated (free) hydroxyls [10,26], and can be related to the ability of the anatase samples to form the surface O–H groups with the important influence on their catalytic activity [10,29].

### 3.6. Spectroscopic Ellipsometry

The optical band gap energy has been estimated by means of the extinction coefficient  $k$ , obtained from SE data of pure and doped TiO<sub>2</sub> nanopowders, by using a so-called two phase model. In a case of large band gap semiconductors, in a small energy range in the vicinity of the optical band gap energy  $E_g$ , the absorption coefficient  $\alpha$  is assumed to follow the well-known dependence  $\alpha h\nu \approx A(h\nu - E_g)^\gamma$ , where  $A$  is a sample-dependent constant parameter,  $\gamma$  is a constant equal to 1/2 and 2 for direct and indirect allowed transitions, respectively, and  $h\nu$  is the photon energy. Then,  $E_g$  can be graphically estimated by a linear fit of the high energy tail of  $(\alpha h\nu)^{1/\gamma}$  [30]. The absorption coefficient has been evaluated from the extinction coefficient  $k$  of pure and doped anatase nanopowders, as  $\alpha = 4\pi k / \lambda$ , where  $\lambda$  is the wavelength of incident light. In the literature, both direct and indirect band to band transitions of nanocrystalline anatase titania are reported ([30] and references therein). To establish the type of electronic transition of the synthesized samples, the absorption coefficient data were fitted to the equation for both indirect and direct band gap transitions. Fig. 7(a) shows the  $(\alpha h\nu)^{1/2}$  plots versus the photon energy  $h\nu$  for an indirect transition, whereas the  $(\alpha h\nu)^2$  plots for a direct transition are given in Fig. 7(b). The dispersions of  $(\alpha h\nu)^{1/2}$  of the samples under examination do not show an asymptotic linear behavior in the near-UV region (Fig. 7(a)). This finding confirms that, contrary to bulk anatase, synthesized TiO<sub>2</sub> nanoparticles do not exhibit an indirect type of band to band transition. In Fig. 7(b) the dispersions of  $(\alpha h\nu)^2$  clearly show an asymptotic linear behavior in the near-UV region, and the intercepts of the linear-fit extrapolations with the horizontal axes led us to estimate the energy of the optical band gap corresponding to the direct electronic transition. The dependence of the optical band gap energy on mol% of La is presented in the inset of Fig. 7(b). The band gap values, found in the range from 3.62 to 3.82 eV, are higher than that of bulk anatase TiO<sub>2</sub> (3.2 eV) [30], and gradually increase with the increase of molar percent of La in titania nanopowders.

Spectroscopic ellipsometry has been also used to determine the room temperature pseudodielectric function spectra of pure and doped anatase nanopowders. The features observed in the range from 2 to 6 eV of the  $\epsilon(\omega)$  spectra are ascribed to interband critical points (CPs) [19,20,31], which are related to regions of the band structure with large or singular point electronic density of states [19]. Those structures are analyzed by standard analytic line shapes [20]:  $\epsilon(\omega) = C - A \exp(i\varphi)(\omega - E + i\gamma)^m$ , where a CP is described by the amplitude  $A$ , threshold energy  $E$ , broadening  $\gamma$  and phase angle  $\varphi$ . The exponent  $m$  takes the values of -1/2 and 1/2 for one- (1D) and three-dimensional (3D) CPs, respectively. Two dimensional (2D) CPs are described with  $m = 0$



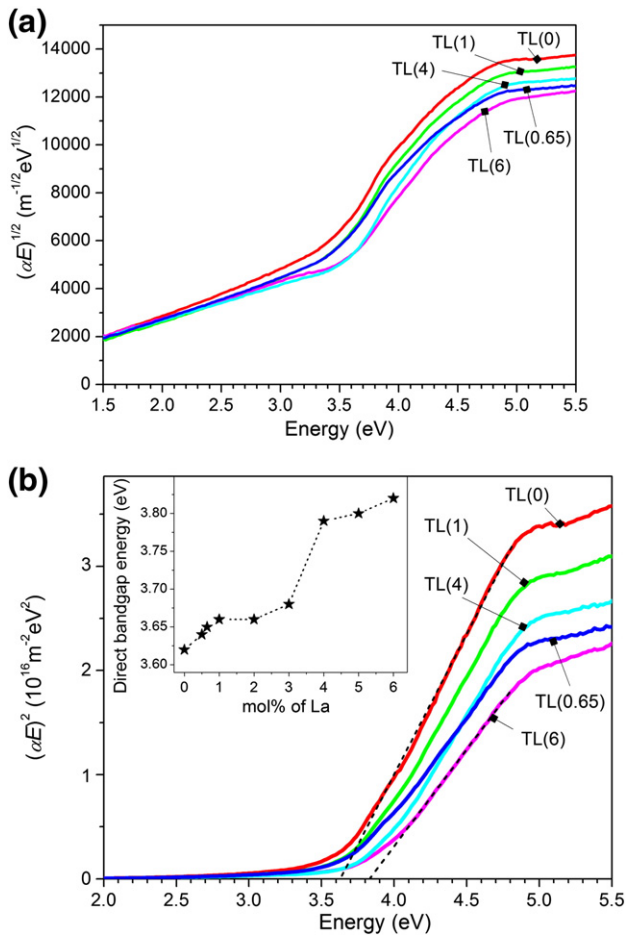


**Fig. 7 – (a) The plot of  $(\alpha E)^{1/2}$  versus  $E$  for indirect band gap transition in pure and selected La-doped  $\text{TiO}_2$  nanopowders; (b) the plot of  $(\alpha E)^2$  versus  $E$  for direct band gap transition in the same samples with characteristic tangent lines. Inset: the dependence of estimated direct band gap energy on mol% of La.**

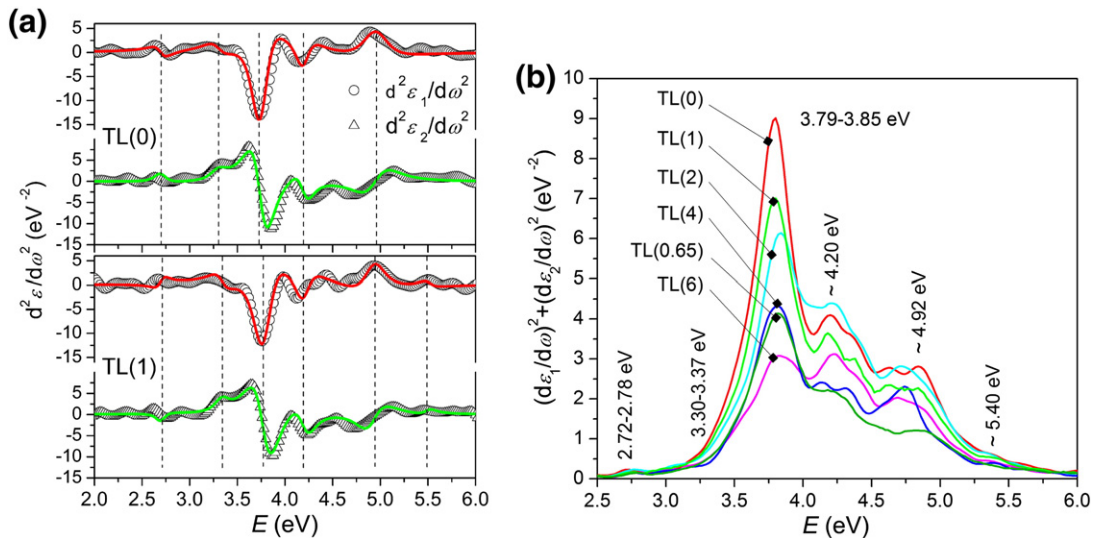


**Fig. 8 – (a) The second derivatives of the real ( $\varepsilon_1(\omega)$ , denoted by circles) and imaginary ( $\varepsilon_2(\omega)$ , triangles) parts of the dielectric functions of  $\text{TiO}_2$  nanopowders TL(0) and TL(1), obtained by SE measurements, together with the fitting curves (lines); (b) the module of the first derivative of dielectric function  $\varepsilon(\omega)$  of pure and several La-doped anatase nanopowders.**

and corresponding analytical line shape is given by  $\varepsilon(\omega) = C - A \exp(i\varphi) \ln(\omega - E + i\gamma)$ . Discrete excitons with a Lorentzian line shape (0D) are represented by  $m = -1$ . The values of the CP energy thresholds have been determined by theoretical fitting of both the second derivative and the module of the first derivative.

The 2nd derivative spectra of the complex dielectric function,  $d^2\varepsilon(\omega) / d\omega^2$ , have been calculated by a standard technique of smoothing polynomials to obtain the CP parameters [19]. It is given in analytic form as follows [21]:

$$\frac{d^2\varepsilon}{d\omega^2} = A' \Omega^{(m-2)/2} \left( \begin{aligned} &\cos\left((m-2) \arccos\left(\frac{\omega-E}{\Omega^{1/2}}\right) + \varphi\right) \\ &+ i \sin\left((m-2) \arccos\left(\frac{\omega-E}{\Omega^{1/2}}\right) + \varphi\right) \end{aligned} \right), \quad (1)$$

with  $\Omega = (\omega - E)^2 + \gamma^2$ . Note that for  $\omega \neq 0$ ,  $A' = -m(m-1)A$ , but for  $m = 0$ ,  $A'$  must be equal to  $A$ . The parameters  $A$ ,  $E$ ,  $\gamma$  and  $\varphi$  have been calculated for all investigated nanopowders by fitting the numerically obtained second derivative spectra of the experimental  $\varepsilon(\omega)$  to Eq. (1), considering the CPs of 2D and 3D types [31]. The 2nd derivatives of the real and imaginary parts ( $\varepsilon_1(\omega)$  and  $\varepsilon_2(\omega)$  respectively) of the complex dielectric function  $\varepsilon(\omega)$  of pure (TL(0)) and one doped  $\text{TiO}_2$  nanopowder (TL(1)), obtained from SE experimental data, are shown in Fig. 8(a). Corresponding fitting curves, taking into account the electronic transitions in the range from 2 to 6 eV, according to Eq. (1) are also shown. According to this procedure, the electronic transitions with energies at about 2.72, 3.35, 3.80, 4.20 and 4.93 eV have been registered in all samples, whereas the transition at about 5.5 eV has been noticed in doped nanopowders only. Thereby, the energies of the first three transitions listed above are gradually increasing with the molar percent of lanthanum.

The module of the first derivative of dielectric function  $\varepsilon(\omega)$  for pure and several La-doped nanopowders, defined as  $|d\varepsilon/d\omega|^2 = (d\varepsilon_1/d\omega)^2 + (d\varepsilon_2/d\omega)^2$ , is shown in Fig. 8(b). Generally, the module of the first derivative of dielectric function shows peaks that correspond to CPs of energy transitions of the

electronic band structure [19]. The shift of the most intensive peak from 3.79 to 3.85 eV with the increase of mol% of La, is obvious from Fig. 8(b). Similar behavior is registered for the peak at 2.72–2.78 eV, whereas the peak at ~5.4 eV has approximately the same position in all doped samples. The position and behavior of other peaks denoted in Fig. 8(b) are hard to correlate with La content systematically, mostly because of the difficulties in precise evaluation of their energies in the spectra.

### 3.7. STM/STS

The AFM results, shown in Fig. 2, point to the existence of a great number of nanoparticles with rough granular surface (Fig. 2(d)) in the sample with 6 mol% of La. Since TiO<sub>2</sub> nanoparticles with both smooth and rough surfaces in that sample have also been distinguished by the STM, STS measurements have been used to obtain information on the surface band gap in the nanoparticles with different surface morphologies.

The tunneling spectroscopy was performed by positioning the tip over different isolated TiO<sub>2</sub> nanoparticles and measuring their *I*-*V* characteristics. The measurements of *I*-*V* characteristics have been always repeated several times and the signal has been finally averaged for 100 runs. The *dI/dV* versus *V* characteristics, corresponding to the characteristic density of states, have been obtained by numerical differentiation of measured *I*-*V* curves. Fig. 9(a) shows a typical *dI/dV* versus *V* characteristic of isolated TiO<sub>2</sub> particles with smooth surface. The STM image of such particle from the sample TL(6) is given in the inset of Fig. 9(a). From the presented STS data, the surface band gap of those particles has been estimated as ~3.2 eV, a value close to the band gap of the anatase phase [30]. However, in the same sample, for isolated TiO<sub>2</sub> particles covered with rough granular structure (Fig. 9(b)), the higher value of surface band gap (~4 eV) has been found.

### 3.8. Photocatalysis

The influence of different amounts of La<sup>3+</sup> in the La-doped TiO<sub>2</sub> nanopowders on photocatalytic activity was studied

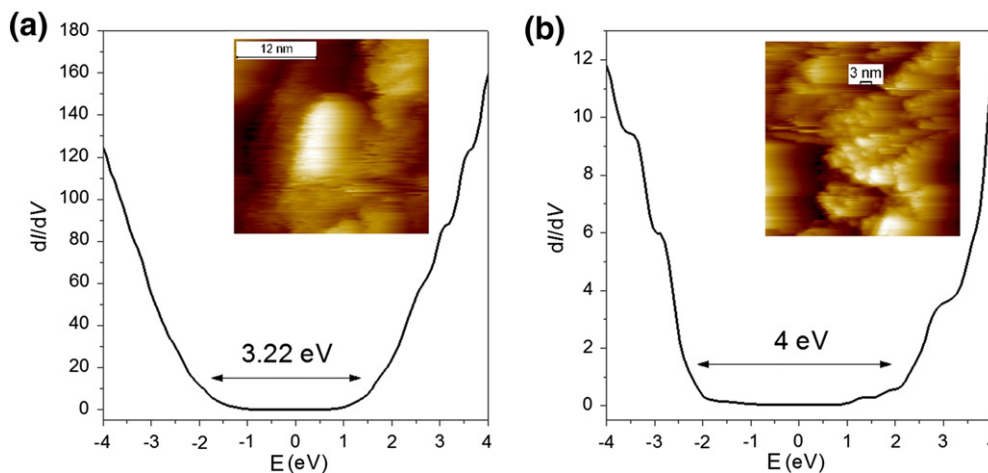


Fig. 9 – The *dI/dV* versus *V* characteristics of isolated TiO<sub>2</sub> nanoparticles of TL(6) sample, with smooth (a) and rough (b) surfaces obtained by STS, followed by corresponding STM images in the insets.

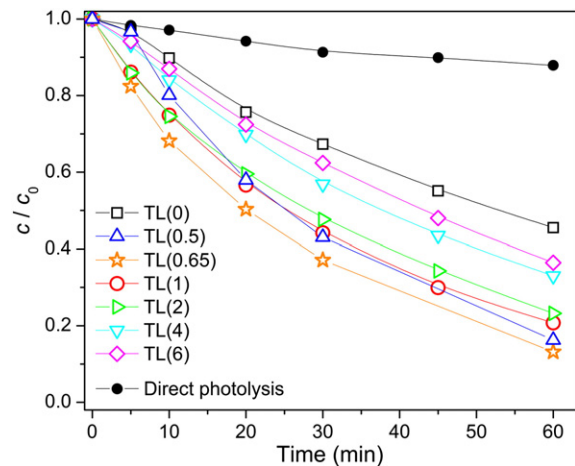
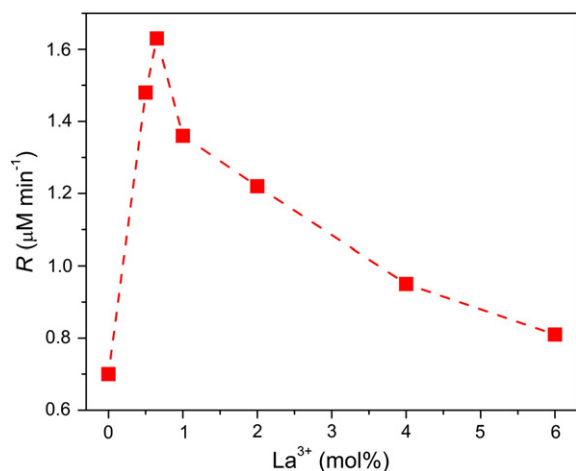


Fig. 10 – Kinetics of MET (0.05 mM) photodegradation under UV irradiation in the presence of La-doped TiO<sub>2</sub> nanopowders with various amounts of La, pure TiO<sub>2</sub>, and direct photolysis. When present, the catalyst loading was 1 mg ml<sup>-3</sup>.

through the photocatalytic degradation of MET under UV light irradiation. Kinetic curves for all investigated samples are presented in Fig. 10, together with the results obtained using pure TiO<sub>2</sub> and direct photolysis. On the basis of these kinetic curves, a linear dependence of  $\ln(c/c_0)$  on illumination time was obtained in the first period (30 min) of heterogeneous photocatalysis for all synthesized samples suggesting that the degradation reaction of the MET is of pseudo-first kinetic order (the linear correlation coefficients varied in the range 0.994–0.999).

As can be seen in Fig. 10, the photocatalytic activity of all doped samples with La<sup>3+</sup> exhibited a significant increase in the MET photodegradation efficiency compared to pure TiO<sub>2</sub>. It can be concluded (Fig. 11) that among all tested La-doped TiO<sub>2</sub> nanopowder samples the highest photocatalytic efficiency was exhibited by the sample TL(0.65), as it led to an 87% elimination of MET within 60 min. However, pure TiO<sub>2</sub> has eliminated only 55% of MET for the same time. These results



**Fig. 11 – The influence of La doping content in TiO<sub>2</sub> nanopowders on MET (0.05 mM) photocatalytic degradation rate determined for the first 30 min of irradiation.**

are in agreement with literature data [32]. Besides, as can be seen in Fig. 10, the addition of the photocatalysts, both undoped and doped with La<sup>3+</sup> has markedly improved the degradation rate of MET in comparison to direct photolysis, i.e., in the absence of TiO<sub>2</sub>.

#### 4. Discussion

The experimental results obtained from XRPD and Raman measurements, presented in previous paragraphs, have shown that synthesized TiO<sub>2</sub> nanopowders retain their anatase structure as the dominant phase, with the brookite content slightly varying with La-doping. Thereby, the anatase crystallites in doped samples are smaller than those in pure sample TL(0), with the strain slightly increasing with doping. The XRPD data confirmed the formation of crystalline La<sub>2</sub>O<sub>3</sub> oxide only in the sample TL(0.65). The absence of the peaks characteristic for lanthanum oxide in XRPD data of other doped samples may indicate that this oxide is highly dispersed and/or mainly amorphized [33]. Also, retaining the position of the main diffraction peak of anatase with La-doping (within experimental error) stands in favor of the assumption that lanthanum has rather formed an oxide, than substituted titanium in the anatase lattice, due to the much greater ionic radius of La<sup>3+</sup> ions (1.22 Å) than that of Ti<sup>4+</sup> (0.69 Å) [3,8].

Although Raman spectroscopy has rarely been applied to study the surface complex formation of anatase nanoparticles [27], because the Raman features are hard to resolve due to intensive sample luminescence in C–H and O–H spectral region, we have demonstrated the applicability of Raman spectroscopy to identify specified surface groups. In addition to broad Raman feature between 2800 and 3800 cm<sup>-1</sup>, assigned to OH stretching vibrations, and the peak at ~2940 cm<sup>-1</sup> assigned to the stretching mode of CH-species, both present in the spectra of all samples, we have found a low intensity peak at ~3700 cm<sup>-1</sup> in the spectra of the samples doped by low La content (TL(0.65) and TL(1)). The peak at ~3700 cm<sup>-1</sup> is assigned to the O–H stretching mode of isolated (free) hydroxyls, which are, according to several

authors, the most photocatalytically active among all hydroxyl groups at the surface of TiO<sub>2</sub> nanoparticles [34].

The analysis of chemical composition by EDS method has shown that the ratio of Ti/O content is higher in doped samples in comparison to pure TiO<sub>2</sub>. However, this method could not distinguish whether the excess oxygen participates in La<sub>2</sub>O<sub>3</sub> or in interstitial oxygen, molecular oxygen at the surface and/or OH groups [10].

The morphological investigation of synthesized nanopowders, performed by nitrogen sorption isotherm measurements, has shown that doped samples are also fully mesoporous, and that La-doping increases the specific surface area to about 30%. Also, the total pore volume and pore structure complexity are increased in doped samples, which could be explained by the presence of La<sub>2</sub>O<sub>3</sub> accumulated on the surface of TiO<sub>2</sub> nanoparticles, which inhibit the agglomeration of TiO<sub>2</sub> particles and produce more complex pores [35].

The analysis of SE data has shown that, contrary to bulk anatase, synthesized TiO<sub>2</sub> nanoparticles do not exhibit an indirect type of band to band transition, which confirms the findings of many authors, that TiO<sub>2</sub> nanoparticles with small crystalline domain exhibit a direct type of band to band transition [30]. These results have also shown that the energy of direct band gap transitions gradually increases with La-doping. The literature data have shown that the optical gap increases significantly with the increasing of La<sub>2</sub>O<sub>3</sub> concentration in TiO<sub>2</sub> [8], whereas incorporation of La<sup>3+</sup> in TiO<sub>2</sub> lattice usually leads to the slight shift of absorption edges of La-doped TiO<sub>2</sub> towards a longer wavelength (red shift) in comparison to pure TiO<sub>2</sub> [36]. So, the gradual increase of band gap registered in our doped samples can be related to increasing concentration of La<sub>2</sub>O<sub>3</sub>. Namely, when anatase TiO<sub>2</sub> is mixed with a larger band gap La<sub>2</sub>O<sub>3</sub> (~5.5 eV [37]), the band gap of the composite semiconductor TiO<sub>2</sub>/La<sub>2</sub>O<sub>3</sub> should be shifted to a higher energy in comparison with pure TiO<sub>2</sub>. Such conclusion is also supported by the results of the CP method. Namely, the electronic transition registered at ~5.4 eV has approximately the same energy for all doped samples, which implies that this transition may be related to the band gap of La<sub>2</sub>O<sub>3</sub>.

The STS data, recorded simultaneously with the STM topography, have provided direct experimental evidence for the modification of surface electronic properties by La-doping. The more prominent presence of granular structure at the surface of TiO<sub>2</sub> nanoparticles in the samples doped with a higher amount of La (6 mol%), as well as a higher value of surface band gap (~4 eV) in those particles, than in particles with smooth surface (~3.2 eV), most probably implies that the granular structure consisted of La<sub>2</sub>O<sub>3</sub>.

All these findings point out that, under specified sol-gel synthesis conditions, the La<sup>3+</sup> ions rather form La<sub>2</sub>O<sub>3</sub> oxide, mainly present in the surface layer of the doped TiO<sub>2</sub> nanopowders, than incorporate in the anatase lattice.

The investigations presented in this work have shown that La-doping does improve the photocatalytic activity of TiO<sub>2</sub> nanopowders, with higher efficiency obtained for lower La content. The kinetic analysis discussed here showed that an optimal La amount, with respect to the efficiency in photocatalytic degradation of MET, is 0.65 mol%, which is similar to the literature data obtained for the degradation of some other organic compounds ([38] and references therein). The improvement in

photocatalytic properties of La-doped samples can be ascribed to the formation of  $\text{La}_2\text{O}_3$  at the grain boundaries of anatase nanoparticles. This effect inhibits the growth of crystal grains, decreases anatase crystallite size and produces a more complex pore structure [35], which is confirmed by the results of XRPD, Raman and BET measurements presented in this work. However, the presence of isolated hydroxyl groups on the surface of  $\text{TiO}_2$  nanoparticles, which can represent a decisive factor in high photocatalytic activity of  $\text{TiO}_2$  [39], has been registered only in the nanopowders with a low level of La-doping—0.65 and 1 mol%. This implies that reduction of photocatalytic activity of  $\text{TiO}_2$  nanopowders with further increase of La-doping amount may be related to the blocking of the active centers due to the accumulation of excess  $\text{La}_2\text{O}_3$  on the surface of anatase grains, registered by both AFM and STM measurements.

## 5. Conclusion

Mesoporous La-doped  $\text{TiO}_2$  photocatalysts, prepared by sol–gel method, have been extensively characterized by various sophisticated techniques. The photocatalytic activity of La-doped  $\text{TiO}_2$  nanopowders has been evaluated for the degradation of MET in an aqueous solution under UV light irradiation. Doped samples have shown a higher rate of degradation than pure  $\text{TiO}_2$ , synthesized under the same condition, with a maximum rate for 0.65 mol% La loading. The enhanced photocatalytic activity of La-doped  $\text{TiO}_2$  is mainly due to the smaller particle size, larger specific surface area and total pore volume, as well as higher pore structure complexity. Moreover, the presence of isolated (free) hydroxyls, as the most photocatalytically active hydroxyl groups, has been registered in the  $\text{TiO}_2$  photocatalysts with low La content, which exhibit the highest photocatalytic efficiency.

This study has also shown that the spectroscopic ellipsometry is able to determine the type of electronic transition in  $\text{TiO}_2$  materials, as well as to resolve the dilemma of whether or not large  $\text{La}^{3+}$  ions replace smaller  $\text{Ti}^{4+}$  ions in the  $\text{TiO}_2$  lattice. Presented analysis of SE results has shown gradual increase of direct band gap energy with La-doping, which can be attributed to the surface modification of  $\text{TiO}_2$  nanoparticles, confirmed by the STM/STS measurements.

## Acknowledgments

This work was financially supported by the Serbian Ministry of Education and Science under the Project Nos. III45018, ON171032, and ON172042, as well as the SASA Project F-134. The authors also express their gratitude to MSc. Marko Radović for his help in AFM and ellipsometric measurements.

## REFERENCES

- [1] Chen W, Hua D, Jun-Ying T, Ji-Mei A. Photocatalytic activity enhancing for  $\text{TiO}_2$  photocatalyst by doping with La. *Trans Nonferrous Met Soc China* 2006;16:s728–31.
- [2] Kim HR, Lee TG, Shul YG. Photoluminescence of La/Ti mixed oxide prepared using sol–gel process and their pCBA photodecomposition. *J Photochem Photobiol A* 2007;185:156–60.
- [3] Liqiang J, Xiaojun S, Baifu X, Baiqi W, Weimin C, Honggang F. The preparation and characterization of La doped  $\text{TiO}_2$  nanoparticles and their photocatalytic activity. *J Solid State Chem* 2004;177:3375–82.
- [4] Jin M, Nagaoka Y, Nishi K, Ogawa K, Nagahata S, Horikawa T, et al. Adsorption properties and photocatalytic activity of  $\text{TiO}_2$  and La-doped  $\text{TiO}_2$ . *Adsorption* 2008;14:257–63.
- [5] Zhao Z, Liu Q. Effects of lanthanide doping on electronic structures and optical properties of anatase  $\text{TiO}_2$  from density functional theory calculations. *J Phys D Appl Phys* 2008;41:085417 [1–9].
- [6] Sun L, Zhao X, Cheng X, Sun H, Li Y, Li P, et al. Synergistic effects in La/N codoped  $\text{TiO}_2$  anatase (101) surface correlated with enhanced visible-light photocatalytic activity. *Langmuir* 2012;28:5882–91.
- [7] Bingham S, Daoud WA. Recent advances in making nano-sized  $\text{TiO}_2$  visible-light active through rare-earth metal doping. *J Mater Chem* 2011;21:2041–50.
- [8] Zhang L, Sun Z-H, Yu F-M, Chen H-B. *Bioinorganic chemistry and applications*. Hindawi Publishing Corporation; 2001. <http://dx.doi.org/10.1155/2011/853048>.
- [9] Golubović A, Šćepanović M, Kremenović A, Askrabić S, Berec V, Dohčević-Mitrović Z, et al. Raman study of the variation in anatase structure of  $\text{TiO}_2$  nanopowders due to the changes of sol–gel synthesis conditions. *J Sol Gel Sci Technol* 2009;49:311–9.
- [10] Šćepanović M, Abramović B, Golubović A, Kler S, Grujić-Brojčič M, Dohčević-Mitrović ZD, et al. Photocatalytic degradation of metoprolol in water suspension of  $\text{TiO}_2$  nanopowders prepared using sol–gel route. *J Sol–Gel Sci Technol* 2012;61:390–402.
- [11] Golubović A, Abramović B, Šćepanović M, Grujić-Brojčič M, Armaković S, Veljković I, et al. Improved efficiency of sol–gel synthesized mesoporous anatase nanopowders in photocatalytic degradation of metoprolol. *Mater Res Bull* 2012;48:1363–71.
- [12] Salmas CE, Androutsopoulos GP. A novel pore structure tortuosity concept based on nitrogen sorption hysteresis data. *Ind Eng Chem Res* 2001;40:721–30.
- [13] Zalc JM, Reyes SC, Iglesia E. The effects of diffusion mechanism and void structure on transport rates and tortuosity factors in complex porous structures. *Chem Eng Sci* 2004;59:2947–60.
- [14] Šojić D, Despotović V, Orčić D, Szabó E, Arany E, Armaković S, et al. Degradation of thiamethoxam and metoprolol by UV,  $\text{O}_3$  and UV/ $\text{O}_3$  hybrid processes: kinetics, degradation intermediates and toxicity. *J Hydrol* 2012;472–473:314–27.
- [15] Ikehata K, Naghashkar NJ, El-Din MG. Degradation of aqueous pharmaceuticals by ozonation and advanced oxidation processes: a review. *Ozone Sci Eng* 2006;28:353–414.
- [16] Rodríguez-Carvajal J. FullProf computer program. <http://www.ill.eu/sites/fullprof/index.html>; 2008.
- [17] Kaneko K, Ishii C, Kanoh H, Hanzawa Y, Setoyama N, Suzuki T. Characterization of porous carbons with high resolution  $\alpha_s$ -analysis and low temperature magnetic susceptibility. *Adv Colloid Interface Sci* 1998;76–77:295–320.
- [18] Barrett EP, Joyner LG, Halenda PP. The determination of pore volume and area distributions in porous substances. I. Computations from nitrogen isotherms. *J Am Chem Soc* 1951;73:373–80.
- [19] Leòn M, Levchenko S, Nateprov A, Nicorici A, Merino JM, Serna R, et al. Dielectric functions and fundamental band gaps of  $\text{Cu}_2\text{In}_4\text{Se}_7$ ,  $\text{CuGa}_3\text{Se}_5$  and  $\text{CuGa}_5\text{Se}_8$  crystals. *J Phys D Appl Phys* 2007;40:740–8.
- [20] Lautenschlager P, Garriga M, Logothetidis S, Cardona M. Interband critical points of GaAs and their temperature dependence. *Phys Rev B* 1987;35:9174–89.
- [21] Alborno JG, Serna R, Leon M. Optical properties and electronic structure of polycrystalline  $\text{Ag}_{1-x}\text{Cu}_x\text{InSe}_2$  alloys. *J Appl Phys* 2005;97:103515 [1–7].

- [22] Androustopoulos GP, Salmas CE. A new model for capillary condensation–evaporation hysteresis based on a random corrugated pore structure concept: prediction of intrinsic pore size distributions: part 1: model development. *Ind Eng Chem Res* 2000;39:3747–63.
- [23] Ohsaka T, Izumi F, Fujiki Y. Raman spectrum of anatase, TiO<sub>2</sub>. *J Raman Spectrosc* 1978;7:321–4.
- [24] Šćepanović MJ, Grujić-Brojčin MU, Dohčević-Mitrović ZD, Popović ZV. Effects of confinement, strain and nonstoichiometry on Raman spectra of anatase TiO<sub>2</sub> nanopowders. *Mater Sci Forum* 2006;518:101–6.
- [25] Šćepanović M, Aškračić S, Berec V, Golubović A, Dohčević-Mitrović Z, Kremenović A, et al. Characterization of La-doped TiO<sub>2</sub> nanopowders by Raman spectroscopy. *Acta Phys Pol A* 2009;115:771–4.
- [26] Soria J, Sanz J, Sobrados I, Coronado JM, Maira AJ, Hernandez-Alonso MD, et al. FTIR and NMR study of the adsorbed water on nanocrystalline anatase. *J Phys Chem C* 2007;111:10590–6.
- [27] Watson S, Beydoun D, Scott J, Amal R. Preparation of nanosized crystalline TiO<sub>2</sub> particles at low temperature for photocatalysis. *J Nanopart Res* 2004;6:193–207.
- [28] Brownson JRS, Tejedor-Tejedor MI, Anderson MA. Photoreactive anatase consolidation characterized by FTIR spectroscopy. *Chem Mater* 2005;17:6304–10.
- [29] Yang D, Liu H, Zheng Z, Yuan Y, Zhao J, Waclawik ER, et al. An efficient photocatalyst structure: TiO<sub>2</sub>(B) nanofibers with a shell of anatase nanocrystals. *J Am Chem Soc* 2009;131:17885–93.
- [30] Ferrara MC, Pilloni L, Mazzarelli S, Tapfer L. Hydrophilic and optical properties of nanostructured titania prepared by sol–gel dip coating. *J Phys D Appl Phys* 2010;43:095301.
- [31] Šćepanović M, Grujić-Brojčin M, Mirić M, Dohčević-Mitrović Z, Popović ZV. Optical characterization of laser-synthesized anatase TiO<sub>2</sub> nanopowders by spectroscopic ellipsometry and photoluminescence measurements. *Acta Phys Pol A* 2009;116:603–6.
- [32] Wu H-H, Deng L-X, Wang S-R, Zhu B-L, Huang W-P, Wu S-H, et al. The preparation and characterization of La doped TiO<sub>2</sub> nanotubes and their photocatalytic activity. *J Dispersion Sci Technol* 2010;31:1311–6.
- [33] Shi Z-L, Lai H, Yao S-H, Wang S-F. Preparation, characterization and photocatalytic activity of lanthanum doped mesoporous titanium dioxide. *Chin J Chem Phys* 2012;25:96–102.
- [34] Bégin-Colin S, Gadalla A, Le Caer G, Humbert O, Thomas F, Barres O, et al. On the origin of the decay of the photocatalytic activity of TiO<sub>2</sub> powders ground at high energy. *J Phys Chem C* 2009;113:16589–602.
- [35] Cao G, Li Y, Zhang Q, Wang H. Synthesis and characterization of La<sub>2</sub>O<sub>3</sub>/TiO<sub>2-x</sub>F<sub>x</sub> and the visible light photocatalytic oxidation of 4-chlorophenol. *J Hazard Mater* 2010;178:440–9.
- [36] Parida KM, Sahu N. Visible light induced photocatalytic activity of rare earth titania nanocomposites. *J Mol Catal A Chem* 2008;287:151–8.
- [37] Yang C, Fan H, Qiu S, Xi Y, Fu Y. Microstructure and dielectric properties of La<sub>2</sub>O<sub>3</sub> films prepared by ion beam assistant electron-beam evaporation. *J Non-Cryst Solids* 2009;355:33–7.
- [38] Zhang S, Zheng Z, Wang J, Chen J. Heterogeneous photocatalytic decomposition of benzene on lanthanum-doped TiO<sub>2</sub> film at ambient temperature. *Chemosphere* 2006;65:2282–8.
- [39] Liu G, Sun C, Cheng L, Jin Y, Lu H, Wang L, et al. Efficient promotion of anatase TiO<sub>2</sub> photocatalysis via bifunctional surface-terminating Ti–O–B–N structures. *J Phys Chem C* 2009;113:12317–24.



# Synthesis of pure and La-doped anatase nanopowders by sol–gel and hydrothermal methods and their efficiency in photocatalytic degradation of alprazolam

A. Golubović<sup>a</sup>, N. Tomić<sup>a</sup>, N. Finčur<sup>b</sup>, B. Abramović<sup>b</sup>, I. Veljković<sup>c</sup>, J. Zdravković<sup>d</sup>,  
M. Grujić-Brojčin<sup>a,\*</sup>, B. Babić<sup>e</sup>, B. Stojadinović<sup>a</sup>, M. Šćepanović<sup>a</sup>

<sup>a</sup>Center for Solid State Physics and New Materials, Institute of Physics, University of Belgrade, Pregrevica 118, 11080 Belgrade-Zemun, Serbia

<sup>b</sup>Department of Chemistry, Biochemistry and Environmental Protection, Faculty of Sciences, University of Novi Sad, Trg D. Obradovića 3, 21000 Novi Sad, Serbia

<sup>c</sup>Institute for Multidisciplinary Research, University of Belgrade, Kneza Višeslava 1, 11000 Belgrade, Serbia

<sup>d</sup>Innovation Center, Faculty of Technology and Metallurgy, University of Belgrade, Karnegijeva 4, 11000 Belgrade, Serbia

<sup>e</sup>Institute of Nuclear Sciences “Vinča”, University of Belgrade, 11001 Belgrade, Serbia

Received 31 January 2014; received in revised form 17 April 2014; accepted 12 May 2014

Available online 20 May 2014

## Abstract

Pure and La<sup>3+</sup> doped titanium dioxide (TiO<sub>2</sub>) nanopowders were obtained by sol–gel and hydrothermal methods. A precursor was titanium tetrachloride and concentrations of dopants were 0.5 and 1.0 mol%. Procedures of both methods were the same, up to the last part of synthesis (the transformation from the mother liquor to oxide nanopowders), in order to find the influence of applied methods on the properties of nanopowders. XRD results have shown that all synthesized nanopowders were in the anatase phase. It was seen from DSC measurements that anatase to rutile phase transition took place at a higher temperature with a higher concentration of dopant (La<sup>3+</sup>). The samples obtained by the sol–gel method had a higher temperature of phase transition than related samples obtained by the hydrothermal method. Nanopowder properties have been related to the photocatalytic activity, tested in degradation of the pharmaceutical alprazolam.

© 2014 Elsevier Ltd and Techna Group S.r.l. All rights reserved.

**Keywords:** A. Powders: chemical preparation; B. Porosity; C. Optical properties; D. TiO<sub>2</sub>

## 1. Introduction

Advanced Oxidation Processes (AOPs) have been developed to remove the contaminants of drinking water and industrial effluents [1,2]. Among them, heterogeneous photocatalysis using TiO<sub>2</sub> is regarded as a promising method for the purification and treatment of both contaminated air and water [3,4] due to its performance such as low cost, non-toxicity, chemical stability, availability and the strong oxidizing power of its photogenerated holes. The size of the titanium dioxide particles is an important factor affecting the photocatalytic

activity of this catalyst [5,6]. Therefore, it is not surprising that much research has been focused upon the reduction of the particle size. Nano-semiconductor materials doped with rare-earth elements have the ability of strong adsorption, good thermal stabilization, electron-type conductivity and high photocatalytic activity [7–9].

TiO<sub>2</sub> can be produced by many different methods and among them we are particularly interested for “wet” methods where the most representative are sol–gel and hydrothermal methods. Because of that, in this work pure and La-doped TiO<sub>2</sub> nanoparticles were prepared by sol–gel and hydrothermal methods. The content of La<sup>3+</sup> in our investigation was 0.5 and 1 mol%, as these concentrations have been established as the most appropriate in photocatalytic applications [9,10].

\*Corresponding author. Tel.: +38 1113713023; fax: +38 1113160531.

E-mail address: [myramyra@ipb.ac.rs](mailto:myramyra@ipb.ac.rs) (M. Grujić-Brojčin).

In recent years, pharmaceuticals have been present in the aquatic environment as a consequence of their use in very high quantities throughout the world. Pharmaceuticals are large group of organic compounds which can enter the water system by means of direct disposal and excretion. They may be present in surface water at low concentration levels, depending on the efficiency of wastewater treatments. Despite these low concentrations, the ubiquity of pharmaceuticals in the aquatic environment together, with their persistent biological activities explains the concern over this specific group of water contaminants [11–13]. Until now, a large diversity of pharmaceuticals has been found in the environment: analgesics, antibiotics, antiepileptics,  $\beta$ -blockers, blood–lipid regulators, antidepressants, anxiolytics, sedatives, contraceptives, etc. [14].

Alprazolam (8-chloro-1-methyl-6-phenyl-4H-[1,2,4]triazole[4,3- $\alpha$ ]-[1,4]-benzodiazepine, CAS no. 28981-97-7,  $C_{17}H_{13}ClN_4$ ,  $M_r=308.765$ ) is a short-acting anxiolytic, which belongs to the benzodiazepine class of psychoactive drugs. It has unique clinical and neurochemical spectrum of action among benzodiazepine full agonists [15,16]. Alprazolam acts on the brain and central nervous system to produce a calming effect [17] and it is mainly used to treat anxiety disorders or anxiety associated to symptoms of depression [18]. The extensive use of alprazolam is a consequence of its antidepressant effect, its synergic action as an anxiolytic in combination with antidepressants in patients with advanced cancer, in the treatment of pathologies that imply anxiety disorders of chronic intensity as the social phobia and other psychosocial pathologies [16].

Since pharmaceuticals are being introduced into the environment on a continuous basis and its continuous input and persistence to the water system may result in a potential risk for aquatic and terrestrial organisms, special attention has recently been paid to the degradation of pharmaceuticals as a means of water decontamination. The aim of this work is to estimate the efficiency of pure and  $La^{3+}$  doped anatase nanopowders, synthesized by two different routes, in photocatalytic degradation of alprazolam, as well as to investigate the variations in anatase structure with  $La^{3+}$  doping.

## 2. Experimental details

### 2.1. Synthesis

All chemicals are used without further purifications.

### 2.2. Sol–gel method (SG)

$TiCl_4$  (99.0%, pure, Merck) was used as a precursor. An appropriate amount of  $TiCl_4$  was dissolved in distilled water under vigorous stirring on an ice-bath. To obtain the hydrogel the aqueous solution of  $NH_4OH$  (29% Carlo Erba), was added under careful control of the pH value of the solution to achieve the alkaline conditions (pH $\sim$ 9). After aging in mother liquor for 5 h the hydrogel was filtered and washed out with distilled water until the complete removal of chloride ions (the common analytical procedure with  $AgNO_3$ ). Afterwards the obtained hydrogel was converted to its ethanol–gel by anhydrous

ethanol. Alcolgel was placed in a vessel, dried at 280 °C and calcined at a temperature of 550 °C for 4 h.

### 2.3. Hydrothermal method (HT)

The whole procedure was the same as the sol–gel process until the hydrogel was obtained (including the aging in mother liquor for 5 h). Then hydrogel was placed in a steel pressure vessel (autoclave) under a controlled temperature. The reaction of hydrothermal synthesis was carried out at 200 °C for 24 h. After that, the vessel contents were filtered and washed with distilled water until complete removal of chloride ions. The last step to obtain  $TiO_2$  nanoparticles was drying at 105.5 °C for 72 h.

### 2.4. Characterization methods

Samples of pure and  $La^{3+}$ -doped  $TiO_2$  obtained by both methods were analyzed by XRD using a Stoe Stadi MP diffractometer ( $CuK\alpha_1$  radiation, primary beam Ge monochromator, linear PSD detector, Bragg–Brentano geometry). Data were collected at every 0.01° in the 10–90°  $2\theta$  angular range, using a counting time of 80 s/step. The Fullprof computer program was used. The Williamson–Hall Method [19] was applied for determination of the average microstrain and the mean crystallite sizes.

Composition/quality of  $TiO_2$  has been analyzed on SEM (JEOL JSM-6460LV, with the operating voltage of 20 keV) equipped with an EDS (INCAx-sight) detector and “INAX-stream” pulse processor (Oxford Instruments).

Non-contact atomic force microscopy (NC-AFM) measurements were carried out using Omicron B002645 SPM probe VT AFM 25.

The TG/DSC analysis of samples consisted in pure and  $La$ -doped  $TiO_2$  (anatase) synthesized by sol–gel method and hydrothermal method was carried out on an SDT Q600 instrument (TA Instruments) up to 1100 °C in  $N_2$  atmosphere (flow rate: 100  $cm^3\ min^{-1}$ ; heating rate: 10 °C  $min^{-1}$ ). The pure indium and sapphire were used for the calibration of temperature and DSC signal, respectively.

The porous structure of anatase samples has been evaluated from adsorption/desorption isotherms of  $N_2$  measured on  $TiO_2$  samples, at  $-196$  °C, using the gravimetric McBain method. The main parameters of the porosity such as specific surface area and pore volume have been estimated by the Brunauer–Emmett–Teller (BET) method and  $\alpha_s$ -plot [20]. The pore size distribution has been estimated from hysteresis sorption data by the Barret–Joyner–Halenda (BJH) method [21].

Raman scattering measurements of  $TiO_2$  samples was performed in the backscattering geometry at room temperature in the air using a Jobin-Yvon T64000 triple spectrometer, equipped with a confocal microscope and a nitrogen-cooled charge coupled device detector. The spectra were excited by 514.5 nm line of  $Ar^+/Kr^+$  ion laser with output power less than 5 mW to avoid local heating due to laser irradiation.

## 2.5. Measurements of photocatalytic activity

The photocatalytic activity of the nanopowders was evaluated in the process of the degradation of the solution of alprazolam (Sigma-Aldrich). The photocatalytic degradation was carried out in a cell described previously [22]. A 125 W high-pressure mercury lamp (Philips, HPL-N, emission bands in the UV region at 304, 314, 335 and 366 nm, with maximum emission at 366 nm), together with an appropriate concave mirror, was used as the radiation source. Experiments were carried out using 20 cm<sup>3</sup> of 0.03 mmol dm<sup>-3</sup> of alprazolam solution and the photocatalyst loading was 1.0 mg cm<sup>-3</sup>. The aqueous suspension was sonicated (50 Hz) in the dark for 15 min before illumination, to uniformly disperse the photocatalyst particles and attain adsorption equilibrium. The suspension thus obtained was thermostated at 25 ± 0.5 °C in a stream of O<sub>2</sub> (3.0 cm<sup>3</sup> min<sup>-1</sup>), and then irradiated. During irradiation, the mixture was stirred at a constant rate under continuous O<sub>2</sub> flow. In order to determine the reproducibility of the results, at least duplicated runs were carried out for each condition for averaging the results, and the reproducibility of kinetic measurements was 3–10%.

For the UFLC–DAD kinetic studies of alprazolam photodegradation, aliquots of 0.50 cm<sup>3</sup> were taken from the reaction mixture at the beginning of the experiment and at regular time intervals. Aliquot sampling caused a maximum volume variation of ca. 10% in the reaction mixture. The suspensions containing photocatalyst were filtered through a Millipore (Millex-GV, 0.22 μm) membrane filter. After that, a 10-μl sample was injected and analyzed on UFLC–Shimadzu equipped with an Eclipse XDB-C18 column (150 mm × 4.6 mm i.d., particle size 5 μm, 25 °C). The UV/vis DAD

detector was set at 222 nm (wavelength of alprazolam maximum absorption). The mobile phase (flow rate 1 cm<sup>3</sup> min<sup>-1</sup>) was a mixture of acetonitrile (99.8%, J. T. Baker) and water (40:60, v/v), the water being acidified with 0.1% H<sub>3</sub>PO<sub>4</sub> (85%, Sigma-Aldrich).

## 3. Results and discussion

### 3.1. Synthesis

In the sol–gel synthesis experimental parameters were the same as in our previous experiments [23] except the duration of calcination of 4 h. It was found that using the duration of 4 h to synthesize TiO<sub>2</sub> nanoparticles (anatase phase) have the best photocatalytic properties in photodegradation of metoprolol [22] within samples with various durations of calcination (from 1 to 7 h) and our samples have mentioned set-up of experimental parameters.

In the hydrothermal synthesis experimental parameters were temperature of 200 °C (as in [24,25], although Ti-butoxide was the precursor, and the duration was 24 h (as in [26]). The charge from the vessel in autoclave was the same as in the case of sol–gel synthesis before the processes of drying and calcination due to reveal a influence of type of synthesis on a properties of obtained TiO<sub>2</sub> nanoparticles.

### 3.2. X-ray diffraction

The XRD patterns of pure TiO<sub>2</sub> and doped with La<sup>3+</sup> doped nanopowders, synthesized by sol–gel and hydrothermal

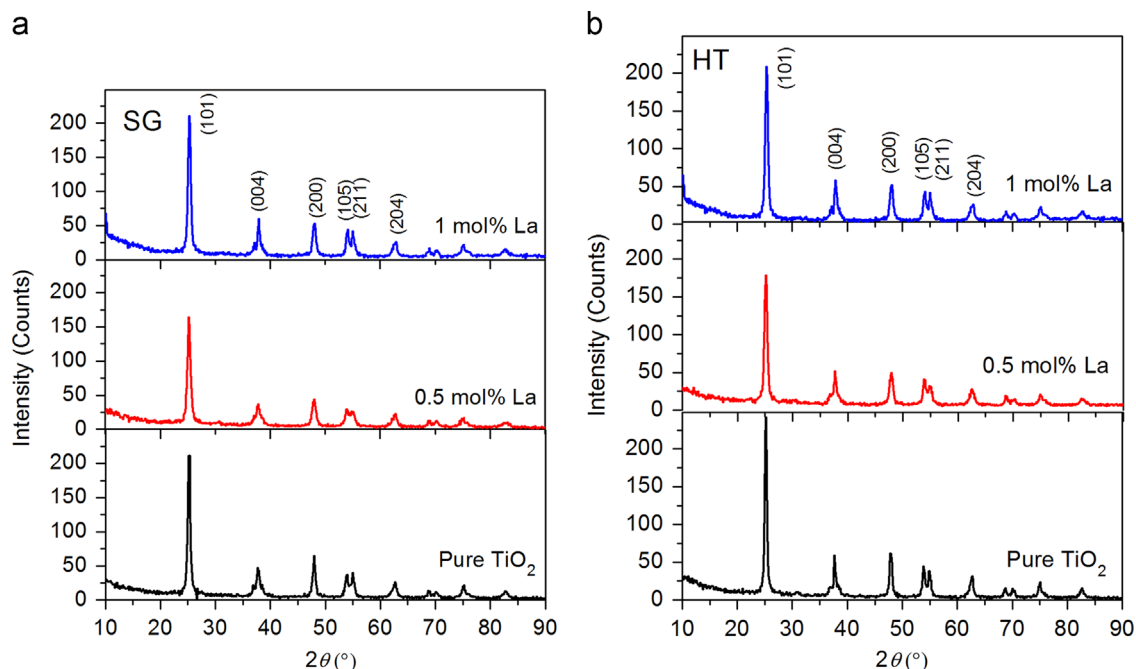


Fig. 1. XRD patterns of pure TiO<sub>2</sub> and La-doped TiO<sub>2</sub> nanopowders synthesized by sol–gel (a) and hydrothermal (b) methods. Characteristic diffractions of anatase phase given in parentheses.



Table 1  
Crystallite size, lattice parameters, and average strain of pure and La<sup>3+</sup> doped TiO<sub>2</sub> (anatase) obtained by sol–gel and hydrothermal methods.

	Crystallite size (nm)	Lattice parameters (nm)		Strain (%)
		a (=b)	c	
SG				
Pure TiO <sub>2</sub>	16	0.3788 (6)	0.9526 (4)	0.12
0.5 mol% La	15	0.3795 (7)	0.9518 (9)	0.29
1 mol% La	15	0.3786 (5)	0.9462 (1)	0.86
HT				
Pure TiO <sub>2</sub>	19	0.3796 (8)	0.9530 (0)	0.13
0.5 mol% La	17	0.3794 (4)	0.9536 (2)	0.24
1 mol% La	18	0.3791 (6)	0.9501 (6)	0.08

method are presented in Fig. 1. The diffraction peaks present in all samples coincide to the anatase TiO<sub>2</sub> structure (JCPDS card 21-1272, space group I41/amd), which is clearly indicated by the main anatase reflection at  $2\theta \sim 25^\circ$ . Their positions are slightly shifted, indicating a change in lattice parameters in comparison to the bulk values for anatase ( $a_0 = 0.37852$  nm,  $c_0 = 0.95139$  nm), as shown in Table 1.

The average crystallite size of anatase nanoparticles, estimated by the Williamson–Hall method, is slightly greater in samples obtained by the hydrothermal method than those obtained by the sol–gel method, as listed in Table 1. The crystallite size in the range from 15 to 19 nm has been estimated from all diffraction patterns. Significant difference in microstrain has not been found in pure TiO<sub>2</sub> samples synthesized by both methods. Similarly, for both samples doped with 0.5% La<sup>3+</sup>, corresponding values of microstrain were close, whereas much smaller microstrain (0.08%) has been detected in the sample doped with 1% La<sup>3+</sup> obtained by the hydrothermal method in comparison to the sample synthesized by the sol–gel method (0.86%).

### 3.3. TG/DSC analysis

The TG analysis of pure, 0.5 mol% La<sup>3+</sup> doped TiO<sub>2</sub> and 1 mol% La<sup>3+</sup> doped TiO<sub>2</sub> nanopowders, obtained by SG and HT method has been performed. After heating the sample, from the room temperature up to 1100 °C, the total mass loss for both pure TiO<sub>2</sub> was 3.5%, while for the 0.5 mol% La doped TiO<sub>2</sub> and 1 mol% La doped TiO<sub>2</sub> synthesized either using SG or HT method total weight loss was around 5%. Unlike pure TiO<sub>2</sub>, the doped samples have a slightly larger mass loss. It could be found that there are two main stages for all samples, where the first step occurs from room temperature up to 200 °C for pure TiO<sub>2</sub> and for doped samples up to 180 °C. For this step the rate of mass loss is around 2.5% and it could be ascribed to the release of some adsorbed water. The second step occurs up to 450 °C and it ranges from 1% for pure up to 1.3% for all doped samples and it could mainly resulted from the combustion decomposition of some organic matters.

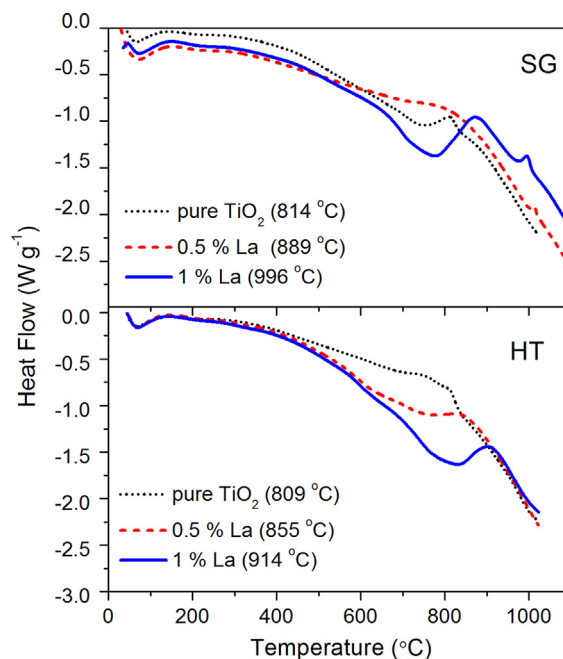


Fig. 2. DSC curves of pure and La-doped TiO<sub>2</sub> synthesized using sol–gel (a) and hydrothermal (b) methods.

In Fig. 2 DSC curves containing two broad exothermic peaks in general are presented. According to these curves, a wide peak at about 100 °C could be found, corresponding to the earlier mentioned desorption of water, as well as one highly overlapped releasing thermal peak with maxima around 350 °C, corresponding to the combustion decomposition of the organic matters. The interval from  $\sim 800$  °C to 1000 °C has exhibited an obvious decalescence phenomena, possibly resulting from the phase transition from anatase to rutile [27]. Independently, in samples obtained both by SG or HT methods, the increasing of temperature of anatase to rutile the phase transition with increased La<sup>3+</sup> concentration has been observed.

It can be concluded from the DSC curves of pure (undoped) TiO<sub>2</sub> nanopowders that the temperature of anatase to rutile phase transitions in these samples are almost the same, regardless of the process of synthesis. Also, the DSC peaks maxima are shifted towards higher temperatures with increasing concentration of La<sup>3+</sup> in the samples synthesized by both methods. Samples obtained by the SG treatment (Fig. 3a) show higher increasing of temperature of anatase to rutile phase transition with increasing La<sup>3+</sup> concentration, than samples obtained by the HT treatment (Fig. 3b). This phenomenon is directly related to the conditions of synthesis and the stoichiometric composition of the product, due to ability of La dopant to greatly inhibit anatase to rutile phase transition [28]. Generally, the temperature of the phase transition can be varied as a function of the preparation condition of the hydroxide gel (in our case, mother liquor). Namely, it has been found by studying XRD data of TiO<sub>2</sub> obtained by the sol–gel method that several weak peaks from the rutile phase appear in the sample calcined at 600 °C [29].

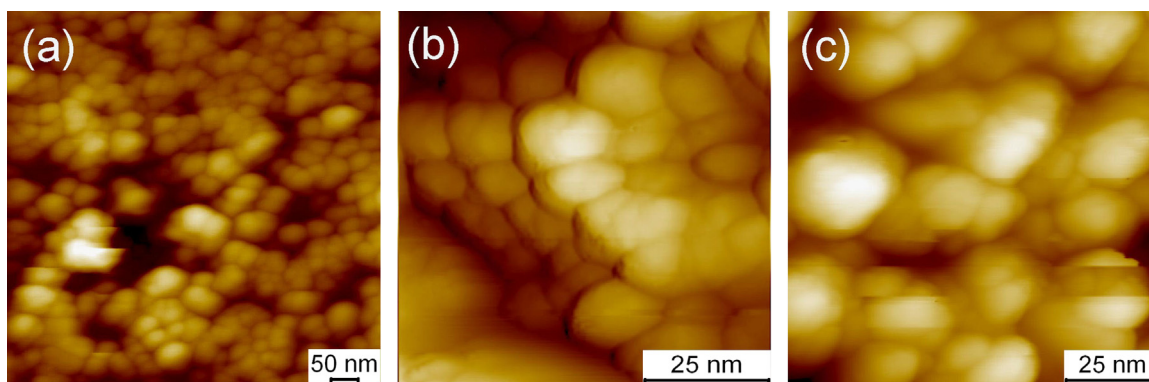


Fig. 3. The AFM images of (a) pure and (b) 0.5 wt% La doped  $\text{TiO}_2$  synthesized by SG method, and (c) HT-synthesized  $\text{TiO}_2$  nanopowder doped with 0.5 wt% La.

Table 2  
EDS results for some  $\text{TiO}_2$  nanopowders synthesized by SG and HT methods.

$\text{TiO}_2$ sample	O (wt%)	Ti (wt%)	La (wt%)	Total (wt%)
Sol-gel method				
Pure	43.28	56.72	0.00	100.00
0.5% La	47.99	52.01	0.00	100.00
1% La	43.56	55.97	0.47	100.00
Hydrothermal method				
Pure	43.16	56.84	0.00	100.00
0.5% La	43.02	56.98	0.00	100.00
1% La	43.03	56.17	0.80	100.00

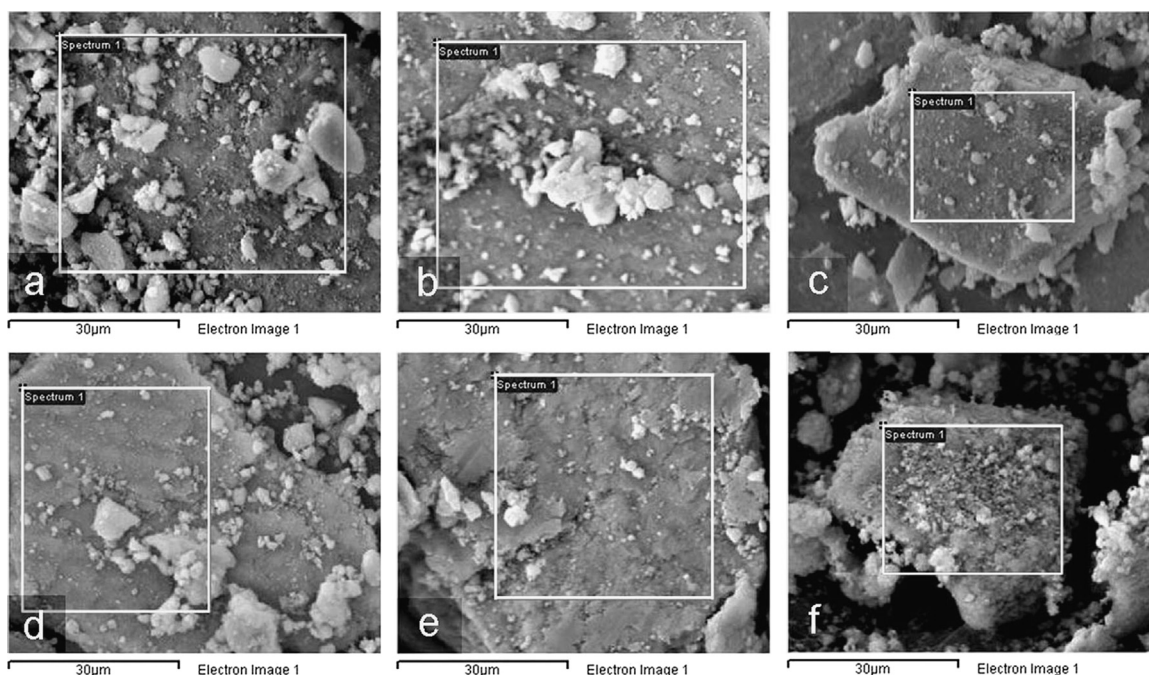


Fig. 4. The SEM images corresponding to EDS results of (a) pure, (b) 0.5 wt La doped and (c) 1 wt% La doped SG synthesized  $\text{TiO}_2$  nanopowders; (d) pure, (e) 0.5 wt La doped and (f) 1 wt% La doped HT synthesized  $\text{TiO}_2$  nanopowders.

#### 3.4. Atomic force microscopy

The NC-AFM images of pure and 0.5 mol% La-doped  $\text{TiO}_2$  samples synthesized by SG method are shown in Figs. 3(a)

and (b), respectively. In Fig. 3(c) the image of 0.5 mol% La-doped  $\text{TiO}_2$  nanopowder synthesized by the HT method is presented. It can be observed from these images that samples consist of small, spherical nanoparticles ( $\sim 15\text{--}20$  nm), as well

as greater agglomerated particles, with slightly smaller particles in the SG synthesized doped sample. These results are in good agreement with size estimation obtained by XRD analysis (Table 1).

### 3.5. SEM-EDS

The chemical composition of pure and La-doped nanopowders synthesized by SG and HT methods has been estimated by the EDS method (Table 2). The micrographs of all synthesized samples are shown in Fig. 4, whereas the EDS spectra, collected from corresponding framed areas, are presented in Fig. 5. The oxygen weight percent is similar in SG and HT synthesized nanopowders ( $\sim 43$  wt%), and above the value in stoichiometric  $\text{TiO}_2$  (40 wt%). The La content has been detected in the samples doped with 1 wt% of La: 0.47 wt%

in the SG synthesized sample, and 0.80 wt% in the HT synthesized sample. In the samples doped with 0.5 wt% of La, synthesized by both methods, the content of La could not be detected.

### 3.6. BET

In order to study the effects of synthesis method and La-doping on the pore structure and adsorption abilities of  $\text{TiO}_2$  nanopowders, BET nitrogen sorption measurements have been carried out. The parameters of porosity, determined from the  $\alpha_s$ -plots [20] obtained from the standard nitrogen adsorption isotherms have shown that the samples are fully mesoporous. In Fig. 6 the pore size distributions for pure and La-doped  $\text{TiO}_2$  nanopowders synthesized by sol-gel and hydrothermal methods, obtained by the BJH model

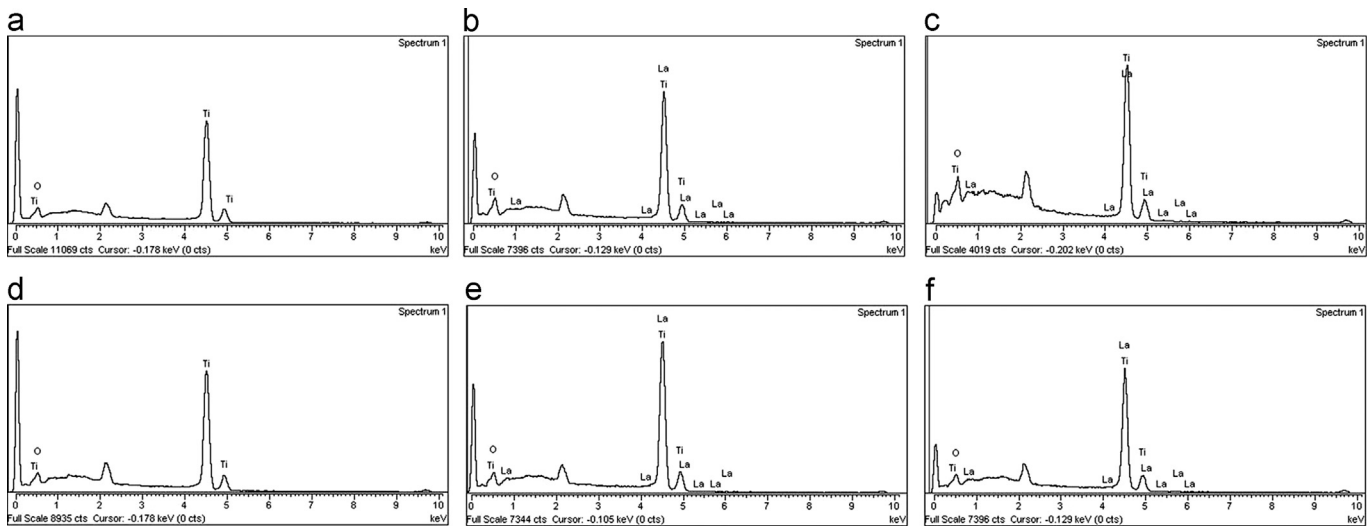


Fig. 5. The EDS spectra of (a) pure, (b) 0.5 wt% La doped and (c) 1 wt% La doped SG synthesized  $\text{TiO}_2$  nanopowders; (d) pure, (e) 0.5 wt% La doped and (f) 1 wt% La doped HT synthesized  $\text{TiO}_2$  nanopowders.

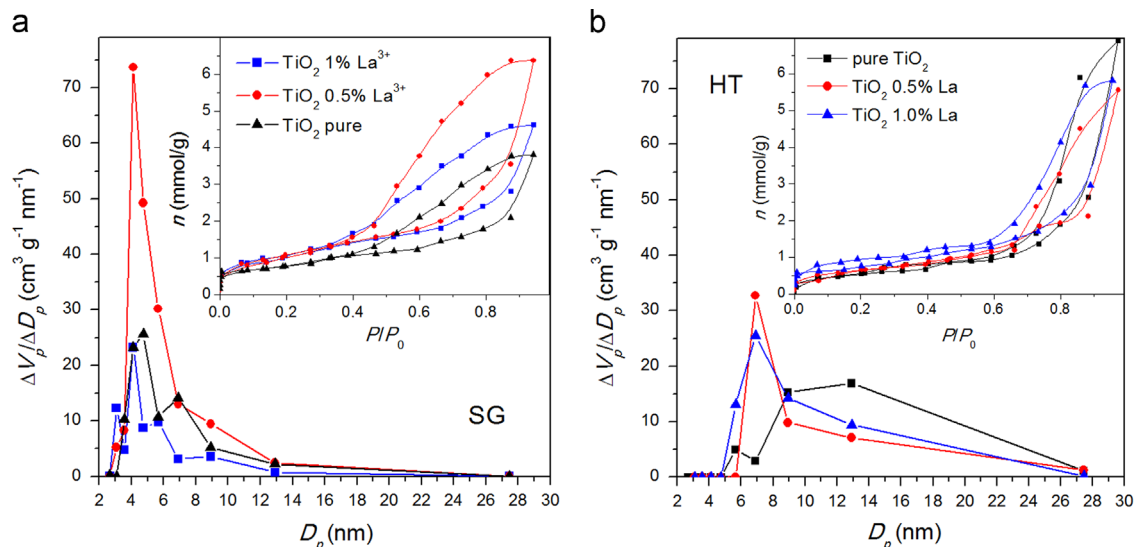


Fig. 6. The pore size distribution for pure and La-doped  $\text{TiO}_2$  nanopowders synthesized by sol-gel (a) and hydrothermal (b) methods, obtained by BJH. Corresponding adsorption/desorption isotherms given in the insets.

[21], are shown, together with corresponding adsorption/desorption curves, given in the insets.

The pore parameters of the samples have been influenced by the synthesis method and the level of La-doping: in Table 3 the values of specific surface area ( $S_{BET}$ ) and pore volume ( $V_p$ ) for sol-gel and hydrothermally synthesized nanopowders, obtained by the BET method, are listed for comparison. Namely, in the sol-gel synthesized samples, the specific surface area is increasing with the increase of La content, from  $60 \text{ m}^2 \text{ g}^{-1}$  in pure  $\text{TiO}_2$  to  $\sim 80 \text{ m}^2 \text{ g}^{-1}$  in La-doped samples (see Table 3). In hydrothermally synthesized samples  $S_{BET}$  values are lower than in the sol-gel synthesized samples. In those samples,  $S_{BET}$  is also increasing, from  $49 \text{ m}^2 \text{ g}^{-1}$  in pure  $\text{TiO}_2$  nanopowder to 51 and  $58 \text{ m}^2 \text{ g}^{-1}$  in samples doped

with 0.5 and 1 mol%, respectively (Table 3). Similar values of specific surface area have been obtained by the BJH method [21].

The mean diameters of mesopores, calculated from both BET and BJH ( $D_{BET}$ ,  $D_{BJH}$ , respectively) for the samples obtained by both synthesis routes are also listed in Table 3. It may be noticed from these data that larger pore diameters have been registered in the hydrothermally synthesized sample.

### 3.7. Raman scattering measurements

The structure of synthesized pure and La-doped  $\text{TiO}_2$  nanopowder samples have been analyzed by Raman

Table 3

The porous properties of pure and La-doped  $\text{TiO}_2$  nanopowders synthesized by sol-gel and hydrothermal methods: specific surface area ( $S_{BET}$ ,  $S_{BJH}$ ), pore volume ( $V_p$ ), and mean pore diameters ( $D_{BET}$ ,  $D_{BJH}$ ) obtained from BET and BJH methods.

	Sol-gel method			Hydrothermal method		
	Pure $\text{TiO}_2$	0.5% La	1% La	Pure $\text{TiO}_2$	0.5% La	1% La
$S_{BET} (\text{m}^2 \text{ g}^{-1}) = S_{meso}$	60	80	81	49	51	58
$V_p (\text{cm}^3 \text{ g}^{-1})$	0.133	0.222	0.161	0.241	0.194	0.203
$D_{BET} (\text{nm})$	5.7	7.2	5.1	12.6	9.8	9.0
$S_{BJH} (\text{m}^2 \text{ g}^{-1})$	62	82	81	51	50	59
$D_{BJH} (\text{nm})$	5.4	7.1	5.2	12.5	9.9	8.5

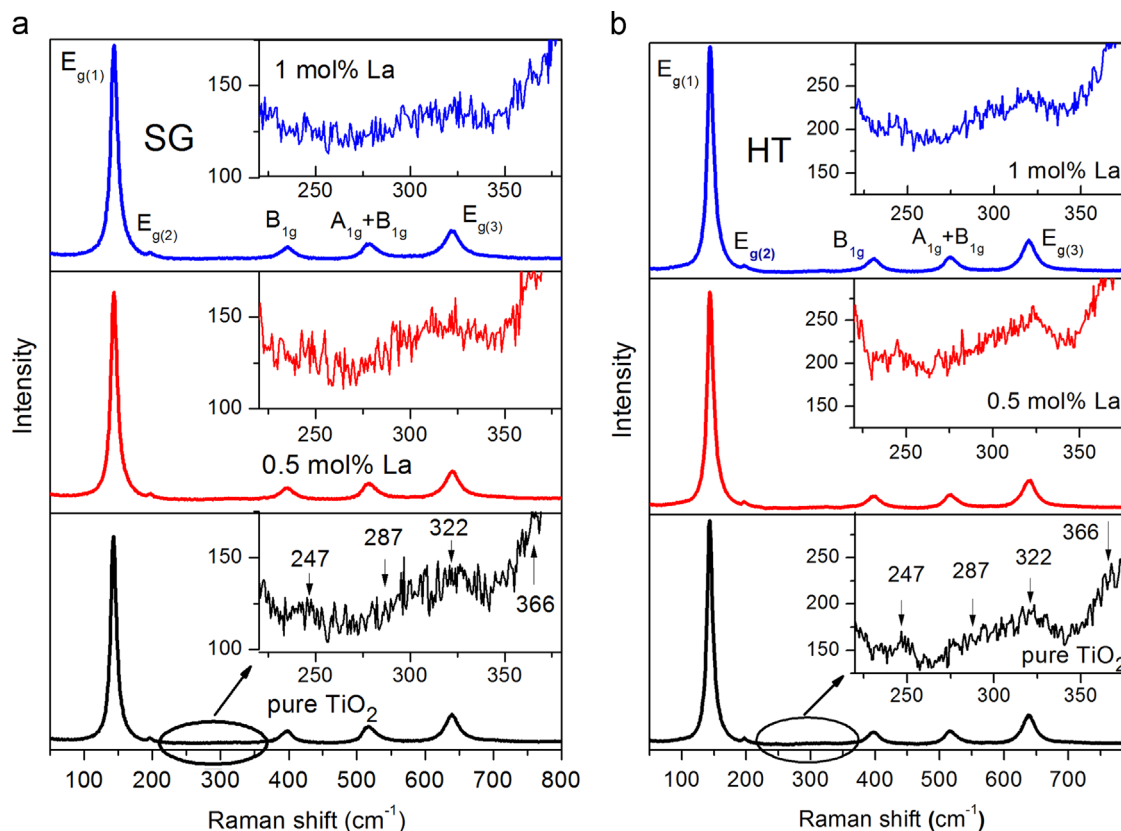


Fig. 7. The Raman spectrum of pure and La-doped  $\text{TiO}_2$  nanopowders, synthesized by sol-gel (a) and hydrothermal (b) methods, with anatase modes denoted. Insets: the spectral region of  $220\text{--}380 \text{ cm}^{-1}$  with characteristic brookite modes.

spectroscopy, to reveal the influence of synthesis method and La-doping on measured Raman spectra. The most intensive Raman features in all spectra (Fig. 7) have been assigned to anatase [30]:  $E_{g(1)}$  ( $\sim 143\text{ cm}^{-1}$ ),  $E_{g(2)}$  ( $\sim 199\text{ cm}^{-1}$ ),  $B_{1g}$  ( $\sim 399\text{ cm}^{-1}$ ),  $A_{1g}+B_{1g}$  ( $\sim 518\text{ cm}^{-1}$ ), and  $E_{g(3)}$  ( $\sim 639\text{ cm}^{-1}$ ). Greater intensity of anatase modes, measured in the HT samples, points to better crystallinity in these samples in comparison to the SG synthesized samples. Besides anatase modes, some additional features of very low intensity have been detected in the range from  $220$  to  $380\text{ cm}^{-1}$  in the Raman spectra of the samples synthesized by both sol-gel and hydrothermal method, as shown in the insets of Fig. 7(a) and (b). These features can be ascribed to the brookite phase [22]:  $A_{1g}$  ( $\sim 247\text{ cm}^{-1}$ ),  $B_{3g}$  ( $\sim 287\text{ cm}^{-1}$ ),  $B_{1g}$  ( $\sim 322\text{ cm}^{-1}$ ), and  $B_{2g}$  ( $\sim 366\text{ cm}^{-1}$ ). Low intensities and large linewidths of these modes should indicate a disorder and/or partial amorphization of the brookite phase [22,23], which is more pronounced in the sol-gel synthesized samples.

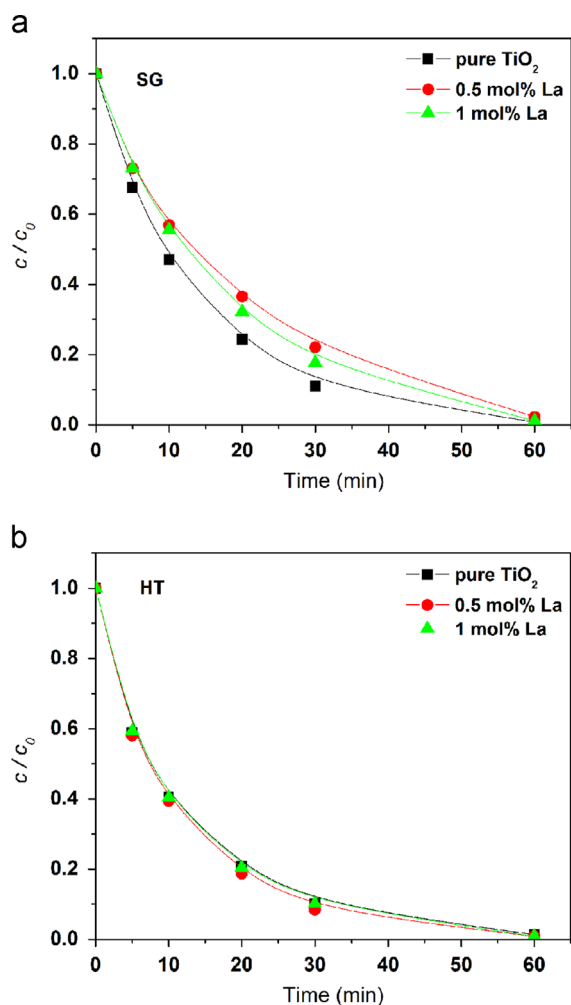


Fig. 8. The kinetics of photocatalytic degradation of alprazolam ( $c_0=0.03\text{ mmol dm}^{-3}$ ) in the presence of different types of catalyst ( $1\text{ mg cm}^{-3}$ ) under UV irradiation: (a) sol-gel and (b) hydrothermally synthesizes samples of pure and La doped  $\text{TiO}_2$  nanopowders.

Table 4

Effect of type catalyst on reaction rate constant and reaction rate of photocatalytic degradation of alprazolam ( $c_0=0.03\text{ mmol dm}^{-3}$ ).

	$k^a \times 10^2$ ( $\text{min}^{-1}$ )	$R^b \times 10^6$ ( $\text{mol dm}^{-3}\text{ min}^{-1}$ )	$r^c$
SG			
Pure $\text{TiO}_2$	7.04	2.28	0.9991
0.5 mol% La	4.97	1.61	0.9966
1 mol% La	5.63	1.82	0.9995
HT			
Pure $\text{TiO}_2$	7.68	2.49	0.9938
0.5 mol% La	8.22	2.66	0.9960
1 mol% La	7.80	2.53	0.9948

<sup>a</sup>Reaction rate constant determined for the first 20 min of irradiation.

<sup>b</sup>Reaction rate determined for the first 20 min of irradiation.

<sup>c</sup>Linear regression coefficient.

### 3.8. Photocatalysis

Influence of two different routes of synthesis and concentrations of  $\text{La}^{3+}$  on the photocatalytic activity of nanopowders was studied in photocatalytic degradation of alprazolam under UV light irradiation. The results are presented in Fig. 8. On the basis of these kinetic curves, a linear dependence of  $\ln(c/c_0)$  on the illumination time was obtained in the first period of heterogeneous photocatalysis for all synthesized samples, suggesting that the degradation reaction of the alprazolam is pseudo-first order kinetics (the linear correlation coefficients varied in the range 0.994–0.999), as shown in Table 4.

As can be seen, the presence of  $\text{La}^{3+}$  has a negative effect on the photocatalytic efficiency of nanopowders synthesized by the sol-gel method (Fig. 8(a), Table 4), while in the case of hydrothermal synthesis method  $\text{La}^{3+}$  content practically has no impact (within experimental error) on the efficiency of nanopowders in photocatalytic degradation of alprazolam (Fig. 8(b), Table 4).

When comparing photocatalytic activity of nanopowders obtained by both methods of synthesis (Fig. 8, Table 4) it can be concluded that the alprazolam degradation rate was somewhat higher in the case of used catalysts synthesized by the hydrothermal method, although the crystallite size of nanoparticles in this case were a slightly greater than nanoparticles obtained by the sol-gel method (Table 1), while the specific surface areas were slightly lower (Table 2). However, the catalysts synthesized by the hydrothermal method have greater mean pore diameter (calculated by two different methods, Table 2) than the catalyst synthesized by the sol-gel method. These relationships confirm the crucial role of pore size distribution in efficient photocatalytic degradation of relatively large pollutant molecules such as alprazolam and probably this is the reason for a slightly higher efficiency of the catalyst synthesized by the hydrothermal method. Similar results were obtained in the study of photocatalytic degradation of metoprolol by using mesoporous anatase nanopowders [22].

#### 4. Conclusion

Mesoporous TiO<sub>2</sub> nanopowders doped with La<sup>3+</sup> were prepared by the sol–gel synthesis performed at 550 °C and hydrothermal method performed at 200 °C in order to compare structural, morphological and photocatalytic properties of synthesized samples. According to XRD and Raman measurements nanoparticles with a dominant anatase phase have been obtained by both synthesis methods. These measurements have shown that slightly larger crystallites, with better crystalline structure, have been produced by HT than by the SG method. It has been observed from DSC measurements that La-doping shifted anatase-to-rutile phase transformation to higher temperatures, giving better thermal stability to these nanomaterials for applications in advanced technologies. Photocatalytic activity of synthesized nanopowders has been tested in degradation of alprazolam in water solution under UV light irradiation. A higher degradation rate has been detected for the catalysts synthesized by the hydrothermal method, in spite of their slightly greater crystallite size and lower specific surface area, in comparison to the nanoparticles obtained by the sol–gel method. Such improvement of photocatalytic performance of hydrothermally synthesized nanopowders may rather be related to their better crystallinity of both TiO<sub>2</sub> phases (anatase and brookite), as well as greater mean pore size. Also, La-doping have slightly degraded photocatalytic efficiency of nanopowders obtained by the applied sol–gel route in degradation of alprazolam, whereas there was no impact of La-content on photocatalytic performance of hydrothermally synthesized samples.

#### Acknowledgments

This work was supported by the Ministry of Education, Science and Technological Development, Republic of Serbia Projects no. III 45018, ON 171032, and ON 172042 as well as SASA Project F – 134.

#### References

- [1] A. Fujishima, T.N. Rao, D.A. Tryk, Titanium dioxide photocatalysis, *J. Photochem. Photobiol. C* 1 (2000) 1–21.
- [2] N. Daneshvar, A.R. Khataee, Removal of azo dye C.I. acid red 14 from contaminated water using Fenton, UV/H<sub>2</sub>O<sub>2</sub>, UV/H<sub>2</sub>O<sub>2</sub>/Fe(II), UV/H<sub>2</sub>O<sub>2</sub>/Fe(III) and UV/H<sub>2</sub>O<sub>2</sub>/Fe(III)/oxalate processes: a comparative study, *J. Environ. Sci. Health A* 41 (2006) 315–328.
- [3] K. Pirkanniemi, M. Sillanpää, Heterogeneous water phase catalysis as an environmental application: a review, *Chemosphere* 48 (2002) 1047–1060.
- [4] N. Daneshvar, D. Salari, A.R. Khataee, Photocatalytic degradation of azo dye acid red14 in water: investigation of the effect of operational parameters, *J. Photochem. Photobiol. A* 157 (2003) 111–116.
- [5] H. Jensen, A. Soloviev, Z. Li, E.G. Søgaard, XPS and FTIR investigation of the surface properties of different prepared titania nano-powders, *Appl. Surf. Sci.* 246 (2005) 239–249.
- [6] K.L. Yeung, A.J. Maira, J. Stolz, E. Hung, N.K.-C. Ho, A.C. Wei, J. Soria, K.-J. Chao, P.L. Yue, Ensemble effects in nanostructured TiO<sub>2</sub> used in the gas-phase photooxidation of trichloroethylene, *J. Phys. Chem. B* 106 (2002) 4608–4616.
- [7] D. Xu, L. Feng, A. Lei, Characterization of lanthanum trivalent ions/TiO<sub>2</sub> nanopowders catalysis prepared by plasma spray, *J. Colloid Interface Sci.* 329 (2009) 395–403.
- [8] K. Xu, G. Zhu, Preparation and characterization of nano-La (S, C)-TiO<sub>2</sub> oriented films by template hydrothermal synthesis, *Appl. Surf. Sci.* 255 (2009) 6691–6695.
- [9] L. Jing, X. Sun, B. Xin, B. Wang, W. Cai, H. Fu, The preparation and characterization of La doped TiO<sub>2</sub> nanoparticles and their photocatalytic activity, *J. Solid State Chem.* 177 (2004) 3375–3382.
- [10] S. Ahmed, M.G. Rasul, W.N. Martens, R. Brown, M.A. Hashib, Heterogeneous photocatalytic degradation of phenols in wastewater: a review on current status and developments, *Desalination* 261 (2010) 3–18.
- [11] M. Huerta-Fontela, M.T. Galceran, F. Ventura, Fast liquid chromatography–quadrupole-linear ion trap mass spectrometry for the analysis of pharmaceuticals and hormones in water resources, *J. Chromatogr. A* 1217 (2010) 4212–4222.
- [12] V. Calisto, V.I. Esteves, Psychiatric pharmaceuticals in the environment, *Chemosphere* 77 (2009) 1257–1274.
- [13] A. Jurado, N. Mastroianni, E. Vázquez-Suñé, J. Carrera, I. Tubau, E. Pujades, C. Postigo, M. López de Alda, D. Barceló, Drug of abuse in urban groundwater. A case study: Barcelona, *Sci. Total Environ.* 424 (2012) 280–288.
- [14] O.A.H. Jones, N. Voulvoulis, J.N. Lester, Partitioning behavior of five pharmaceuticals compounds to activated sludge and river sediment, *Arch. Environ. Contam. Toxicol.* 50 (2006) 297–305.
- [15] M. Reza Ganjali, H. Haji-Hashemi, F. Faridbod, P. Norouzi, M. Qomi, Potentiometric determination of alprazolam based on carbon paste and PVC membrane Electrodes, *Int. J. Electrochem. Sci.* 7 (2012) 1470–1481.
- [16] B. Castañeda, W. Ortiz-Cala, C. Gallardo-Cabrera, N. Sbarbati Nudelman, Stability studies of alprazolam tablets: effect of chemical interactions with some excipients in pharmaceutical solid preparations, *J. Phys. Org. Chem.* 22 (2009) 807–814.
- [17] G. Tulja Rani, D. Gowri Shankar, P. Kadgathi, B. Satyanarayana, A validated RP HPLC method for simultaneous determination of propranolol hydrochloride and alprazolam in bulk and in pharmaceutical formulations, *J. Pharm. Res.* 4 (2011) 358–360.
- [18] P. Pérez-Lozano, E. García-Montoya, A. Orriols, M. Miñarro, J.R. Ticó, J.M. Suñé-Negre, Development and validation of a new HPLC analytical method for the determination of alprazolam tablets, *J. Pharm. Biomed.* 34 (2004) 979–987.
- [19] G.K. Williamson, W.H. Hall, X-ray line broadening from fcc aluminium and wolfram, *Acta Metall.* 1 (1953) 22–31.
- [20] K. Kaneko, C. Ishii, H. Kanoh, Y. Hanzawa, N. Setoyama, T. Suzuki, Characterization of porous carbons with high resolution α<sub>s</sub>-analysis and low temperatures magnetic susceptibility, *Adv. Colloid Interface* 76–77 (1998) 295–320.
- [21] E.P. Barret, L.G. Joyner, P.P. Halenda, The determination of pore volume and area distribution in porous substances. I. computation from nitrogen isotherms, *J. Am. Chem. Soc.* 73 (1951) 373–380.
- [22] A. Golubović, B. Abramović, M. Šćepanović, M. Grujić-Brojčin, S. Armaković, I. Veljković, B. Babić, Z. Dohčević-Mitrović, Z.V. Popović, Improved efficiency of sol–gel synthesized mesoporous nanopowders in photocatalytic degradation of metoprolol, *Mater. Res. Bull.* 48 (2013) 1363–1371.
- [23] A. Golubović, M. Šćepanović, A. Kremenović, S. Aškračić, V. Berec, Z. Dohčević-Mitrović, Z.V. Popović, Raman study of the variation in anatase structure of TiO<sub>2</sub> nanopowders due to the changes of sol–gel synthesis conditions, *J. Sol–Gel Sci. Technol.* 49 (2009) 311–319.
- [24] M. Akarsu, A. Asiltürk, F. Sayilkan, N. Kiraz, E. Arpaç, H. Sayilkan, A Novel, Approach to the hydrothermal synthesis of anatase titania nanoparticles and the photocatalytic degradation of rhodamine B, *Turk. J. Chem.* 30 (2006) 333–343.
- [25] R.R. Djenadic, Lj.M. Nikolic, K.P. Giannakopoulos, B. Stojanovic, V.V. Srdic, One-dimensional titanate nanostructures: synthesis and characterization, *J. Eur. Ceram. Soc.* 27 (2007) 4339–4343.
- [26] K. Yanagisawa, J. Overstone, Crystallization of anatase from amorphous titania using the hydrothermal technique: effects of starting material and temperature, *J. Phys. Chem. B* 103 (1999) 7781–7787.

- [27] J. Liqiang, S. Xiaojun, C. Weimin, X. Zili, D. Yaoguo, F. Honggang, The preparation and characterization of nanoparticle TiO<sub>2</sub>/Ti films and their photocatalytic activity, *J. Phys. Chem. Solids* 64 (2003) 615–623.
- [28] J. Liqiang, S. Xiaojun, X. Baifu, W. Baiqi, C. Weimin, F. Honggang, The preparation and characterization of La doped TiO<sub>2</sub> nanoparticles and their photocatalytic activity, *J. Solid State Chem.* 177 (2004) 3375–3382.
- [29] T. Sugimoto, X. Zhou, A. Muramatsu, Synthesis of uniform anatase TiO<sub>2</sub> nanoparticles by sol-gel method. 3. Formation process and size control, *J. Colloid Interface Sci.* 259 (2003) 43–52.
- [30] T. Ohsaka, F. Izumi, Y. Fujiki, Raman spectra of anatase, TiO<sub>2</sub>, *J. Raman Spectrosc.* 7 (1978) 321–324.

Nanocrystalline CeO<sub>2-δ</sub> as Effective Adsorbent of Azo Dyes

Nataša M. Tomić,<sup>†</sup> Zorana D. Dohčević-Mitrović,<sup>\*,†</sup> Novica M. Paunović,<sup>†</sup> Dušan Ž. Mijin,<sup>‡</sup> Nenad D. Radić,<sup>§</sup> Boško V. Grbić,<sup>§</sup> Sonja M. Aškračić,<sup>†</sup> Biljana M. Babić,<sup>||</sup> and Danica V. Bajuk-Bogdanović<sup>⊥</sup>

<sup>†</sup>Institute of Physics, University of Belgrade, Pregrevica 118, 11080 Belgrade, Serbia

<sup>‡</sup>Faculty of Technology and Metallurgy, University of Belgrade, Karnegijeva 4, 11000 Belgrade, Serbia

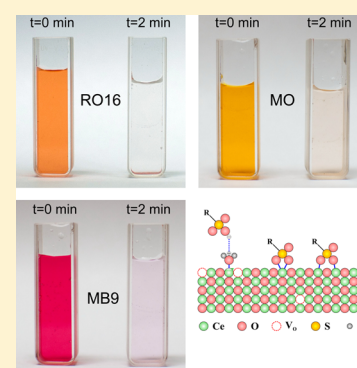
<sup>§</sup>ICChTM, Department of Catalysis and Chemical Engineering, University of Belgrade, Njegoševa 12, 11000 Belgrade, Serbia

<sup>||</sup>Institute of Nuclear Sciences "Vinča", University of Belgrade, 11001 Belgrade, Serbia

<sup>⊥</sup>Faculty of Physical Chemistry, University of Belgrade, Studentski Trg 12-16, 11000 Belgrade, Serbia

**S** Supporting Information

**ABSTRACT:** Ultrafine CeO<sub>2-δ</sub> nanopowder, prepared by a simple and cost-effective self-propagating room temperature synthesis method (SPRT), showed high adsorption capability for removal of different azo dyes. Batch type of adsorption experiments with fixed initial pH value were conducted for the removal of Reactive Orange 16 (RO16), Methyl Orange (MO), and Mordant Blue 9 (MB9). The equilibrium adsorption data were evaluated using Freundlich and Langmuir isotherm models. The Langmuir model slightly better describes isotherm data for RO16 and MO, whereas the Freundlich model was found to best fit the isotherm data for MB9 over the whole concentration range. The maximum adsorption capacities, determined from isotherm data for MO, MB9, and RO16 were 113, 101, and 91 mg g<sup>-1</sup> respectively. The adsorption process follows the pseudo-second-order kinetic model indicating the coexistence of chemisorption and physisorption. The mechanism of azo dye adsorption is also discussed.

**■ INTRODUCTION**

Synthetic dyes are widely used in a number of industries such as textile and leather industries, paper printing, cosmetics, and pharmaceuticals. It is estimated to be more than 10 000 commercially available dyes with over  $7 \times 10^5$  tons of dyestuff produced annually.<sup>1,2</sup> Azo dyes represent about 60–70% of the dyes used in the textile industry. Some of them show aquatic toxicity or allergenic effects, and under reductive conditions they produce aromatic amines that are carcinogenic.<sup>2,3</sup> Azo dyes represent a class of synthetic, colored, organic compounds, which are characterized by the presence of one or more azo bonds. These dyes belong to the most toxic ones compared to other forms of dyes.<sup>1</sup> Large quantities of these dyes (10–15% of the total world production) are released into the wastewater (typical concentration 10–200 mg L<sup>-1</sup>), the presence of which poses a major threat to the aquatic organisms as well as animals and humans because of their nonbiodegradability, toxicity, and potential carcinogenic nature.<sup>4–6</sup>

Dye removal from textile effluents is a major environmental problem because of the difficulty to treat such streams by conventional physicochemical and biological treatment methods. The methods such as filtration, coagulation, flocculation, ion exchange, and photocatalytic degradation are unsatisfactory for wastewater treatment because they are expensive and may produce more toxic byproducts. Among the various available water treatment techniques, adsorption is the most reliable and efficient technique for dye removal, despite the fact that usually

the adsorbent needs to be regenerated, which increases the cost of the process and can be a time-consuming procedure. The liquid phase adsorption has been shown to be an efficient way for removing the suspended solids, organic matter, and oil from aqueous solutions. Adsorption appears to offer the best perspective over all the other treatments because it can handle fairly large flow rates, producing a high quality effluent and does not result in the formation of harmful substances, such as ozone and free radicals which are present during the photodegradation process using UV.

Activated carbon is the most widely used adsorbent for this purpose, because it has a high surface area and high capacity for adsorption of organic matter, but its use is limited because of its high production cost and significant problems with the regeneration of the spent activated carbon.<sup>7,8</sup> A great variety of low-cost biomass materials<sup>9–13</sup> have been used to produce activated carbon for the treatment of wastewaters. In recent years, low cost agricultural wastes have been investigated as potential biosorbents,<sup>14</sup> but most of these cheap substitutes have to be subjected to the process of carbonization which increases process costs. Therefore, there is still a high demand for cheaper adsorbent materials with high adsorption capacity.

**Received:** March 6, 2014

**Revised:** September 8, 2014

**Published:** September 14, 2014



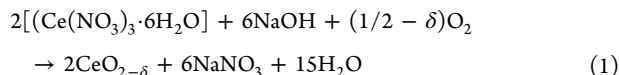
Nowadays, nanoscience and nanotechnology play important role in environmental protection. There is a strong need to develop simple and economical methods for producing nanomaterials with higher adsorption rates which can efficiently remove various contaminants. Nanomaterials with high surface area are the most promising candidates as adsorbents in organic dye removal.<sup>5,15–19</sup>

Among various metal oxide semiconductors, CeO<sub>2</sub> is widely used in many application areas such as catalysis, fuel cells, sensors, and UV shielding, owing to its outstanding physical and chemical properties. The application of ceria as effective sorbent is not so often studied. There are few reports in which it is demonstrated that ceria is effective sorbent for the removal of high toxic pollutants such as<sup>17</sup> As(V) and Cr(VI) and azo dyes such as Congo Red<sup>18</sup> or Acid Orange<sup>4</sup> from water. The adsorption experiments, performed to remove Reactive Orange 16 and Methyl Orange from wastewaters, mainly used as adsorbent waste biomass,<sup>20</sup> various types of sludge, and biosorbents.<sup>1,13,14,20–26</sup> Although most of these sorbents were relatively cheap and effective in dye removal, they showed modest and rarely high sorption capacities. On the other side, to the best of our knowledge there is almost no study which concerns the adsorption of Mordant Blue 9.

Herein we present the adsorption capability of ceria nanoparticles for removal of different azo dyes such as Reactive Orange 16, Methyl Orange, and Mordant Blue 9. Ceria nanopowder, obtained by a simple and cost-effective method, has shown very high efficiency toward azo dye removal and has been proven to be a promising alternative for wastewater treatment.

## ■ EXPERIMENTAL SECTION

**1. Materials Preparation.** The ultrafine CeO<sub>2-δ</sub> nanopowder was fabricated via a simple and economical self-propagating room temperature synthesis method (SPRT).<sup>27,28</sup> Starting reactants were cerium nitrate hexahydrate (Ce(NO<sub>3</sub>)<sub>3</sub>·6H<sub>2</sub>O) (Acros Organics 99.5%) and sodium hydroxide (Carlo Erba). Hand-mixing of nitrate with NaOH was performed in alumina mortar for ~10 min until the mixture turned light brown. After being exposed to air for 4 h, the mixture was suspended in water. Rinsing of NaNO<sub>3</sub> was performed in a centrifuge at 3500 rpm for 10 min. This procedure was performed four times with distilled water and twice with ethanol. The precipitate was dried at 60 °C overnight. The reaction based on the self-propagating room temperature method can be written as follows:



**2. Characterization Methods.** X-ray powder diffraction (XRD) data of the sample were collected on a Siemens D-5000 diffractometer with Cu K $\alpha$  radiation over the 2 $\theta$  range from 20° to 80°. Atomic force microscope (AFM) images were taken using the Omicron B002645 SPM PROBE VT AFM 25 instrument in noncontact mode at room temperature. The powder specific surface area of the sample was calculated following the multipoint BET procedure on the Quantachrome ChemBet-3000 setup. The pore size distribution was derived from nitrogen adsorption-desorption isotherm obtained at 77 K. The infrared (IR) transmission spectra of CeO<sub>2-δ</sub> pellets before and after dye adsorption were measured on a Thermo Nicolet 6700 Fourier transform infrared spectrophotometer at room temperature. Micro-Raman spectra were collected in the backscattering configuration using the TriVista 557 Raman system. The 488 nm line of an Ar<sup>+</sup>/Kr<sup>+</sup> mixed gas laser was used as an excitation source. In order to avoid sample heating, the incident laser power on the samples was kept below 20 mW. Surface charge (zeta potential) of ceria nanoparticles at different pH was measured using Zetasizer Nano ZS90 (Malvern

Instruments) apparatus. Suspensions were prepared using deionized water as dispersing medium and were ultrasonicated for 15 min prior to the measurements using an ultrasonic bath. The pH values of suspensions were adjusted by adding HCl and NaOH solutions to the starting suspension of CeO<sub>2-δ</sub> nanopowder.

**3. Adsorption Experiments.** The adsorption experiments were carried out as batch tests in a magnetically stirred thermostated glass vessel with three different concentrations (50, 100, and 200 mg L<sup>-1</sup>) of Reactive Orange 16 (RO16), Methyl Orange (MO), and Mordant Blue 9 (MB9). All measurements were performed at initial pH values of 6.2, 6, and 4.6 for MO, MB9, and RO16 dye solutions, respectively. The suspensions were stirred for 2 min at room temperature in the dark. The adsorption capacity (for the 200 mg L<sup>-1</sup> concentration of dyes) of coconut-based powdered activated carbon (PAC), of large specific surface area (1200 m<sup>2</sup>/g), was determined for comparison. The working volume (25 mL) and the quantity of ceria nanopowders and PAC (50 mg) were kept fixed in all adsorption experiments. At fixed contact time, the samples were taken, centrifuged, and analyzed on a Shimadzu 1700 UV-vis spectrophotometer within the spectral range where maximum absorption for each dye occurs. In Table S1 (see the Supporting Information) are given the chemical structure and the wavelength of maximal absorption ( $\lambda_{\text{max}}$ ) for each dye.

## ■ RESULTS AND DISCUSSION

The powder XRD pattern of CeO<sub>2-δ</sub> nanopowder is presented in Figure 1a. Diffraction peaks corresponding to cubic fluorite structure are clearly observed. All XRD peaks are broadened, indicating that the crystallite size is within the nanometer range. The average size of CeO<sub>2-δ</sub> nanocrystals, estimated by the Williamson-Hall method,<sup>29</sup> is about 6 nm. The noncontact AFM image of CeO<sub>2-δ</sub> sample (Inset of Figure 1b) shows small and agglomerated nonporous CeO<sub>2-δ</sub> particles. The pores between agglomerated CeO<sub>2-δ</sub> nanoparticles are also visible on the AFM image. Particle size distribution obtained from the AFM image of CeO<sub>2-δ</sub> sample is presented in Figure 1b, and it was modeled by asymmetric double sigmoidal function. The average particle size is 11.4 nm.

To determine the surface area and pore size distribution, nitrogen adsorption-desorption isotherms at 77 K were recorded, and these are given in the inset of Figure 1c. According to the IUPAC classification,<sup>30</sup> the nitrogen adsorption-desorption isotherm is attributed to the Langmuir IV type. The pore size distribution was determined from the desorption branch of the isotherms using the BJH (Barrett-Joyner-Halenda) method and is shown in Figure 1c. It can be observed that the sample has bimodal pore size distribution in the mesoporous area with the first mode peak around 2 nm and the second one in the range 3–4 nm. The value of the BET specific surface area ( $S_{\text{BET}}$ ) is 74 m<sup>2</sup> g<sup>-1</sup>.

Further, we examined the performances of CeO<sub>2-δ</sub> nanopowder as a potential adsorbent for removal of RO16, MO, and MB9. The adsorption measurements were carried out with three different concentrations of the dye solutions (50, 100, and 200 mg L<sup>-1</sup>), and absorption spectra of the dye solutions were collected after certain time intervals. The UV-vis spectrum of RO16 is given in Figure 2a (blue line) for the concentration of 50 mg L<sup>-1</sup>. The absorption spectrum of RO16 in the presence of CeO<sub>2-δ</sub> nanoparticles after 2 min is also presented in Figure 2a (red line). As can be seen, the RO16 characteristic bands decreased promptly, indicating that RO16 was removed from the solution. The corresponding photo image (right panel of Figure 2a) shows that the solution is almost colorless. The absorption spectra of the MO and MB9 before (blue line) and after 2 min (red line) in the presence of CeO<sub>2-δ</sub> nanoparticles are given in Figure 2b,c. Absorption spectra of these two dye

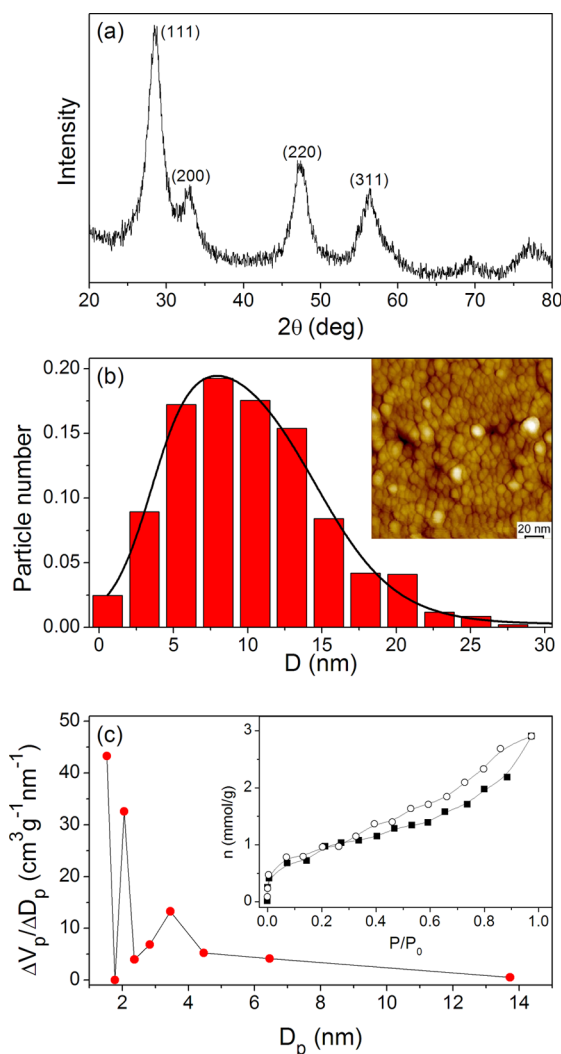


**Figure 1.** XRD spectrum (a), particle size distribution obtained from AFM (b), and pore size distribution curve obtained from the desorption branch of the isotherm (c) for CeO<sub>2-δ</sub> nanopowder. Insets present the AFM image and the nitrogen adsorption-desorption isotherm of CeO<sub>2-δ</sub> nanopowder.

solutions after 2 min showed that the dyes were present in a very low concentration. From the photo images (right panel of Figure 2b,c), it can be noticed that the solutions were almost colorless after 2 min. The experiment was repeated with an increased concentration for all three dyes (100 mg L<sup>-1</sup>), and the obtained results were similar.

The concentration of RO16 in the solution was further increased to 200 mg L<sup>-1</sup>. The absorption spectra of RO16 dye solution in the presence of CeO<sub>2-δ</sub> nanoparticles, presented in Figure S1a (Supporting Information), demonstrate that CeO<sub>2-δ</sub> quickly removes the RO16 from the solution. After 40 min, the equilibrium state was reached. The adsorption measurements were also performed on the solutions of MO and MB9 (200 mg L<sup>-1</sup>) in the presence of CeO<sub>2-δ</sub> nanopowder, in order to compare the efficiency of adsorption process onto ceria nanopowder for all three dyes. The adsorption capacity of CeO<sub>2-δ</sub> nanopowder was determined from the mass balance relationship:<sup>1,13,15,22</sup>

$$q_e = \frac{(C_0 - C_e)V}{m} \quad (2)$$

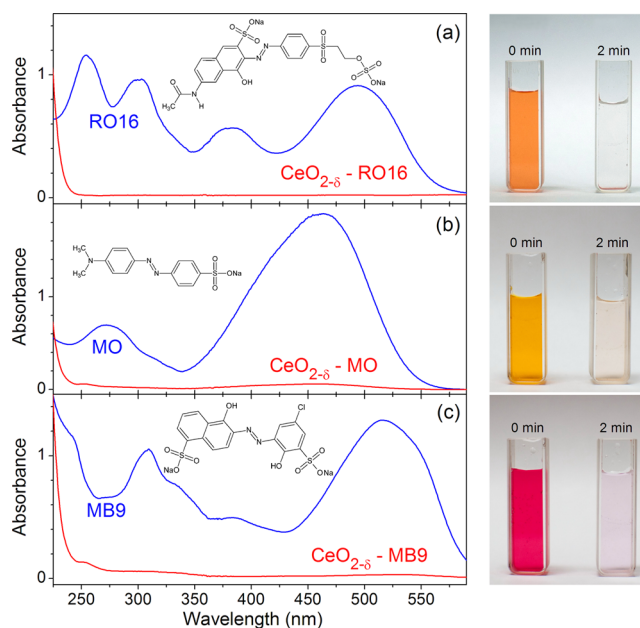


**Figure 2.** Absorption spectra with corresponding photo images of (a) RO16, (b) MO, and (c) MB9 dye solutions (50 mg L<sup>-1</sup>) before and 2 min after introducing CeO<sub>2-δ</sub> nanoparticles (2 g L<sup>-1</sup>). Mass of adsorbent = 50 mg; solution volume = 25 mL.

where  $q_e$  represents the amount of dye adsorbed per unit mass of adsorbent (mg g<sup>-1</sup>),  $C_0$  and  $C_e$  are the initial and equilibrium liquid phase concentrations (mg L<sup>-1</sup>), respectively,  $V$  is the volume of the solution (L), and  $m$  is the mass (g) of CeO<sub>2-δ</sub> used.

The adsorption rate and the amount of adsorbed dye with contact time for the solutions of RO16, MO, and MB9 (200 mg L<sup>-1</sup>) are illustrated in Figure 3a,b. As can be noticed from Figure 3, for all three curves, it is characteristic that the adsorption process is rapid in the initial stage, whereas in the later stage it becomes much slower. The adsorption rate for RO16 was higher at the beginning, but after 60 min much better elimination of MO from the solution was observed, whereas the adsorption rate of MB9 was still lower. The equilibrium was achieved after 40 (60) min for RO16 (MO), whereas for MB9 it was achieved after 180 min. The adsorption capacities of CeO<sub>2-δ</sub> nanopowder in the case of MO, MB9, and RO16 were 100, 94, and 91 mg g<sup>-1</sup>, respectively.

Further, the adsorption capacities of CeO<sub>2-δ</sub> nanopowder and activated carbon were compared. The adsorption capacity of commercial activated carbon (50 mg) is presented in Figure 4 for MO (a), RO16 (b), and MB9 (c) solutions (200 mg L<sup>-1</sup>). In the case of MO dye solution, it can be noticed that at the beginning of the adsorption process the activated carbon was slightly faster than CeO<sub>2-δ</sub> nanopowder and reached the equilibrium state after 20 min. After 60 min, both curves overlapped. In the case of RO16 dye solution, activated carbon was much slower compared to CeO<sub>2-δ</sub>. After 40 min, CeO<sub>2-δ</sub> nanopowder reached equilibrium and eliminated almost 90% of RO16 from the solution, whereas activated carbon needed 2 h to reach the final adsorption capacity of 85 mg g<sup>-1</sup> which was still lower than that of ceria nanopowder (91 mg g<sup>-1</sup>). The adsorption capability of CeO<sub>2-δ</sub> for MB9 is lower than that for activated carbon, although after 2 h the final adsorption capacities were comparable.

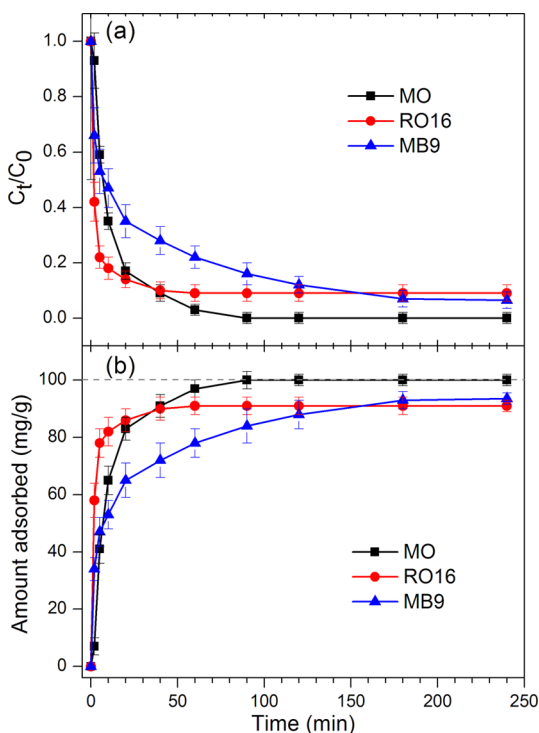


**Figure 3.** Adsorption rate (a) and amount of adsorbed dyes (b) for the solutions of MO, RO16, and MB9 ( $200 \text{ mg L}^{-1}$ ) in the presence of  $\text{CeO}_{2-\delta}$  nanopowder. Mass of adsorbent = 50 mg; solution volume = 25 mL.

In Figure 5a–c are shown the IR transmission spectra of pure dyes and  $\text{CeO}_{2-\delta}$  nanopowders after dye adsorption. For comparison, the IR spectrum of pure  $\text{CeO}_{2-\delta}$  nanopowder is also given in Figure 5a–c.

The IR spectra of pure dyes have some common characteristic bands.<sup>4,6,31–36</sup> The bands at  $1040/1120 \text{ cm}^{-1}$  in MO,  $1054/1139 \text{ cm}^{-1}$  in RO16, and  $1044/1136 \text{ cm}^{-1}$  in MB9 originate from the symmetric stretching vibrations of the  $\text{SO}_3^-$  group ( $\nu_s(\text{SO}_3^-)$ ). The band at  $1204 \text{ cm}^{-1}$  in MO,  $1236 \text{ cm}^{-1}$  in RO16, and  $1190 \text{ cm}^{-1}$  in MB9 represents the asymmetric stretching vibrations of the  $\text{SO}_3^-$  group ( $\nu_{as}(\text{SO}_3^-)$ ). The band at  $1368 \text{ cm}^{-1}$  in MO and  $1372 \text{ cm}^{-1}$  in RO16 belongs to the C–N stretching vibrations. The bands at  $1422$ ,  $1410$ , and  $1409 \text{ cm}^{-1}$  in MO, RO16, and MB9, respectively, are assigned to the N=N stretching vibrations. The bands at  $1520/1608 \text{ cm}^{-1}$  in MO and  $1586 \text{ cm}^{-1}$  in RO16 are from the aromatic ring stretching vibrations. The band at  $1672 \text{ cm}^{-1}$  in the spectra of RO16 originates from the stretching vibrations of the carbonyl C=O group.

In the IR spectrum of MO dye adsorbed on  $\text{CeO}_{2-\delta}$  (shown in Figure 5a), the IR bands of the MO dye are of much lower intensity. The pronounced changes of the IR bands characteristic for sulfonate stretching vibration mode are observed. The  $\nu_{as}(\text{SO}_3^-)$  band at  $1204 \text{ cm}^{-1}$  is much weaker after MO adsorption on  $\text{CeO}_{2-\delta}$  and shifted to  $\sim 1193 \text{ cm}^{-1}$  (marked with arrow in Figure 5a). The  $\nu_s(\text{SO}_3^-)$  band at  $1040 \text{ cm}^{-1}$  in MO is slightly shifted to  $1034 \text{ cm}^{-1}$  (marked with arrow in Figure 5a) in the  $\text{CeO}_2\text{-MO}$  spectrum, the intensity of which is much lower after adsorption. All these changes can indicate that the sulfonate group is strongly involved in the adsorption of MO onto  $\text{CeO}_{2-\delta}$ .<sup>34</sup> In the IR spectrum of RO16 adsorbed onto  $\text{CeO}_{2-\delta}$  (Figure 5b), a significant intensity decrease of the IR bands at  $1054/1139$  and  $1500 \text{ cm}^{-1}$ , characteristic for  $\text{SO}_3^-$

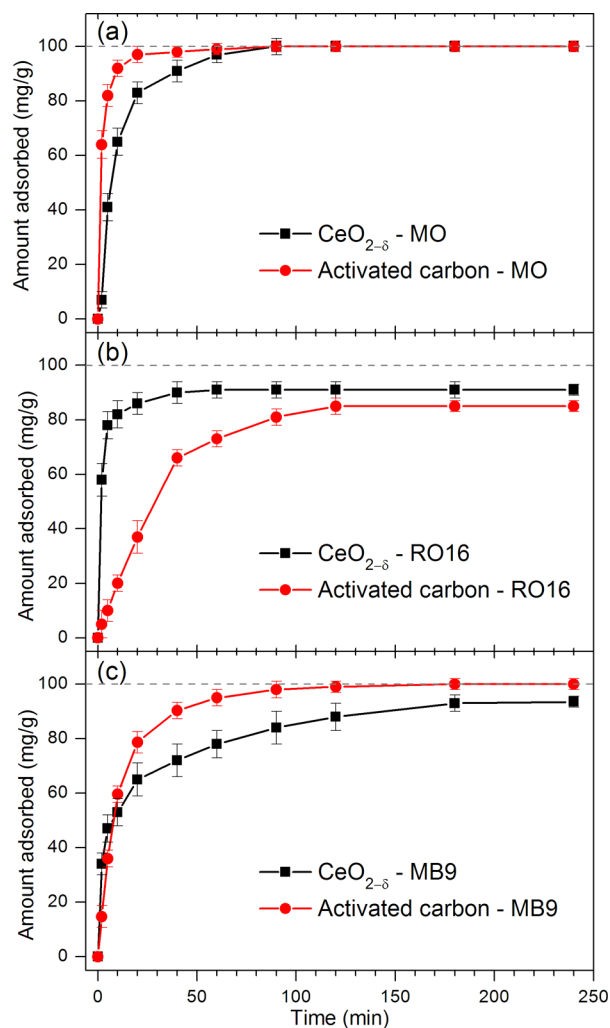


**Figure 4.** Comparison of adsorption capacities between  $\text{CeO}_{2-\delta}$  nanopowder and activated carbon in the case of (a) MO, (b) RO16, and (c) MB9 dye solutions ( $200 \text{ mg L}^{-1}$ ). Mass of adsorbent = 50 mg; solution volume = 25 mL.

group and N–H bending vibrations,<sup>4,6</sup> is observed too. Many other bands which belong to pure RO16 dye are much weaker or barely visible in the  $\text{CeO}_{2-\delta}$ -RO16 spectrum, as for instance the band at  $1410 \text{ cm}^{-1}$  for N=N stretching vibrations. The carbonyl C=O peak at  $1672 \text{ cm}^{-1}$  in the IR spectrum of RO16, is almost absent from the  $\text{CeO}_{2-\delta}$ -RO16 spectrum. The  $\nu_s(\text{SO}_3^-)$  band is shifted from  $1139$  to  $1136 \text{ cm}^{-1}$  in the  $\text{CeO}_{2-\delta}$ -RO16 spectrum. In the IR spectrum of  $\text{CeO}_{2-\delta}$ -MB9 (Figure 5c), a major decrease of the MB9 band intensity is observed and the slight shift of the asymmetric  $\nu_s(\text{SO}_3^-)$  band is barely visible (marked with arrow in Figure 5c). All this indicates that RO16 and MB9 are also strongly adsorbed onto the  $\text{CeO}_{2-\delta}$  surface. In Figure 5d is presented the IR transmission spectrum of pure  $\text{CeO}_{2-\delta}$  in the extended spectral range. As can be seen, strong bands near  $3400$  and  $1620 \text{ cm}^{-1}$  are attributed to the adsorbed  $\text{H}_2\text{O}$  and hydroxyls.<sup>37,38</sup> The absorption band at  $1384 \text{ cm}^{-1}$  originates from  $\text{CO}_2$  molecule vibrations.

Raman spectra, obtained on  $\text{CeO}_{2-\delta}$  nanopowder before and after dye adsorption, are presented in Figure 6 and are consistent with the IR measurements. In the Raman spectra of nanocrystalline  $\text{CeO}_{2-\delta}$  treated with dyes, besides the  $\text{F}_{2g}$  mode of pure  $\text{CeO}_{2-\delta}$  positioned at  $\sim 456.5 \text{ cm}^{-1}$  and the mode at

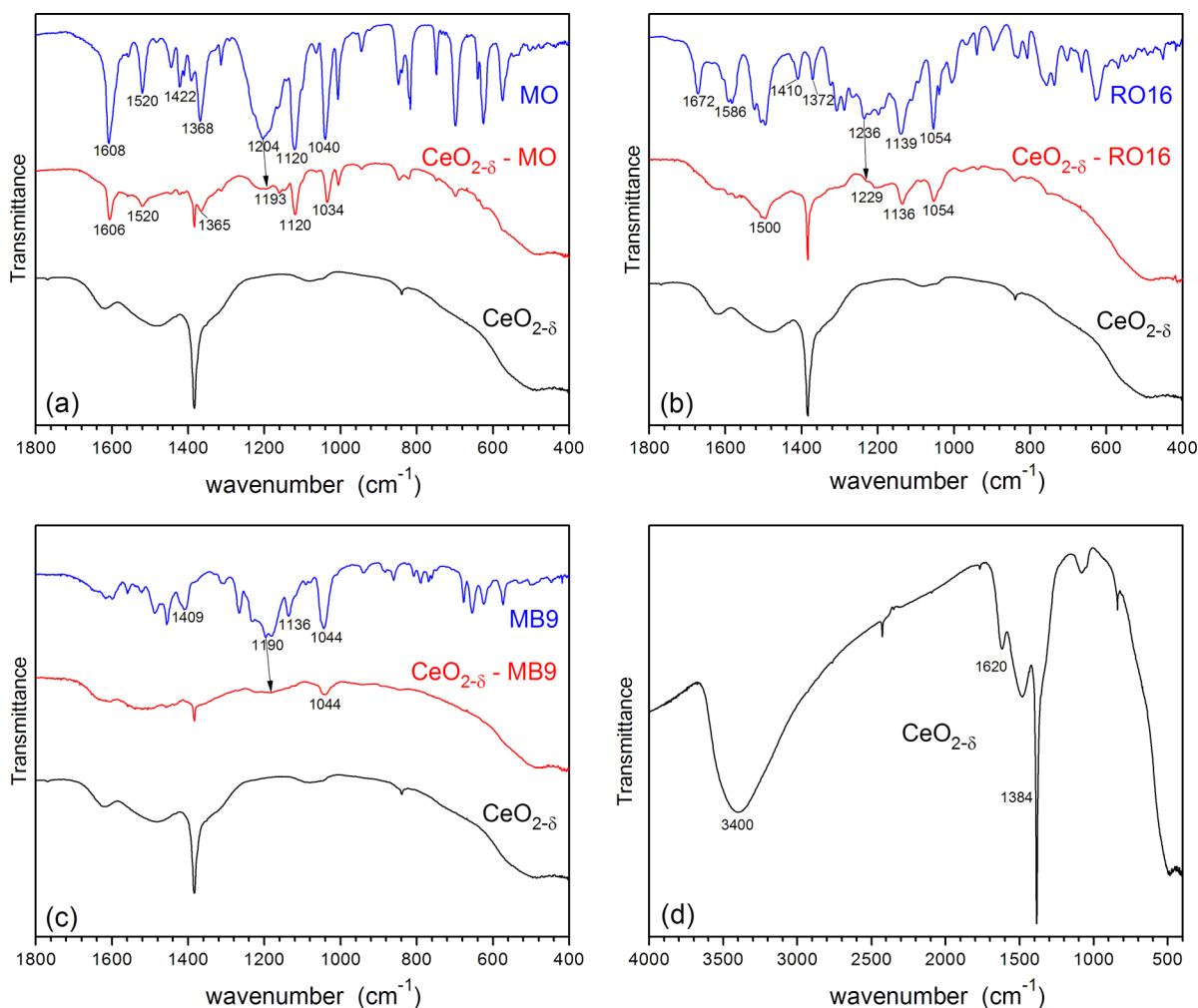


**Figure 5.** IR transmission spectra of (a) MO, (b) RO16, and (c) MB9 adsorbed on  $\text{CeO}_{2-\delta}$  together with the transmission spectra of pure dyes and  $\text{CeO}_{2-\delta}$  nanopowder. (d) IR transmission spectrum of  $\text{CeO}_{2-\delta}$  nanopowder in the extended range.

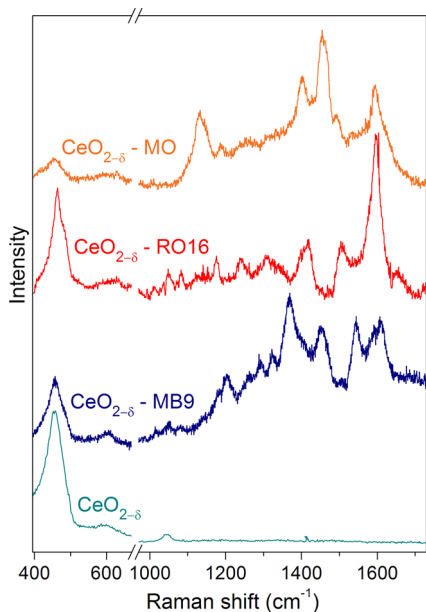


**Figure 6.** Room temperature Raman spectra of  $\text{CeO}_{2-\delta}$  nanopowder before and after adsorption of MO, RO16, and MB9 dyes.

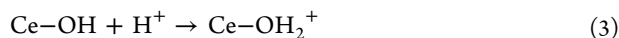
$\sim 600 \text{ cm}^{-1}$  which belongs to intrinsic oxygen vacancies,<sup>39</sup> additional modes are observed. These new modes correspond to the vibrations of different atomic groups of dye molecules, such as  $-\text{N}=\text{N}-$ ,  $-\text{C}=\text{O}$ ,  $-\text{S}=\text{O}$ ,  $-\text{O}-\text{H}$ , and aromatic ring vibrations. The most prominent mode frequencies deduced from the spectra of ceria treated with MO, RO16, and MB9 are summarized in the Table S2 (see the Supporting Information). As the majority of the atomic group vibrations characteristic for the dye molecules in question are observed in the Raman spectra of dyed ceria nanopowder, it can be concluded that in all three cases the adsorption of dye molecules took place.

The IR and Raman spectra unambiguously showed that MO, RO16, and MB9 are adsorbed on  $\text{CeO}_{2-\delta}$  surface. In addition, from the IR spectra of three azo dyes adsorbed on  $\text{CeO}_{2-\delta}$  nanopowders, we concluded that  $\nu_{\text{as}}$  and  $\nu_{\text{s}}$  bands of sulfonate groups are affected considerably. The intensity ratio of these bands ( $\nu_{\text{as}}(\text{SO}_3^-)/\nu_{\text{s}}(\text{SO}_3^-) = 0.4$ ) for adsorbed MO onto ceria is different from the same ratio in the spectrum of isolated MO ( $\nu_{\text{as}}(\text{SO}_3^-)/\nu_{\text{s}}(\text{SO}_3^-) = 0.9$ ). The changes of the  $\nu_{\text{as}}$  and  $\nu_{\text{s}}$  band intensities of sulfonate groups are also registered in the IR spectra of adsorbed RO16 and MB9 onto ceria. It is further worth mentioning that the frequency difference  $\Delta\nu_{\text{as-s}}$  ( $\nu_{\text{as}}(\text{SO}_3^-) - \nu_{\text{s}}(\text{SO}_3^-)$ ) in the MO, RO16, and MB9 spectra is higher than that in the corresponding spectra of adsorbed dyes on ceria (see Figure 5). This is characteristic of the

bidentate type coordination according to the Deacon and Phillips<sup>40</sup> empirical rule and the work of Bauer et al.,<sup>41</sup> formed when OH groups situated on the surface metal cations are substituted with oxygen atoms from azo dyes. Ji et al.<sup>4</sup> noticed similar changes to ours in the IR spectra of acid orange adsorbed onto CeO<sub>2</sub> surface and proposed that a bidentate type bridge is formed between sulfonate group and Ce<sup>4+</sup> cations. According to the observed changes in the IR spectra of MO, RO16, and MB9 adsorbed on CeO<sub>2-δ</sub> nanopowder, it is reasonable to assume that all three dyes form a bidentate type bridge on the ceria surface, where two oxygen atoms of the SO<sub>3</sub><sup>-</sup> group are bound to one or two Ce<sup>4+</sup> cations in a process that involves the substitution of surface coordinated OH groups on Ce<sup>4+</sup> cations with oxygen atoms from azo dyes.

Another very important factor for dye removal concerns the capability of CeO<sub>2-δ</sub> nanopowders to easily form oxygen vacancies on the surface which accompany functional groups. The surface functional groups can interact with dye molecules via hydrogen bonds and/or electrostatic forces promoting the adsorption of dye molecules. The first principle density functional theory calculations performed by Yang et al.<sup>42</sup> have shown that, in oxygen deficient ceria, the adsorbed water molecules prefer to decompose near the oxygen vacancy site, forming surface hydroxyls, where H atoms are bonded with surface oxygen atoms. Therefore, they concluded that in reduced ceria both adsorbed H<sub>2</sub>O and surface hydroxyls coexist. Their calculations are in good agreement with experimental work of Kundakovic et al.<sup>43</sup> performed on oxidized and reduced CeO<sub>2</sub> thin films, who detected surface hydroxyls only in reduced ceria films.

Having in mind that our ceria is oxygen deficient, it is reasonable to assume that hydroxyl groups, already observed in the IR spectra, are present on the surface of CeO<sub>2-δ</sub> nanopowder. The experimental determination of the pH value at zero point charge (pH<sub>ZPC</sub>) revealed that CeO<sub>2-δ</sub> has pH<sub>ZPC</sub> = 6.3 (Figure S2 in the Supporting Information). As pH values of the dye solutions are lower than pH<sub>ZPC</sub> of CeO<sub>2-δ</sub> (see section 3 in Experimental Section), CeO<sub>2-δ</sub> as adsorbent acts as a positive surface. The electrostatic attraction between ceria nanoparticles and negatively charged dye ions is an operable mechanism. In that case, the ceria surface hydroxyls are protonated:



In aqueous solution, the sulfonate groups (R-SO<sub>3</sub>Na) dissociate and are converted to anionic dye ions. The adsorption process further proceeds due to the electrostatic attraction between these two oppositely charged ions:

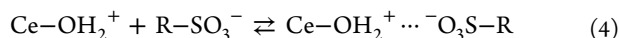
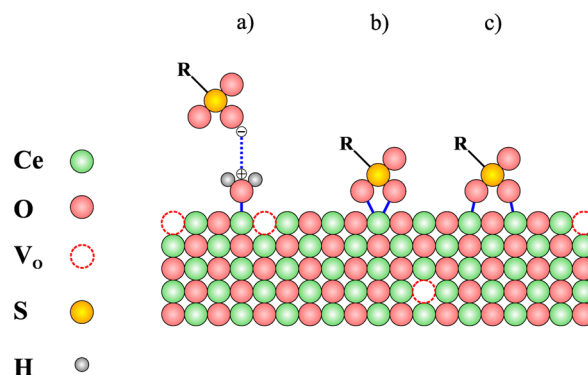


Illustration of the adsorption mechanisms between dye molecules and CeO<sub>2-δ</sub> adsorbent is shown in Figure 7.

As we stated earlier, the adsorption rate at the beginning of the process (presented in Figure 3a) is higher for RO16 than for MO and MB9. The difference in removal efficiency between three dyes can be explained by the fact that the pH value of the RO16 solution is close to the pH value where ceria net positive charge surface has maximum, whereas the pH values of MO and MB9 dye solutions are close to the pH<sub>ZPC</sub> value of CeO<sub>2-δ</sub>. Therefore, the electrostatic interaction between RO16 dye molecules and CeO<sub>2-δ</sub> at the beginning will be stronger than that for MB9 and MO. It is important to emphasize that



**Figure 7.** Schematic representation of RO16, MO, and MB9 adsorption on CeO<sub>2-δ</sub> surface. (a) Electrostatic interaction between protonated ceria surface and sulfonate group in the dye molecule; (b, c) bidentate type structures between sulfonate group and Ce<sup>4+</sup> cations.

sulfonic groups, which dissociate in aqueous solution and convert to R-SO<sub>3</sub><sup>-</sup> anions, are negatively charged even at higher acidic solutions, because their pK<sub>a</sub> values are lower than zero.<sup>44</sup> Finally, the interaction between OH groups on the surface of CeO<sub>2-δ</sub> and NH groups of the RO16 is also a possible mechanism for RO16 dye adsorption<sup>19</sup> and can explain the higher adsorption rate in the case of RO16 at the beginning of the process.

The study of the adsorption equilibrium isotherm is helpful in determining the maximum adsorption capacity of adsorbent for given adsorbate. These isotherms relate the dye uptake per unit mass of adsorbent,  $q_e$ , to the equilibrium liquid phase concentration  $C_e$ . In Figure 8 are presented the adsorption isotherms for RO16 (a), MO (b), and MB9 (c) dye solutions, measured at room temperature. Adsorption isotherms were analyzed according to Langmuir and Freundlich models in order to determine the best-fit model. Langmuir's model predicts the monolayer coverage of the adsorbate, assuming that all adsorption sites are identical and energetically equivalent, whereas the Freundlich's model assumes the adsorption on heterogeneous surface composed of nonidentical adsorption sites with different energy of adsorption. The isotherm equations and isotherm parameters for both models are listed in Supporting Information Table S3.

The adsorption isotherms of RO16 and MO from Figure 8a,b can be fitted by both the Langmuir and Freundlich equations. Both models give reasonable good fit in the case of MO and RO16, although the values of correlation coefficients (Supporting Information Table S3) are slightly higher for the Langmuir isotherm. The sorption data of MB9 are much better represented by the Freundlich model (Figure 8c and Supporting Information Table S3) which expresses adsorption in a multilayer manner on an energetically heterogeneous surface.

The parameter  $1/n$  from the Freundlich equation characterizes the heterogeneity of the site energies and the adsorption intensity, that is, the degree of nonlinearity of adsorption isotherm. In their work, Tseng and Wu<sup>45</sup> have defined a favorable level for the adsorption isotherm curves and gave a classification for the values of parameter  $1/n$ . Despite the fact that the Langmuir model seems more suitable to describe the sorption of MO and RO16 onto ceria, according to Tseng's classification, the parameter  $1/n$  (listed in Supporting Information Table S3) lies in the range of strongly favorable (for RO16 and MO) and favorable (for MB9) adsorption.

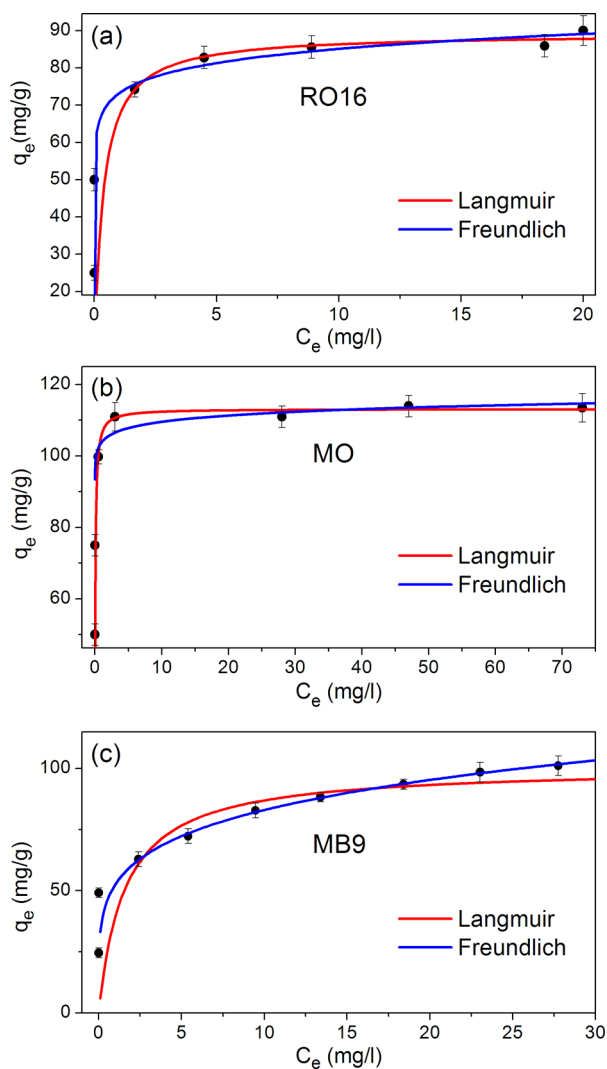


**Figure 8.** Adsorption isotherms of (a) RO16, (b) MO, and (c) MB9 dye solutions on  $\text{CeO}_{2-\delta}$  at room temperature. Initial dye concentration = 50–230  $\text{mg L}^{-1}$ ; mass of adsorbent = 50 mg; solution volume = 25 mL.

Therefore, keeping in mind that oxygen-deficient surface of nanosized ceria is more heterogeneous than homogeneous, it is reasonable to conclude that adsorption of MB9, MO, and RO16 on  $\text{CeO}_{2-\delta}$  nanopowders reflects the presence of more than one kind of adsorbent–adsorbate surface interaction. The maximal adsorption capacity values of  $\text{CeO}_{2-\delta}$  nanopowder from isotherm data were found to be 113, 101, and 91  $\text{mg g}^{-1}$  in the case of MO, MB9, and RO16 respectively.

To get further insight into the mechanism of adsorption, pseudo-first- and pseudo-second-order models were used to simulate the adsorption data for various contact times from Figure 3b. The pseudo-first-order model didn't give a good fit of the experimental data and will be omitted in further discussion. Kinetic data were further analyzed with the pseudo-second-order kinetic model shown in Figure 9. The linear form of the pseudo-second-order model is expressed as follows:

$$\frac{t}{q_t} = \frac{1}{k_2 q_e^2} + \frac{t}{q_e} \quad (4)$$

where  $q_e$  and  $q_t$  refer to the amount of adsorbed dye at equilibrium and at time  $t$ , respectively, and  $k_2$  is the equilibrium

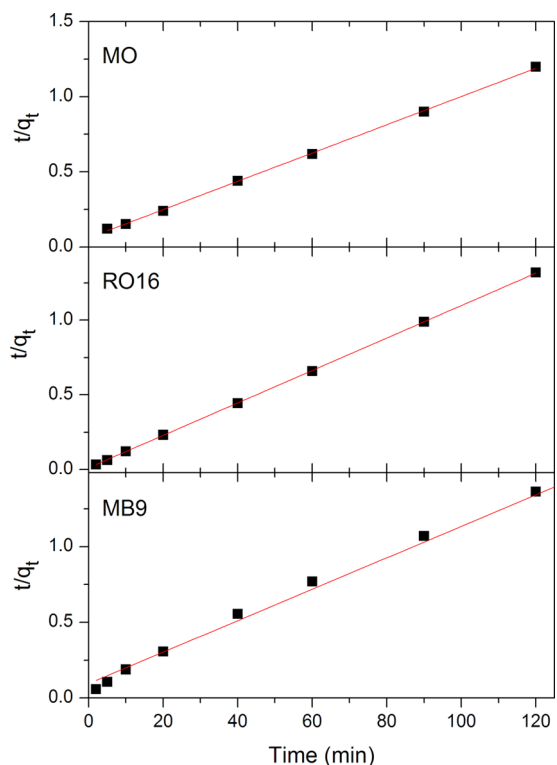


**Figure 9.** Pseudo-second-order kinetics of MO, RO16, and MB9 onto  $\text{CeO}_{2-\delta}$  nanopowder. Initial dye concentration = 200  $\text{mg L}^{-1}$ ; mass of adsorbent = 50 mg; solution volume = 25 mL.

rate constant of the pseudo-second-order kinetic model. The linear plots of  $t/q_t$  vs  $t$  (Figure 9) show that the experimental data agree well with the pseudo-second-order kinetic model for all three dyes. The values of  $q_e$  and  $k_2$  were calculated from the slope and intercept of eq 4, and their values are given in Table 1, together with experimental  $q_e$  values and correlation

**Table 1. Pseudo-Second-Order Kinetic Model Parameters Together with Experimental  $q_e$  Values for Adsorption of Each Dye**

	$q_{e,\text{cal}}$ ( $\text{mg g}^{-1}$ )	$q_{e,\text{exp}}$ ( $\text{mg g}^{-1}$ )	$k_2$ ( $\text{g mg}^{-1} \text{min}^{-1}$ )	$R^2$
MO	106.3	100	$1.44 \times 10^{-3}$	0.9994
RO16	100	91	$9.09 \times 10^{-3}$	0.9999
MB9	96.3	93.6	$1.13 \times 10^{-3}$	0.9977

coefficients. Calculated  $q_e$  values, tabulated in Table 1, are in quite good agreement with experimental ones and the correlation coefficients have large values ( $R^2 > 0.99$ ). It can be concluded that the adsorption of MO, RO16, and MB9 on  $\text{CeO}_{2-\delta}$  nanopowder follows the pseudo-second-order kinetic model which relies on the assumption that chemisorption and effective electrostatic interactions play a major role in the adsorption process.<sup>46,47</sup> Comparing the adsorption capacities of  $\text{CeO}_{2-\delta}$  nanopowder with other adsorbents mentioned in the Introduction, we can conclude that  $\text{CeO}_{2-\delta}$  nanopowder, produced by cost-effective SPRT method, shows efficient adsorption properties and is a promising candidate for environmentally friendly adsorbents in water treatment.

## CONCLUSIONS

The  $\text{CeO}_{2-\delta}$  nanopowder, synthesized by a facile and cost-effective SPRT method, appeared to be a very effective sorbent

for the MO, RO16, and MB9 azo dyes. The adsorption process was monitored at fixed initial pH value and varying dye concentration and contact time. Infrared and Raman spectroscopy measurements confirmed that the adsorption of azo dyes on the  $\text{CeO}_{2-\delta}$  surface took place. The experimental adsorption data for the MO and RO16 were slightly better fitted with the Langmuir isotherm, whereas the Freundlich isotherm was a better fit for MB9 over the whole concentration range. According to the values of the Freundlich constant ( $1/n$ ), the adsorption of MB9, MO, and RO16 lies in a favorable and strongly favorable zone. The highest adsorption capacity of  $\text{CeO}_{2-\delta}$  was obtained for MO ( $113 \text{ mg g}^{-1}$ ) and then for MB9 ( $101 \text{ mg g}^{-1}$ ) and RO16 ( $91 \text{ mg g}^{-1}$ ). The formation of a bidentate type bridge between sulfonate group and  $\text{Ce}^{4+}$  cations and the protonation of ceria surface hydroxyls can be responsible for effective adsorption process. Adsorption of MO, RO16, and MB9 dyes follows the pseudo-second-order equation with good correlation. These results imply that, besides strong electrostatic sorption, chemisorption mechanism may play an important role for the dye adsorption. Based on our results, ceria nanopowder prepared by the SPRT method represents an effective dye adsorbent and can be a promising substitute in wastewater treatment.

## ■ ASSOCIATED CONTENT

### ● Supporting Information

Figures showing absorption spectra of RO16 ( $200 \text{ mg L}^{-1}$ ) and photo image of RO16 solutions in the presence of  $\text{CeO}_{2-\delta}$  nanopowders, and zeta potential of  $\text{CeO}_{2-\delta}$  nanoparticles. Tables showing dye structures and their wavelengths of maximal absorption, values of the Raman shifts extracted from the experimental Raman spectra of  $\text{CeO}_{2-\delta}$  nanopowder after adsorption of MO, RO16, and MB9, and isotherm equations and parameters for azo dyes at room temperature. This material is available free of charge via the Internet at <http://pubs.acs.org>.

## ■ AUTHOR INFORMATION

### Corresponding Author

\*E-mail: zordoh@ipb.ac.rs.

### Notes

The authors declare no competing financial interest.

## ■ ACKNOWLEDGMENTS

We thank Bojan R. Stojadinović for the AFM image and Bojan Čalija for the zeta potential measurements. This work was financially supported by the Serbian Ministry of Education, Science and Technological Development under Projects ON171032 and III45018 and bilateral Project Serbia-Italy No. RS13MO11.

## ■ REFERENCES

- (1) Lee, J. W.; Choi, S. P.; Thiruvenkatachari, R.; Shim, W. G.; Moon, H. Evaluation of the performance of adsorption and coagulation processes for the maximum removal of reactive dyes. *Dyes Pigm.* **2006**, *69*, 196–203.
- (2) Gomez, V.; Larrechi, M. S.; Callao, M. P. Kinetic and adsorption study of acid dye removal using activated carbon. *Chemosphere* **2007**, *69*, 1151–1158.
- (3) Silva, J. P.; Sousa, S.; Rodrigues, J.; Antunes, H.; Porter, J. J.; Goncalves, I.; Ferreira-Dias, S. Adsorption of acid orange 7 dye in aqueous solutions by spent brewery grains. *Sep. Purif. Technol.* **2004**, *40*, 309–315.

- (4) Ji, P. F.; Zhang, J. L.; Chen, F.; Anpo, M. Study of adsorption and degradation of acid orange 7 on the surface of  $\text{CeO}_2$  under visible light irradiation. *Appl. Catal., B* **2009**, *85*, 148–154.

- (5) Venkatesha, T. G.; Viswanatha, R.; Nayaka, Y. A.; Chethana, B. K. Kinetics and thermodynamics of reactive and vat dyes adsorption on  $\text{MgO}$  nanoparticles. *Chem. Eng. J.* **2012**, *198*, 1–10.

- (6) Sahasrabudhe, M.; Pathade, G. Biodegradation of azo dye C.I. Reactive Orange 16 by an actinobacterium *Georgenia* sp. CC-NMPT-T3. *Int. J. Adv. Res.* **2013**, *1*, 91–99.

- (7) Mohan, D.; Pittman, C. U., Jr. Activated carbons and low cost adsorbents for remediation of tri- and hexavalent chromium from water. *J. Hazard. Mater.* **2006**, *137*, 762–811.

- (8) Pollard, S. J. T.; Fowler, G. D.; Sollars, C. J.; Perry, R. Low-cost adsorbents for waste and wastewater treatment: a review. *Sci. Total Environ.* **1992**, *116*, 31–52.

- (9) Amin, N. K. Removal of direct blue-106 dye from aqueous solution using new activated carbons developed from pomegranate peel: Adsorption equilibrium and kinetics. *J. Hazard. Mater.* **2009**, *165*, 52–62.

- (10) Sharma, Y. C.; Uma; Upadhyay, S. N. Removal of a cationic dye from wastewaters by adsorption on activated carbon developed from coconut coir. *Energy Fuels* **2009**, *23*, 2983–2988.

- (11) Aygün, A.; Yenisoay-Karakaş, S.; Duman, I. Production of granular activated carbon from fruit stones and nutshells and evaluation of their physical, chemical and adsorption properties. *Microporous Mesoporous Mater.* **2003**, *66*, 189–195.

- (12) Kannan, N.; Sundaram, M. M. Kinetics and mechanism of removal of methylene blue by adsorption on various carbons—a comparative study. *Dyes Pigm.* **2001**, *51*, 25–40.

- (13) Annadurai, G.; Juang, R. S.; Lee, D. J. Use of cellulose-based wastes for adsorption of dyes from aqueous solutions. *J. Hazard. Mater.* **2002**, *92*, 263–274.

- (14) Haddadian, Z.; Shavandi, M. A.; Abidin, Z. Z.; Fakhru'l-Razi, A.; Ismail, M. H. S. Removal methyl orange from aqueous solutions using dragon fruit (*Hylocereusundatus*) foliage. *Chem. Sci. Trans.* **2013**, *2*, 900–910.

- (15) Cheung, W. H.; Szeto, Y. S.; McKay, G. Enhancing the adsorption capacities of acid dyes by chitosan nano particles. *Bioresour. Technol.* **2009**, *100*, 1143–1148.

- (16) Wu, C. H. Adsorption of reactive dye onto carbon nanotubes: Equilibrium, kinetics and thermodynamics. *J. Hazard. Mater.* **2007**, *144*, 93–100.

- (17) Zhong, L. S.; Hu, J. S.; Cao, A. M.; Liu, Q.; Song, W. G.; Wan, L. J. 3D flowerlike ceria micro/nanocomposite structure and its application for water treatment and CO removal. *Chem. Mater.* **2007**, *19*, 1648–1655.

- (18) Ouyang, X. W.; Li, W.; Xie, S. L.; Zhai, T.; Yu, M. H.; Gan, J. Y.; Lu, X. H. Hierarchical  $\text{CeO}_2$  nanospheres as highly-efficient adsorbents for dye removal. *New J. Chem.* **2013**, *37*, S85–S88.

- (19) Zhai, T.; Xie, S. L.; Lu, X. H.; Xiang, L.; Yu, M. H.; Li, W.; Liang, C. L.; Mo, C. H.; Zeng, F.; Luan, T. G.; Tong, Y. X. Porous  $\text{Pr}(\text{OH})_3$  nanostructures as high-efficiency adsorbents for dye removal. *Langmuir* **2012**, *28*, 11078–11085.

- (20) Won, S. W.; Yun, H. J.; Yun, Y.-S. Effect of pH on the binding mechanisms in biosorption of Reactive Orange 16 by *Corynebacterium glutamicum*. *J. Colloid Interface Sci.* **2009**, *331*, 83–89.

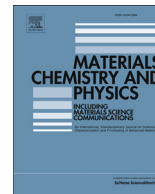
- (21) Won, S. W.; Choi, S. B.; Yun, Y.-S. Performance and mechanism in binding of Reactive Orange 16 to various types of sludge. *Biochem. Eng. J.* **2006**, *28*, 208–214.

- (22) Janaki, V.; Vijayaraghavan, K.; Ramasamy, A. K.; Lee, K. J.; Oh, B. T.; Kamala-Kannan, S. Competitive adsorption of Reactive Orange 16 and Reactive Brilliant Blue R on polyaniline/bacterial extracellular polysaccharides composite-A novel eco-friendly polymer. *J. Hazard. Mater.* **2012**, *241*, 110–117.

- (23) Suteu, D.; Zaharia, C.; Malutan, T. Removal of orange 16 reactive dye from aqueous solutions by waste sunflower seed shells. *J. Serb. Chem. Soc.* **2011**, *76*, 17.

- (24) Zhao, D.; Zhang, W.; Chen, C.; Wang, X. Adsorption of Methyl Orange dye onto multiwalled carbon nanotubes. *Procedia Environ. Sci.* **2013**, *18*, 890–895.
- (25) Saha, T. K.; Bhoomik, N. C.; Karmaker, S.; Ahmed, M. G.; Ichikawa, H.; Fukumori, Y. Adsorption of Methyl Orange onto Chitosan from Aqueous Solution. *J. Water Resour. Prot.* **2010**, *2*, 8.
- (26) Ai, L.; Zhang, C.; Meng, L. Adsorption of Methyl Orange from Aqueous Solution on Hydrothermal Synthesized Mg–Al Layered Double Hydroxide. *J. Chem. Eng. Data* **2011**, *56*, 4217–4225.
- (27) Yu, X.; Li, F.; Ye, X.; Xin, X.; Xue, Z. Synthesis of cerium(IV) oxide ultrafine particles by solid-state reactions. *J. Am. Ceram. Soc.* **2000**, *83*, 964–966.
- (28) Boskovic, S.; Djurovic, D.; Dohcevic-Mitrovic, Z.; Popovic, Z.; Zinkevich, M.; Aldinger, F. Self-propagating room temperature synthesis of nanopowders for solid oxide fuel cells (SOFC). *J. Power Sources* **2005**, *145*, 237–242.
- (29) Zhou, X.-D.; Huebner, W. Size-induced lattice relaxation in CeO<sub>2</sub> nanoparticles. *Appl. Phys. Lett.* **2001**, *79*, 3512–3514.
- (30) Lowell, S. *Characterization of Porous Solids and Powders: Surface Area, Pore Size and Density*; Kluwer Academic Publishers: Dordrecht, The Netherlands, 2004.
- (31) Jia, T.-J.; Song, G.; Li, P.-W.; He, T.-C.; Mo, Y.-J.; Cui, Y.-T. Vibrational modes study of methyl orange using SERS-measurement and the DFT method. *Mod. Phys. Lett. B* **2008**, *22*, 2869–2879.
- (32) Sathiyabama, J.; Rajendran, S.; Selvi, J. A.; Amalraj, A. J. Methyl orange as corrosion inhibitor for carbon steel in well water. *Indian J. Chem. Technol.* **2008**, *15*, 462–466.
- (33) Liu, Y.; Sun, D. Z. Development of Fe<sub>2</sub>O<sub>3</sub>-CeO<sub>2</sub>-TiO<sub>2</sub>/gamma-Al<sub>2</sub>O<sub>3</sub> as catalyst for catalytic wet air oxidation of methyl orange azo dye under room condition. *Appl. Catal., B* **2007**, *72*, 205–211.
- (34) Hua, Q.; Shi, F. C.; Chen, K.; Chang, S. J.; Ma, Y. S.; Jiang, Z. Q.; Pan, G. Q.; Huang, W. X. Cu<sub>2</sub>O-Au nanocomposites with novel structures and remarkable chemisorption capacity and photocatalytic activity. *Nano Res.* **2011**, *4*, 948–962.
- (35) Telke, A. A.; Kalyani, D. C.; Dawkar, V. V.; Govindwar, S. P. Influence of organic and inorganic compounds on oxidoreductive decolorization of sulfonated azo dye CI Reactive Orange 16. *J. Hazard. Mater.* **2009**, *172*, 298–309.
- (36) Galindo, C.; Jacques, P.; Kalt, A. Photodegradation of the aminoazobenzene acid orange 52 by three advanced oxidation processes: UV/H<sub>2</sub>O<sub>2</sub> UV/TiO<sub>2</sub> and VIS/TiO<sub>2</sub> - Comparative mechanistic and kinetic investigations. *J. Photochem. Photobiol., A* **2000**, *130*, 35–47.
- (37) Yue, L.; Zhang, X.-M. Structural characterization and photocatalytic behaviors of doped CeO<sub>2</sub> nanoparticles. *J. Alloys Compd.* **2009**, *475*, 702–705.
- (38) Danish, M.; Hashim, R.; Ibrahim, M. N. M.; Sulaiman, O. Characterization of physically activated acacia mangium wood-based carbon for the removal of methyl orange dye. *BioResources* **2013**, *8*, 16.
- (39) Dohčević-Mitrović, Z. D.; Šćepanović, M. J.; Grujić-Brojčin, M. U.; Popović, Z. V.; Bošković, S. B.; Matović, B. M.; Zinkevich, M. V.; Aldinger, F. The size and strain effects on the Raman spectra of Ce<sub>1-x</sub>Nd<sub>x</sub>O<sub>2-d</sub> (0 ≤ x ≤ 0.25) nanopowders. *Solid State Commun.* **2006**, *137*, 387–390.
- (40) Deacon, G. B.; Phillips, R. J. Relationships between the carbon-oxygen stretching frequencies of carboxylate complexes and the type of carboxylate coordination. *Coord. Chem. Rev.* **1980**, *33*, 227–250.
- (41) Bauer, C.; Jacques, P.; Kalt, A. Investigation of the interaction between a sulfonated azo dye (AO7) and a TiO<sub>2</sub> surface. *Chem. Phys. Lett.* **1999**, *307*, 397–406.
- (42) Yang, Z.; Wang, Q.; Wei, S.; Ma, D.; Sun, Q. The effect of environment on the reaction of water on the ceria(111) surface: A DFT+U study. *J. Phys. Chem. C* **2010**, *114*, 14891–14899.
- (43) Kundakovic, L.; Mullins, D. R.; Overbury, S. H. Adsorption and reaction of H<sub>2</sub>O and CO on oxidized and reduced Rh/CeO<sub>x</sub>(111) surfaces. *Surf. Sci.* **2000**, *457*, 51–62.
- (44) Lima, E. C.; Royer, B.; Vaghetti, J. C. P.; Simon, N. M.; da Cunha, B. M.; Pavan, F. A.; Benvenuti, E. V.; Cataluña-Veses, R.; Airoldi, C. Application of Brazilian pine-fruit shell as a biosorbent to removal of reactive red 194 textile dye from aqueous solution: Kinetics and equilibrium study. *J. Hazard. Mater.* **2008**, *155*, 536–550.
- (45) Tseng, R.-L.; Wu, F.-C. Inferring the favorable adsorption level and the concurrent multi-stage process with the Freundlich constant. *J. Hazard. Mater.* **2008**, *155*, 277–287.
- (46) Zhu, Y.-P.; Liu, Y.-L.; Ren, T.-Z.; Yuan, Z.-Y. Hollow manganese phosphonate microspheres with hierarchical porosity for efficient adsorption and separation. *Nanoscale* **2014**, *6*, 6627–6636.
- (47) Yeddou-Mezenner, N. Kinetics and mechanism of dye biosorption onto an untreated antibiotic waste. *Desalination* **2010**, *262*, 251–259.





# Photocatalytic degradation of alprazolam in water suspension of brookite type TiO<sub>2</sub> nanopowders prepared using hydrothermal route

N. Tomić<sup>a</sup>, M. Grujić-Brojčin<sup>a,\*</sup>, N. Finčur<sup>b</sup>, B. Abramović<sup>b</sup>, B. Simović<sup>c</sup>, J. Krstić<sup>d</sup>, B. Matović<sup>e</sup>, M. Šćepanović<sup>a</sup>

<sup>a</sup> Center for Solid State Physics and New Materials, Institute of Physics, University of Belgrade, Pregrevica 118, 11080 Belgrade, Serbia

<sup>b</sup> Department of Chemistry, Biochemistry and Environmental Protection, Faculty of Sciences, University of Novi Sad, Trg D. Obradovića 3, 21000 Novi Sad, Serbia

<sup>c</sup> Institute for Multidisciplinary Research, University of Belgrade, Kneza Višeslava 1, 11030 Belgrade, Serbia

<sup>d</sup> Institute of Chemistry, Technology and Metallurgy, Department of Catalysis and Chemical Engineering, University of Belgrade, Njegoševa 12, 11000 Belgrade, Serbia

<sup>e</sup> Institute of Nuclear Sciences "Vinča", University of Belgrade, 11001 Belgrade, Serbia

## HIGHLIGHTS

- Brookite-type TiO<sub>2</sub> powders synthesized by combined sol–gel–hydrothermal method.
- Powders investigated by XRD, SEM, EDS, BET, SE and Raman spectroscopy.
- Photocatalytic degradation of alprazolam under UV radiation.
- Photocatalytic activity attributed to high content of brookite phase.
- High photocatalytic efficiency of pure brookite sample, comparable to Degussa P25.

## ARTICLE INFO

### Article history:

Received 11 February 2015

Received in revised form

28 July 2015

Accepted 2 August 2015

Available online 15 August 2015

### Keywords:

Oxides

Nanostructures

Sol–gel growth

Raman spectroscopy and scattering

Optical properties

## ABSTRACT

Two series of nanocrystalline brookite-type powders have been synthesized by using combined sol–gel–hydrothermal method with titanium tetrachloride (TiCl<sub>4</sub>) as a precursor and hydrothermal temperature and reaction time varied in the range of 120–200 °C and 12–48 h, respectively. The effects of chosen synthesis parameters on structural, morphological and optical properties of synthesized powders have been investigated by the XRPD, SEM, EDS and BET measurements, as well Raman spectroscopy and spectroscopic ellipsometry. The XRPD results have shown that pure brookite phase, with mean crystallite size of ~33 nm, has been obtained only in the sample synthesized at 200 °C, after 24 h of hydrothermal process. In all other samples anatase phase also appears, whereas rutile and sodium titanate phases have been noticed in the samples synthesized at lower temperatures. The presence of different titania phases has also been confirmed and analyzed by Raman scattering measurements. The SEM measurements have shown spindle-like particles in brookite-rich samples synthesized at 200 °C, whereas BET measurements have detected mesoporous structure in these samples. The properties of synthesized powders have been correlated to their photocatalytic efficiency, tested in degradation of alprazolam, one of the 5th generation benzodiazepines. The sample consisted of pure brookite has shown the highest efficiency in the photodegradation of alprazolam, practically equal to the activity of Degussa P25.

© 2015 Elsevier B.V. All rights reserved.

## 1. Introduction

Titanium dioxide (titania, TiO<sub>2</sub>) is known as a polymorphic

material with three naturally occurring crystalline modifications: anatase, rutile and brookite. These structures are composed of TiO<sub>6</sub> octahedra, with edge and corner sharing organized in a different way, which is also characteristic of various titanate materials [1–4]. Brookite is the rarest of the natural TiO<sub>2</sub> polymorphs. As opposite to anatase and rutile, common titania polymorphs easily synthesized by a variety of techniques from different titanium compounds, the

\* Corresponding author.

E-mail address: [myramyra@ipb.ac.rs](mailto:myramyra@ipb.ac.rs) (M. Grujić-Brojčin).

brookite occasionally appears as a by-product obtained together with either anatase or rutile or both of these phases. Consequently, the brookite has been much less characterized phase in comparison to anatase and rutile [2,5]. The investigation of properties and potential applications has been limited due to difficulties in synthesis of pure brookite phase [2,6–11], related mainly to narrow range of synthesis conditions, which allow brookite phase to be produced [5,12]. However, the interest in brookite has been increased in recent years and pure brookite has been observed as an interesting candidate in photocatalytic applications [5,13–15].

Titania may be generally obtained by thermolysis, hydrothermal synthesis and sol–gel process [10]. Well-crystallized titania nanoparticles have been produced by using hydrothermal method [6], which has been proven as necessary in synthesizing brookite as major phase [10]. Since this treatment with titanium tetrachloride as a precursor and the addition of NaOH into reaction solution can lead to all three polymorphs of titania, the control of synthesis parameters, such as hydrothermal temperature [16] and reaction time [14] is of a great importance. Also, under these hydrothermal conditions, certain solution pH (high basicity) and particular amounts of Na cations are necessary to produce pure brookite phase [2,4,17] (and references therein). Therefore brookite type nanopowders, investigated in this study, have been prepared by combined sol–gel–hydrothermal method with  $\text{TiCl}_4$  as a precursor, in alkaline environment, with hydrothermal temperature and time varied. The effects of chosen synthesis parameters on the crystallite size, structure and phase composition of the synthesized nanopowders have been investigated by X-ray powder diffraction (XRPD), energy-dispersive X-ray spectroscopy (EDS), and Raman scattering measurements. The morphological properties of samples have been studied by scanning electron microscopy (SEM) and the Brunauer–Emmett–Teller (BET), whereas their optical properties have been investigated by the spectroscopic ellipsometry (SE) measurements.

The properties of synthesized brookite-type titania nanopowders have been correlated to their photocatalytic efficiency, tested in degradation of alprazolam and compared to the efficiency of commercial Degussa P25 under the same conditions. Alprazolam is one of the 5th generation benzodiazepines [18,19], a group of psychiatric substances acting on the central nervous system [19–21] and, similarly to the other pharmacological groups, occurring in the environment in the range of  $\text{ng/l}$ – $\mu\text{g/l}$  [22]. The presence of these compounds in the ecosystems might have a significant effect on non-target organisms [23]. In the research investigating the stability of the benzodiazepines under the influence of simulated solar irradiation, only alprazolam has shown high resistance to photodegradation [24]. Having in mind continuous input of this kind of pharmaceuticals in the environment and their persistence, there is a great interest to find new methods for their removal.

## 2. Experimental

### 2.1. Synthesis of brookite-type powders

Brookite type nanoparticles have been prepared by using combined sol–gel–hydrothermal method with  $\text{TiCl}_4$  (99.0% pure, Merck) as a precursor. An appropriate amount of  $\text{TiCl}_4$  has been dissolved in 150 ml of distilled water under vigorous stirring on the ice-bath. In order to obtain the hydrogel, the aqueous solution of NaOH has been added under careful control of the pH value of the solution (9.3). After aging in the mother liquor for 5 h, as-prepared hydrogel has been placed in a steel pressure vessel (autoclave) under a controlled temperature. After treatment, filtration and washing with distilled water until complete removal of chloride

ions, were carried out. The last step was drying at  $105.5^\circ\text{C}$  for 72 h. Two series of samples have been produced by varying the hydrothermal temperature and reaction time. In the first series the reaction time was 24 h at different temperatures: 120, 160, and  $200^\circ\text{C}$ . The second series of samples was prepared by keeping the temperature at  $200^\circ\text{C}$ , while the time of treatment was 12, 24, and 48 h. The labels assigned to samples, concerning the hydrothermal temperature and reaction time are listed in Table 1.

### 2.2. Characterization methods

The X-ray powder analysis was used to identify the crystalline phases, as well as to calculate lattice parameters of brookite phase in synthesized powders. The XRPD patterns of all samples were recorded on Rigaku (Ultima IV) X-ray Powder Diffractometer with  $\text{Cu K}\alpha_{1,2}$  radiation ( $\lambda = 1.54178 \text{ \AA}$ ). The measurements were performed in the  $2\theta$  range from  $10^\circ$  to  $80^\circ$  with the step of  $0.02^\circ$  and scanning time of 2 s/min. The calculation of the volume-weighted mean crystallite size ( $D$ ) was performed on the basis of the full width at half maximum intensity of the all reflections for brookite phase by using Scherrer's formula [25].

Morphology of the synthesized nanopowders has been studied on SEM type JEOL JSM-6460LV with the operating voltage of 20 keV. The composition/quality has also been analyzed by using the same SEM instrument equipped with an EDS INCAx-sight detector and “INAX-stream” pulse processor (Oxford Instruments).

Adsorption–desorption isotherms were obtained by nitrogen adsorption at 77 K using a Sorptomatic 1990 Thermo Finnigan device. Prior to adsorption, the samples were outgassed for 1 h under vacuum at room temperature and, additionally, at  $110^\circ\text{C}$  and the same residual pressure, for 16 h. The specific surface areas ( $S_{\text{BET}}$ ) of samples is calculated from the linear part of the adsorption isotherm by applying the Brunauer–Emmett–Teller (BET) equation [26]. The total pore volumes ( $V_{\text{tot}}$ ) were obtained from the  $\text{N}_2$  adsorption, expressed in liquid form, by using the Gurvitsch rule [27]. The micropore volume ( $V_{\text{mic}}$ ) has been estimated by the Dubinin–Radushkevich method [28]. The mesopore volume ( $V_{\text{mes}}$ ), as well as mesopore size distribution have been estimated by the Barrett, Joyner and Halenda (BJH) method from the desorption branch of the isotherms [29].

The Raman scattering measurements on brookite-type powders pressed into pellets were performed using a TriVista TR557 triple spectrometer with the 900/900/1800 grooves/mm gratings combination, equipped with a nitrogen-cooled charge coupled device (CCD) detector. All spectra have been collected in backscattering micro-Raman configuration at room temperature in the air. The 488 nm line of a mixed  $\text{Ar}^+/\text{Kr}^+$  gas laser was used as an excitation source with an output power of less than 10 mW to avoid local heating due to laser irradiation.

The ellipsometric spectra of the brookite-type nanopowders have been measured by SOPRA GES-5 variable angle ellipsometer in rotating polarizer configuration. The data were collected at room temperature, in the range from 1.5 to 6.2 eV with resolution of 0.04 eV and incidence angle of  $65^\circ$ .

## 3. Photocatalytic measurements

The photocatalytic activity of the nanopowders was evaluated

**Table 1**  
The parameters of hydrothermal synthesis.

	B <sub>120/24</sub>	B <sub>160/24</sub>	B <sub>200/24</sub>	B <sub>200/12</sub>	B <sub>200/48</sub>
Treatment temperature ( $^\circ\text{C}$ )	120	160	200	200	200
Hydrothermal reaction time (h)	24	24	24	12	48

by the removal of the solution of alprazolam (8-chloro-1-methyl-6-phenyl-4H-[1,2,4]triazole[4,3- $\alpha$ ]-[1,4]-benzodiazepine, CAS No. 28981-97-7,  $C_{17}H_{13}ClN_4$ ,  $M_r = 308.765$ ). The photocatalytic study was carried out in a cell made of Pyrex glass (total volume of ca. 40 cm<sup>3</sup>), with a plain window on which the light beam was focused, equipped with a magnetic stirring bar and a water circulating jacket. Irradiation in the UV range was performed using a 125 W high-pressure mercury lamp (Philips, HPL-N, emission bands in the UV region at 304, 314, 335 and 366 nm, with maximum emission at 366 nm), together with an appropriate concave mirror. Initial alprazolam concentration was 0.03 mM and the catalyst loading was 1.0 mg/cm<sup>3</sup>. Experiments were carried out using 20 cm<sup>3</sup> of alprazolam solution. The aqueous suspension was sonicated (50 Hz) in the dark for 15 min before illumination, to uniformly disperse the photocatalyst particles and attain adsorption equilibrium. The suspension thus obtained was thermostated at  $25 \pm 0.5$  °C in a stream of O<sub>2</sub> (3.0 cm<sup>3</sup>/min), and then irradiated. During irradiation, the suspension was stirred at a constant rate under continuous O<sub>2</sub> flow. The kinetics of the alprazolam removal was monitored with liquid chromatography with diode array detection (UFLC–DAD) at 222 nm (wavelength of alprazolam maximum absorption [30]). Commercially available TiO<sub>2</sub> Degussa P25 (75% anatase and 25% rutile, with average particle size about 20 nm, according to the producer's specification), was used for comparison.

## 4. Results

### 4.1. X-ray powder diffraction

The XRPD has been used to determine the percentage of brookite phase in synthesized nanopowder samples. Corresponding diffraction patterns are presented in Fig. 1. The existence of brookite phase has been clearly evidenced from the presence of the (121) peak at  $2\theta = 30.81^\circ$  in the patterns of all samples, but brookite content significantly varies depending on the synthesis condition. Lower content of brookite (~12.6 and ~31.6%) has been registered in the samples treated at lower temperatures (B<sub>120/24</sub> and B<sub>160/24</sub>, respectively), as listed in Table 2. In the samples synthesized at 200 °C, the content of brookite is significantly increased, but it varies with the hydrothermal time. The lowest content (~65%) of brookite is estimated in the sample treated for shortest time (B<sub>200/12</sub>). In the samples treated for longer time the amount of brookite is increased: 95% in B<sub>200/48</sub> and 100% of brookite phase in the sample B<sub>200/24</sub>.

The lattice parameters of brookite phase in all synthesized samples are listed in Table 3. Their values are similar to orthorhombic bulk structure of brookite ( $a_0 = 9.184$  nm,  $b_0 = 5.447$  nm,  $c_0 = 5.145$  nm [31]). The values of mean crystallite size and strain of brookite phase have been estimated by Scherrer's method [25] only for the samples synthesized at 200 °C (Table 3). The attempt to obtain reliable size and strain data in the other samples has failed, most probably due to more disordered brookite phase produced at lower temperatures (120, 160 °C). As can be seen from the Table 3, the decrease of the average brookite crystallite size from 58 nm to ~30 nm with the increase of the hydrothermal reaction time from 12 to 48 h has been noticed, whereas maximal strain has been observed in pure brookite sample B<sub>200/24</sub>.

In addition to the brookite diffraction peaks, the peaks corresponding to anatase phase have also been noticed in all XRPD patterns, except the one of the sample B<sub>200/24</sub> (Table 2). Note that the main (101) diffraction peak of anatase at  $2\theta = 25.28^\circ$  is partially overlapped with the (120) and (111) peaks of brookite at  $2\theta = 25.34^\circ$  and  $25.69^\circ$ , respectively [5,7,32,33]. According to results given in Table 2, in the sample treated for the shortest time (B<sub>200/12</sub>) almost 35% of anatase phase is synthesized, whereas much

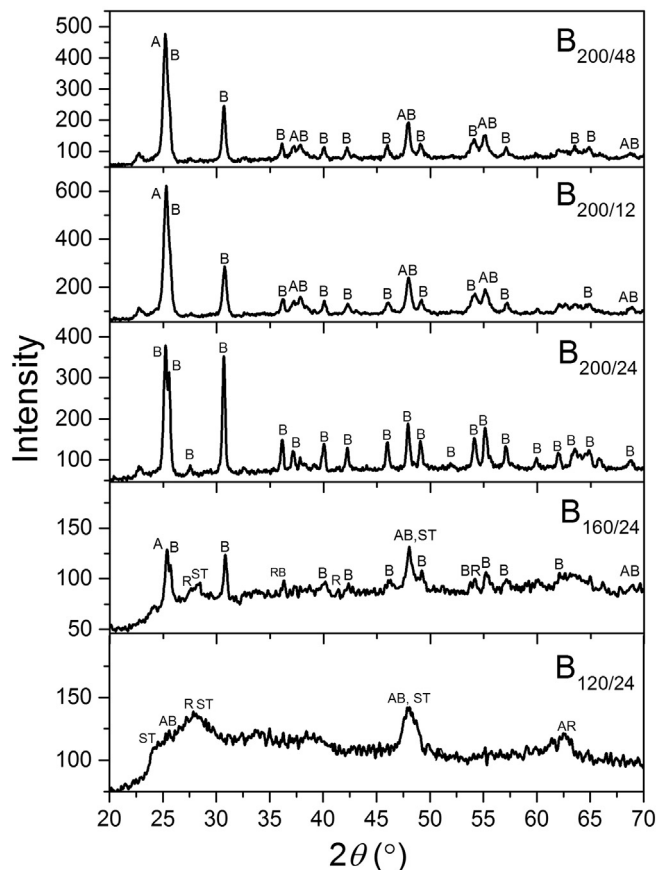


Fig. 1. XRPD patterns of titania nanopowders, with characteristic diffraction peaks of brookite, anatase, rutile and sodium titanate phase, denoted by corresponding letters.

smaller amount of anatase (~5–8%) is present in the samples treated for longer time, as can be seen from the Table 2.

Beside the brookite and anatase diffraction peaks, the XRPD patterns of the samples synthesized at lower temperatures (120 and 160 °C) exhibit low intensity and relatively broad peaks which may be related to rutile phase (~14 and ~6%, respectively) [33] and sodium trititanate in significant content (more than 50%) (Table 2), with the characteristic peaks at  $24^\circ$ ,  $28.1^\circ$  and  $48^\circ$  [16,34]. However, the XRPD patterns of these two samples have pronounced background with the humps, especially in the pattern of the sample synthesized at the lowest temperature (B<sub>120/24</sub>), suggest the presence of amorphous phase.

### 4.2. SEM

The SEM images of nanopowders are presented in Fig. 2. The differences in powder morphology, originated from different phase content, may be clearly observed. The samples synthesized at lower temperatures (B<sub>120/24</sub> and B<sub>160/24</sub>), rich in sodium titanate phase, have nanoparticles (~50 nm) of dominantly spherical shape, with

Table 2

The volume fraction (%) of brookite, anatase, rutile and sodium titanate phases estimated from XRPD patterns of synthesized powders.

Sample	B <sub>120/24</sub>	B <sub>160/24</sub>	B <sub>200/24</sub>	B <sub>200/12</sub>	B <sub>200/48</sub>
Brookite %	12.4	31.6	100	65.2	95
Anatase %	7.7	7.6	–	34.8	5.0
Rutile %	14.0	6.3	–	–	–
Na-titanate %	65.9	54.5	–	–	–

**Table 3**The lattice parameters ( $a$ ,  $b$ ,  $c$ ), average crystallite size ( $D$ ) and average strain ( $\epsilon$ ) of brookite phase in synthesized powders.

Sample		B <sub>120/24</sub>	B <sub>160/24</sub>	B <sub>200/24</sub>	B <sub>200/12</sub>	B <sub>200/48</sub>
Brookite	$a$ (nm)	9.1782	9.1347	9.1673	9.1362	9.2470
	$b$ (nm)	5.5591	5.5591	5.4382	5.4578	5.4698
	$c$ (nm)	5.1091	5.1090	5.1303	5.1398	5.1634
	$D$ (nm)	–	–	33	58	29.6
	$\epsilon$	–	–	0.0351	0.0049	0.0040

pronounced agglomeration (Fig. 2(a and b)). The spindle-like particles are predominating in the pure brookite sample (B<sub>200/24</sub>), with longer dimensions estimated up to ~300 nm, and shorter less than 100 nm (Fig. 2(c)). In the samples with mixture of anatase and brookite (B<sub>200/12</sub> and B<sub>200/48</sub>), shown in Fig. 2(d and e), most of the particles are smaller than in the pure brookite sample, with elongated structure retained.

#### 4.3. EDS

The chemical composition of synthesized nanopowders has been estimated by EDS method. The EDS spectra are collected from corresponding framed areas of SEM micrographs, shown together in Fig. 3. The oxygen weight percent in all samples is estimated in the range ~45–48 wt.% (Table 4), above the value corresponding to stoichiometric TiO<sub>2</sub> (40 wt.%). The Na content has been detected in sodium titanate rich samples, treated at lower temperatures (120 and 160 °C).

#### 4.4. Nitrogen physisorption

In order to study the influence of the hydrothermal temperature and reaction time on the pore structure and adsorption abilities of synthesized powders nitrogen sorption isotherms have been measured. The isotherms of brookite-rich samples (B<sub>200/12</sub>, B<sub>200/24</sub>, and B<sub>200/48</sub>) are presented in Fig. 4(a). The curves may be interpreted as type IV [35], typical for mesoporous materials, with an H<sub>2</sub>-type hysteresis loop, indicating the presence of pore networks. Corresponding information on specific surface areas ( $S_{BET}$ ) and the total pore ( $V_{tot}$ ), micropore ( $V_{mic}$ ) and mesopore ( $V_{mSSe50}$ ) volumes are summarized in Table 5. According to these results, the specific surface area in the pure brookite sample (B<sub>200/24</sub>) is the smallest ( $S_{BET} = 69.5 \text{ m}^2/\text{g}$ ), whereas  $S_{BET}$  is larger in the samples consisting of both anatase and brookite phase is higher (97.9 and 76.5  $\text{m}^2/\text{g}$  in B<sub>200/12</sub> and B<sub>200/48</sub>, respectively). Such reverse dependency

between the  $S_{BET}$  of brookite-rich powders and brookite content has been already noticed in the literature [36,37]. It should be also noted that in our samples synthesized at lower temperatures (B<sub>120/24</sub> and B<sub>160/24</sub>) very high values of specific surface area ( $>250 \text{ m}^2/\text{g}$ ), with significant microporous contribution, have been measured.

The BJH method was used to evaluate the mesopore size distribution in brookite-rich samples from the desorption branch of the isotherm curves. The distributions are shown in Fig. 4(b), whereas the values of the most frequent pore diameter ( $D_p$ ), corresponding to the maximum of the mesopore size distribution, are listed in Table 5. The highest value of  $D_p$  is estimated in the pure brookite sample.

#### 4.5. Raman scattering measurements

The Raman spectroscopy, as a powerful technique to distinguish titania modifications in samples consisting of mixed phases, has been used for independent structural analysis, providing data on phase purity and crystallinity. The Raman spectra of all synthesized nanopowders are shown in Fig. 5. It can be noticed that the spectra of nanopowders synthesized at 200 °C are dominated by brookite modes (denoted by “B” in the figure). Moreover, all Raman features in the spectrum of the sample B<sub>200/24</sub> can be ascribed to brookite phase, as shown in Fig. 6. These brookite modes are assigned and listed in the Table 6, together with bulk reference values [11]. Almost all of these modes are also registered in the spectra of the samples at the same temperature, but for different time (B<sub>200/12</sub> and B<sub>200/48</sub>), as shown in Table 6. The frequencies of the most intensive brookite Raman modes are slightly shifted towards higher values in comparison to the values of bulk brookite [11]. This shift is most pronounced in the spectrum of the sample B<sub>200/48</sub>.

In the Raman spectra of the samples hydrothermally treated at 200 °C (B<sub>200/12</sub> and B<sub>200/48</sub>), besides brookite modes, the most intensive anatase  $E_g$  mode  $\sim 144 \text{ cm}^{-1}$  is clearly observed (Fig. 5). The other anatase modes have also been detected in these

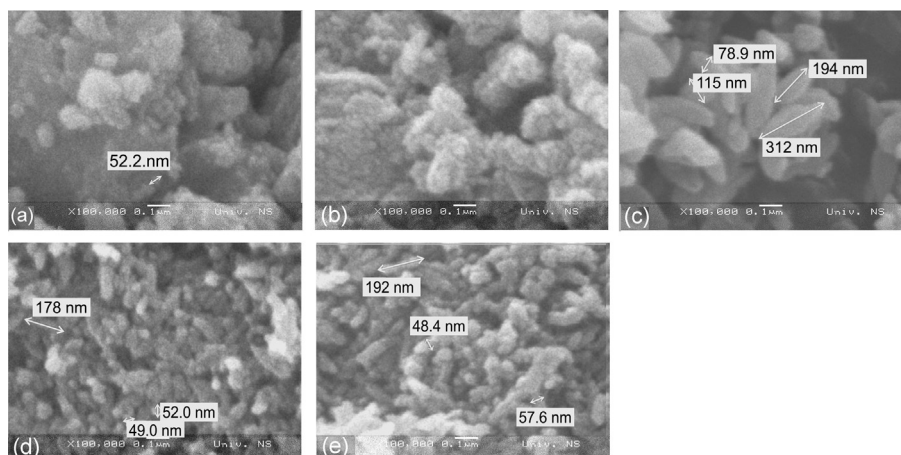


**Fig. 2.** The SEM micrographs of synthesized nanopowders: (a) B<sub>120/24</sub>, (b) B<sub>160/24</sub>, (c) B<sub>200/24</sub>, (d) B<sub>200/12</sub>, and (e) B<sub>200/48</sub>.

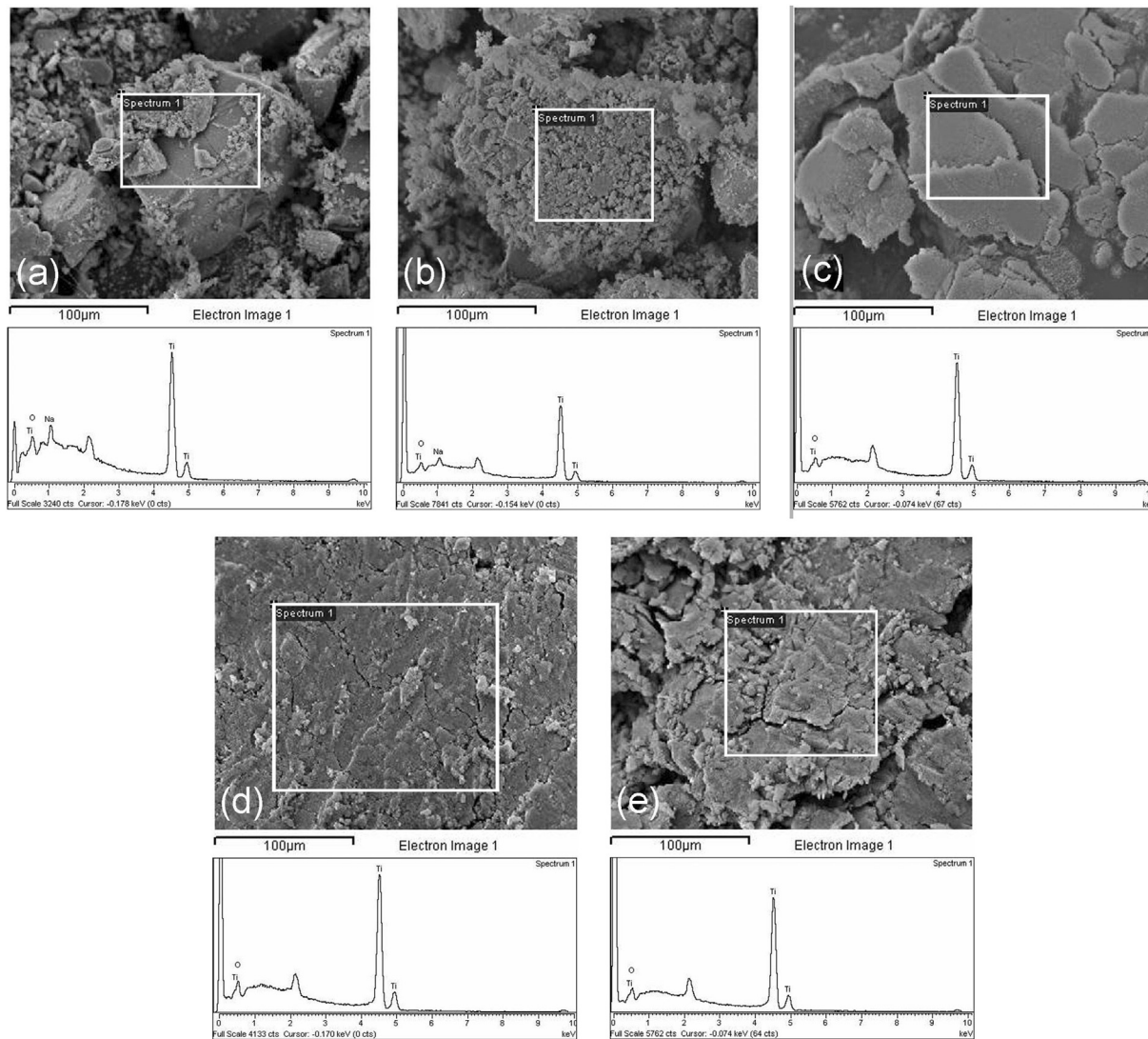


**Fig. 3.** EDS spectra of hydrothermally synthesized titania samples: (a) B<sub>120/24</sub>, (b) B<sub>160/24</sub>, (c) B<sub>200/24</sub>, (d) B<sub>200/12</sub>, and (e) B<sub>200/48</sub>, with corresponding area shown in SEM images.

spectra:  $A_{1g}$  ( $\sim 399\text{ cm}^{-1}$ ) and  $A_{1g} + B_{1g}$  ( $\sim 520\text{ cm}^{-1}$ ), with  $E_g$  mode at  $\sim 637\text{ cm}^{-1}$  partially overlapping with brookite  $A_{1g}$  mode at  $\sim 640\text{ cm}^{-1}$ .

The Raman spectra of samples treated at lower temperatures (B<sub>120/24</sub> and B<sub>160/24</sub>) are dominated by the broad features which can be ascribed to amorphized sodium titanate structure [16,38] as follows:  $\sim 123, 385, 440, 582, 665, 710, 754, 815,$  and  $911\text{ cm}^{-1}$ . These modes are more pronounced in the spectrum of the sample B<sub>120/24</sub>. Note also that in the spectra of these samples very low intensity modes  $A_{1g}$  at  $\sim 445\text{ cm}^{-1}$  and  $E_g$  at  $\sim 610\text{ cm}^{-1}$  corresponding to rutile phase have also been registered.

The Raman spectra of all synthesized samples in the region of  $80\text{--}230\text{ cm}^{-1}$ , fitted by the sum of Lorentzian functions

corresponding to the modes of anatase, brookite and sodium titanate, are shown in Fig. 7. This region, containing the most intensive Raman modes of anatase and brookite, has been used as reliable fingerprint, which may give insight into the phase composition and crystallinity of synthesized nanopowders.

The spectra of the samples synthesized at lower temperatures (B<sub>120/24</sub> and B<sub>160/24</sub>) in this region are characterized by the most intensive  $A_{1g}$  brookite mode (B) and broad features corresponding to sodium titanate modes (ST), covering anatase modes (A) and the other, less intensive brookite modes, positioned in the vicinity (marked as ST + B). Thereby, the intensity ratio of the brookite to sodium titanate Raman modes is much higher in the spectrum of the sample synthesized at higher hydrothermal temperature (B<sub>160/24</sub>).

Raman modes corresponding to brookite phase positioned at  $\sim 129, 155,$  and  $215\text{ cm}^{-1}$  have been clearly distinguished in specified region of all Raman spectra of the samples synthesized at  $200\text{ }^\circ\text{C}$  (Fig. 7). However in the spectra of the samples B<sub>200/12</sub> and B<sub>200/48</sub>, characteristic anatase mode  $E_g$  at  $\sim 144\text{ cm}^{-1}$  is the most intensive. Slightly higher integrated intensity ratio of this anatase  $E_g$  mode to the most intensive brookite  $A_{1g}$  mode is found in the spectrum of the sample treated for shorter time (B<sub>200/12</sub>).

**Table 4**  
EDS results for hydrothermally synthesized titania nanopowders.

Sample	O (wt.%)	Ti (wt.%)	Na (wt.%)	Total (wt.%)
B <sub>120/24</sub>	46.26	44.43	9.31	100.00
B <sub>160/24</sub>	45.21	48.78	6.01	100.00
B <sub>200/24</sub>	45.46	54.54	–	100.00
B <sub>200/12</sub>	48.09	51.91	–	100.00
B <sub>200/48</sub>	47.22	52.78	–	100.00

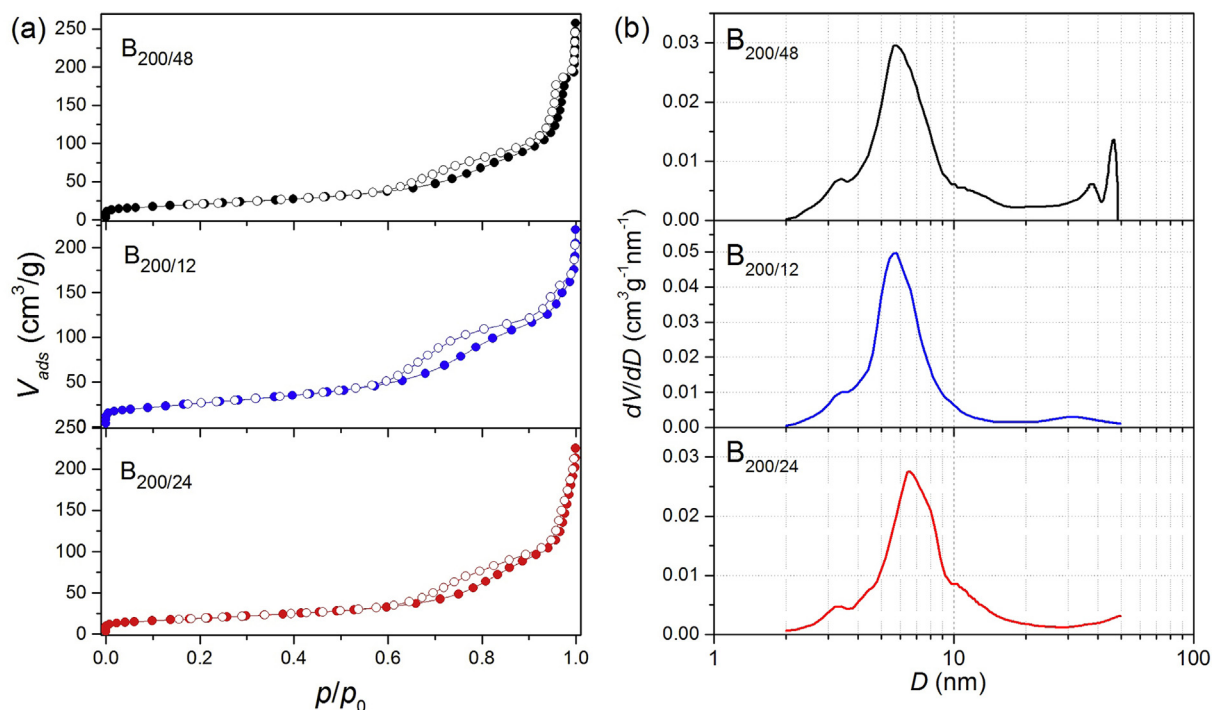


**Fig. 4.** (a) Nitrogen physisorption isotherms of brookite-rich samples ( $B_{200/12}$ ,  $B_{200/24}$ ,  $B_{200/48}$ ) at 77 K. The filled symbols represent adsorption points and empty symbols represent desorption points. (b) The mesopore size distribution calculated by BJH method.

#### 4.6. Spectroscopic ellipsometry

Electronic band structure of brookite is rarely studied in comparison to other titania polymorphs. Basically, there are experimental and theoretical studies providing different and also conflicting bandgap energies, both direct and indirect, as well as larger and smaller than bandgap of anatase phase ([3,7,13] and references therein). In general, the reason for lack of unambiguous opinion on the bandgap of brookite is anisotropy of such complex semiconductor material. Therefore the values of energy related to direct or indirect transition is surely dependent on the structural and morphological properties of brookite material, determined by different synthesis conditions.

The spectroscopic ellipsometry has been used to investigate optical and electronic properties of synthesized brookite-type nanopowders. The complex pseudo-dielectric functions of these powders have been determined from SE data by using a two-phase (ambient/substrate) model. No correction for overlayers and surface roughness has been made. The absorption coefficient for all synthesized powders has been evaluated as  $\alpha(\lambda) = 4\pi k(\lambda)/\lambda$ , where  $\lambda$  is the wavelength of incident light and the spectral dependence of the extinction coefficient  $k(\lambda)$  has been calculated from the real and the imaginary part of the pseudo-dielectric function.

**Table 5**

The porous properties of brookite-rich nanopowders and Degussa P25 obtained from BET measurement: specific surface area ( $S_{BET}$ ), total pore volume ( $V_{tot}$ ), meso- and micro-pore volume ( $V_{meso}$  and  $V_{mic}$ , respectively), and the most frequent pore diameter ( $D_p$ ).

Sample	$S_{BET}$ (m <sup>2</sup> /g)	$V_{tot}$ (cm <sup>3</sup> /g)	$V_{meso}$ (cm <sup>3</sup> /g)	$V_{mic}$ (cm <sup>3</sup> /g)	$D_p$ (nm)
$B_{200/12}$	97.9	0.244	0.247	0.032	5.78
$B_{200/24}$	69.5	0.241	0.201	0.024	6.64
$B_{200/48}$	76.5	0.286	0.280	0.026	5.91
Degussa P25	53.2	0.134	0.108	0.017	2.09

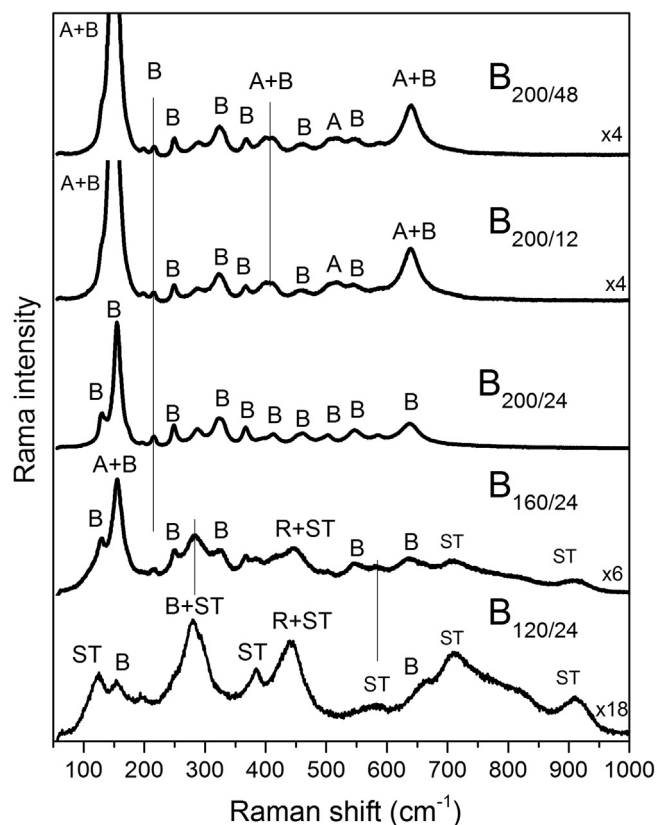


**Fig. 5.** The Raman spectra of hydrothermally synthesized powders, with the most intensive modes assigned to brookite (B), anatase (A), rutile (R), and sodium titanate (ST).

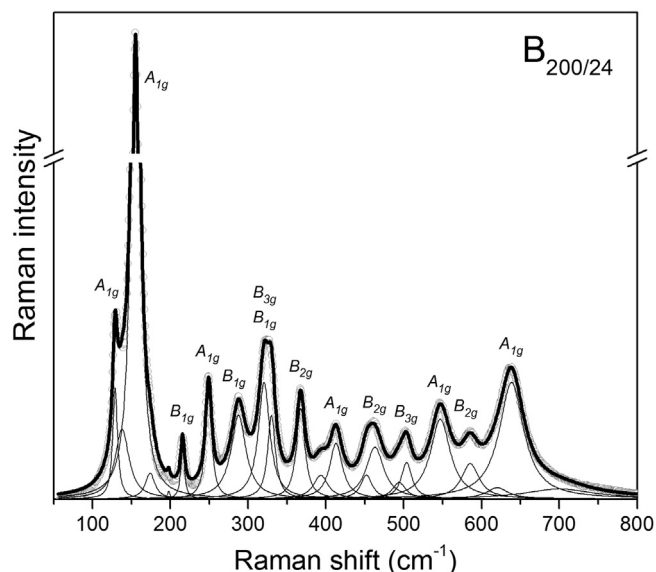


**Fig. 6.** The Raman spectrum of nanopowder  $B_{200/24}$  fitted by the sum of Lorentzians corresponding to brookite modes (only the most intensive modes are assigned).

The absorption coefficient  $\alpha$  is assumed to follow well-known dependence  $\alpha E \approx A(E-E_g)^\gamma$ , where  $E$  is the photon energy,  $A$  is a sample-dependent constant parameter, whereas  $\gamma$  is a constant equal to 1/2 and 2 for direct and indirect allowed transitions, respectively. The dependence of  $(\alpha E)^{1/2}$  plots on the photon energy for an indirect transition, as well as the  $(\alpha E)^2$  plots for a direct transition, are shown in Fig. 8(a) and (b) respectively. The energies of direct and indirect transition in pure brookite sample ( $B_{200/24}$ ) are determined by extrapolating the straight-line portions of these plots to the photon energy axis [39]. For this sample the values of  $\sim 2.5$  eV for indirect and  $\sim 3.85$  eV for direct transition energy have been obtained by this procedure. The curves presented in Fig. 8 suggest lower values of the energy both for direct and indirect transition in other samples synthesized at 200 °C ( $B_{200/12}$  and  $B_{200/48}$ ) consisted from anatase and brookite. On the contrary, in the powders synthesized at lower temperatures ( $B_{120/24}$  and  $B_{160/24}$ ), with sodium titanate as dominant phase, the energies of direct and indirect transition seem to be higher than in pure brookite sample. However, the values of transition energy for the samples other than pure brookite have not been refined by the procedure described above, having in mind that two-phase model is not fully appropriate to calculate the dielectric function of the material consisted of several phases with different bandgap energies. Therefore more elaborate analysis of the ellipsometric data, should be performed in the future research.

#### 4.7. Photocatalytic efficiency

The influence of the hydrothermal temperature and time of the synthesis process on photocatalytic activity of produced powders have been studied through the photocatalytic removal of alprazolam under UV light irradiation. The effect of the treatment temperature on the photocatalytic activity of powders synthesized during 24 h, presented in Fig. 9(a), has been studied. Photocatalytic activity of powders treated at 120 and 160 °C have shown very low photocatalytic activity, whereas the one treated at 200 °C has exhibited a significant increase in the alprazolam photodegradation efficiency. The kinetics curve of alprazolam removal using the most frequently used oxide semiconductor for photodegradation, Degussa P25 is also shown in Fig. 9(a). As can be seen from the

**Table 6**  
The brookite Raman modes of the brookite-type nanopowders samples. The assignment has been performed according to Iliev et al. [11].

Assign.	Raman modes ( $\text{cm}^{-1}$ )					Ref. [11]
	$B_{120/24}$	$B_{160/24}$	$B_{200/24}$	$B_{200/12}$	$B_{200/48}$	
$A_{1g}$	128	125	129	129	130	125 m
	155	154	155	155	156	152 vs
	195	197	198	199	200	194 w
	244	249	249	249	250	246 s
	–	–	–	–	–	324 w
	–	418	413	413	413	412 w
	–	–	494	–	–	492 w
	–	549	547	546	547	545 s
	–	635	639	638	640	640 s
	–	–	–	–	–	–
$B_{1g}$	168	–	174	170	179	169 m
	218	215	215	215	215	212 m
	289	285	288	287	290	283 s
	–	–	330	–	–	327 m
	–	–	–	–	–	381 vw
	–	–	–	–	–	–
	–	451	452	–	–	449 m
	–	–	625	–	–	622 w
	–	–	–	–	–	160 s
	–	–	–	–	–	254 vw
$B_{2g}$	–	–	–	–	–	325 m
	–	366	367	367	368	366 s
	–	–	393	399	399	391 w
	–	–	463	460	460	460 s
	–	586	585	587	583	584 m
	–	–	137	–	–	132 m
	–	–	–	–	–	212 w
	322	325	320	323	324	318 s
	–	–	–	–	–	416 w
	506	500	504	508	505	500 m

figure, photocatalytic activity of the sample  $B_{200/24}$  is practically equal to Degussa P25.

The effect of hydrothermal reaction time (12, 24 and 48 h) on photocatalytic activity of the samples synthesized at 200 °C has also been studied. The kinetics curves for the samples are presented in Fig. 9(b). Among these samples, all active in degradation of alprazolam, the sample  $B_{200/24}$  has shown the highest activity. On the basis of these kinetic curves from Fig. 9(b), the kinetics parameters (reaction rate constant and reaction rate) were also calculated by fitting a pseudo-first order kinetic model to each set of results. Linear regression coefficients were in the range from 0.9968 to 0.9989 (Table 7), confirming the adequacy of the pseudo-first order model to describe the kinetics of alprazolam degradation. According to this analysis, the lowest photocatalytic efficiency has been registered in nanopowder  $B_{200/12}$ , whereas the sample  $B_{200/24}$  has been the most effective in the degradation of alprazolam.

## 5. Discussion

The intention of this work is to analyze the influence of structure and morphology of brookite-type powders on photocatalytic efficiency in removal of alprazolam, as pharmaceutical rarely studied in terms of photocatalytic degradation. Two series of nanocrystalline brookite-type powders have been synthesized by using combined sol–gel–hydrothermal method with  $\text{TiCl}_4$  as a precursor, with the hydrothermal temperature and reaction time varied. By comparing the synthesis conditions and the properties of produced samples of these two series, optimal hydrothermal parameters for producing pure brookite phase have been determined.

The first series of samples has been obtained at different temperatures (120, 160 and 200 °C) during 24 h. The XRPD and Raman

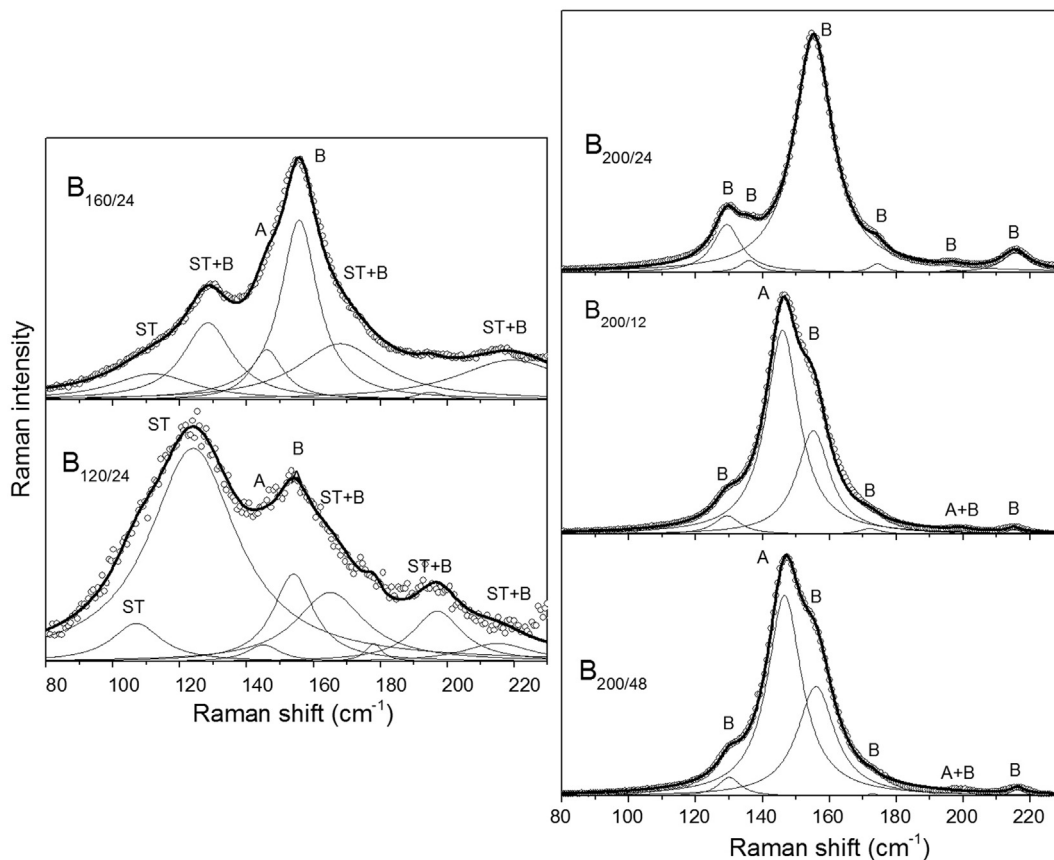


**Fig. 7.** The Raman spectra of nanopowder samples in the range from 80 to 230  $\text{cm}^{-1}$  fitted by the sum of Lorentzians corresponding to the modes of anatase, brookite and sodium titanate, denoted by A, B, and ST respectively.

scattering measurements have shown that temperatures lower than 200 °C in such hydrothermal process are insufficient to synthesize brookite-rich samples. Namely, the samples synthesized at lower temperatures ( $B_{120/24}$  and  $B_{160/24}$ ) are abundant in amorphous sodium titanate phase, whereas all titania phases (rutile, anatase, and brookite) are represented in a much smaller percentage. The SEM measurements have shown that these powders

consisted of agglomerated nanoparticles with dominantly spherical shape. Also, in these samples, synthesized at lower temperatures, a large specific surface areas, with great microporous contribution, have been measured by BET. With hydrothermal temperature increased to 200 °C, specific surface area has decreased, and mesoporous samples have been synthesized. Pure brookite sample with spindle-like particles has been obtained at the temperature of

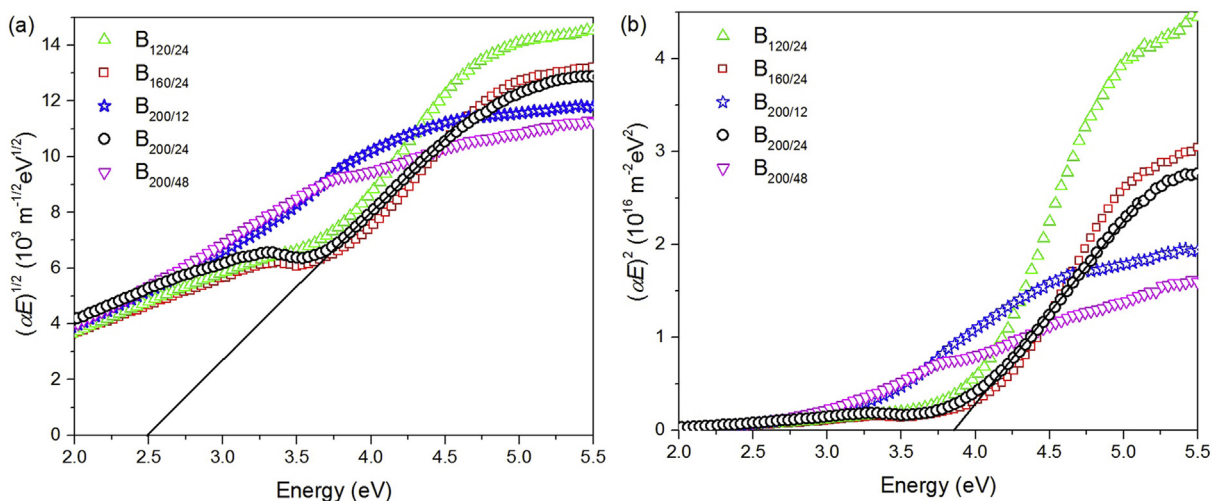


**Fig. 8.** (a) The plot of  $(\alpha E)^{1/2}$  versus  $E$  for indirect bandgap transition in synthesized powders; (b) The plot of  $(\alpha E)^2$  versus  $E$  for direct bandgap transition in the same samples with characteristic tangent lines for pure brookite sample.



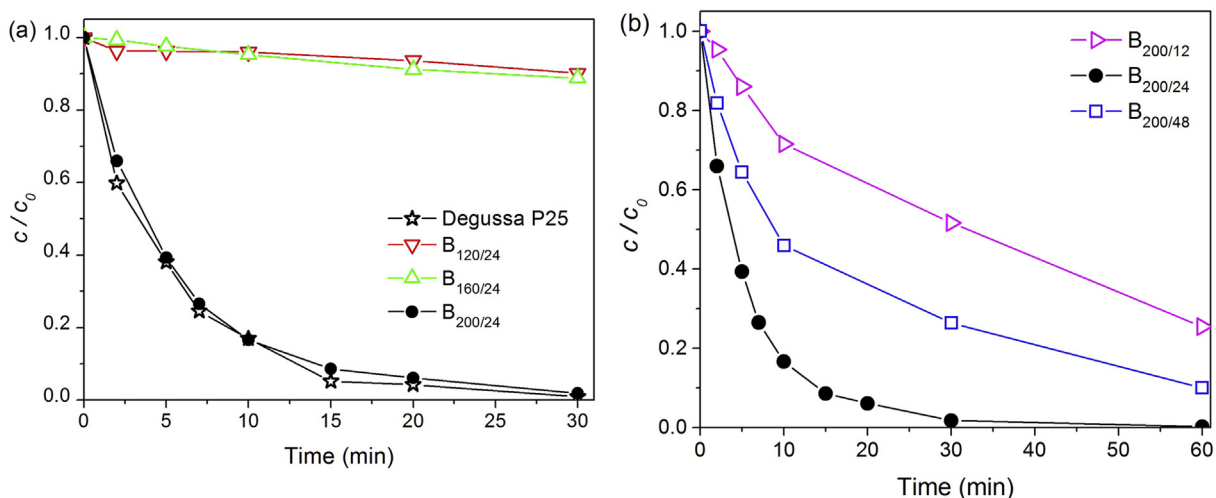


**Fig. 9.** The influence of different synthesis conditions on the photocatalytic efficiency of synthesized powders in the removal of alprazolam ( $c_0 = 0.03$  mM): (a) the samples synthesized at different temperatures (120, 160, and 200 °C) during 24 h, and (b) the samples synthesized at 200 °C during different hydrothermal reaction time (12, 24, and 48 h).

200 °C for 24 h of hydrothermal procedure, as mentioned in the previous sections.

In another series of the samples the influence of the hydrothermal time on the properties of powders synthesized at 200 °C has been studied. Beside the sample synthesized during 24 h at 200 °C, included in the series described above, two more powders with hydrothermal reaction times of 12 and 48 h have been produced. According to the XRPD analyses average crystallite size of brookite phase has decreased with the increase of hydrothermal reaction time. The results obtained by Raman scattering measurements have also pointed to higher crystallinity of brookite phase in the sample synthesized for 12 h than in the one synthesized for 48 h. Namely, similar Raman spectra obtained for the samples  $B_{200/12}$  and  $B_{200/48}$ , with different brookite content (according to XRPD), may be the consequence of lower crystallinity of brookite phase in the sample with higher brookite content ( $B_{200/48}$ ). It should be noted that these results are opposite to those presented in the study of Xie et al. [6] where, with  $Ti(SO_4)_2$  used as precursor, more crystalline, larger particles of brookite phase have been produced by increasing the hydrothermal reaction time.

In the samples  $B_{200/12}$  and  $B_{200/48}$  the anatase phase has also been revealed by the XRPD and Raman scattering measurements, in addition to the brookite phase. In both of these samples spindle-like particles recorded by the SEM are ascribed to brookite phase, whereas particles with dominant anatase phase are most likely spherical. The anatase has been synthesized not only in the sample treated for time shorter than 24 h (~35%), but also in the one treated for the 48 h (~5% of anatase phase), confirming that by described hydrothermal procedure pure brookite may be synthesized in relatively narrow range of reaction time [12]. Note also that in hydrothermal synthesis of mixed titania phase, produced with  $TiCl_3$

as precursor and NaOH added to the reaction solution, the decrease of pH value of solution, followed by the decrease of brookite content, has been registered with increase of hydrothermal time [17]. Having in mind that high basicity is required for the formation of brookite phase in this type of hydrothermal synthesis [4,17], reappearance of anatase phase after hydrothermal reaction time longer than 24 h, as in the sample  $B_{200/48}$  here, may be attributed to the decrease in the pH value of the solution due to increased reaction time. The BET measurements have shown that all brookite-rich samples were mesoporous, with the specific surface area of the samples decreasing and maximum of the mesopore size distribution slightly increasing with the increase of brookite content. The results of spectroscopic ellipsometry have pointed that the presence of anatase phase in the samples synthesized at 200 °C is decreasing the energy of direct and indirect transitions. This observation is in accordance with effective increase of the bandgap energy of the brookite in comparison to that of the anatase phase, due to cathodic shift of conduction band of brookite [36].

Regarding the photocatalytic activity, pure brookite sample  $B_{200/24}$  has shown the highest efficiency, removing more than 98% of alprazolam completely in the first 30 min of photocatalytic reaction. This sample has shown activity practically equal to commercial Degussa P25. The samples  $B_{200/12}$ , and  $B_{200/48}$ , consisted of both brookite and anatase phases, have removed ~75% and ~90% of alprazolam within 60 min of exposure. The sodium-titanate-powders synthesized at lower temperatures ( $B_{120/24}$  and  $B_{160/24}$ ) have performed very low activity.

In general, the dependence of photocatalytic activity of titania-based materials on many factors, such as crystallinity and crystallite size, phase composition, morphology and porous structure, bandgap energy, etc., is a complex question [7,37,40–42]. The photocatalytic activity of two or three phases titania mixture is often reported higher than of pure polymorphs [7,43,44], but the majority of studies have been related to anatase-based photocatalysts [7] and references therein]. Several authors have pointed out an optimum ratios between anatase and brookite corresponding to the highest photoactivity in particular degradation processes [7,44]. On the other side, the nature of brookite-based photocatalysts is still matter of discussion, as pure brookite samples of different structures have been reported as both more and less active than other titania polymorphs or mixtures of brookite with other titania phases [5,14,15].

**Table 7**

Kinetic parameters for the photocatalytic removal of alprazolam ( $c_0 = 0.03$  mM) in presence of synthesized  $TiO_2$  nanopowders.

	$k^a \times 10^2$ (min <sup>-1</sup> )	$R^b \times 10^3$ (mM/min)	$r^c$
$B_{200/12}$	3.39	1.02	0.9976
$B_{200/24}$	17.9	5.38	0.9989
$B_{200/48}$	7.68	2.30	0.9968

<sup>a</sup> Reaction rate constant determined for the first 10 min of irradiation.

<sup>b</sup> Reaction rate determined for the first 10 min of irradiation.

<sup>c</sup> Linear regression coefficient.

In photocatalytic degradation of alprazolam, presented in this work, the samples consisted of brookite-anatase mixed phase have shown increasing efficiency with decreasing of anatase in favor of brookite content. Among brookite-rich samples the pure brookite has performed the highest efficiency in degradation of alprazolam. This efficiency could not be related to the properties often pointed out as preferable in photocatalysis, such as small particle size and/or large specific surface area. Namely, neither the specific surface area of the pure brookite sample is the largest (on the contrary, it has minimal value,  $\sim 69.5 \text{ m}^2/\text{g}$ ), nor its brookite crystallites are the smallest (see Table 3). High brookite content as decisive factor for higher photocatalytic efficiency of brookite/anatase mixtures, rather than crystallite size or surface area, has been previously noticed and explained by the cathodic shift of the conduction band of brookite in comparison to anatase phase [36,37]. This shift should facilitate the interfacial electron transfer to molecular oxygen and thus accelerate the overall photocatalytic process [36,40]. Having in mind this consideration, the energy of direct and indirect transition registered in pure brookite sample, higher than in brookite/anatase mixtures, may provide better photocatalytic efficiency in degradation of alprazolam. Beside this, improved efficiency in photodegradation of relatively large molecule of alprazolam (with molecular size estimated as  $1.27 \times 1.13 \times 0.85 \text{ nm}$ ) may also be influenced by a slight increase of most frequent pore diameter with the increase of brookite content in the samples.

## 6. Conclusion

The influence of composition and morphology of brookite-type powders on their photocatalytic efficiency in removal of alprazolam under UV light irradiation has been studied. Two series of nanocrystalline brookite-type powders have been synthesized by using combined sol–gel–hydrothermal method with  $\text{TiCl}_4$  as a precursor, with the hydrothermal temperature and reaction time varied. Optimal hydrothermal parameters for producing pure brookite phase have been determined. The brookite-rich powders, synthesized at  $200^\circ\text{C}$ , have shown high photocatalytic efficiency, whereas the powders consisted dominantly of sodium-titanate, produced at lower temperatures ( $120$  and  $160^\circ\text{C}$ ), have been almost photocatalytically inactive in degradation of alprazolam. Pure brookite sample has performed the highest efficiency, removing more than 98% of alprazolam in the first 30 min of photocatalytic reaction. Improved photocatalytic efficiency in photodegradation of alprazolam has been mainly ascribed to increased amount of brookite phase in the hydrothermally synthesized  $\text{TiO}_2$  samples, rather than brookite crystallite size and specific surface area of nanopowders. Such improvement may be related to higher energy of direct and indirect transitions in pure brookite sample, as well as a slight increase of most frequent pore diameter with the increase of brookite content in brookite-rich samples.

## Acknowledgment

This work was financially supported by the Ministry of Education, Science and Technological Development (Republic of Serbia), under the Projects No. III45018, ON171032, and ON172042, as well as SASA project F–134.

## References

- [1] H. Liu, E.R. Waclawik, Z. Zheng, D. Yang, X. Ke, H. Zhu, R.L. Frost, TEM investigation and FBB model explanation to the phase relationships between titanates and titanium dioxides, *J. Phys. Chem. C* 114 (2010) 11430–11434.
- [2] J.G. Li, T. Ishigaki, Brookite – rutile phase transformation of  $\text{TiO}_2$  studied with monodispersed particles, *Acta Mater.* 52 (2004) 5143–5150.
- [3] D. Reyes-Coronado, G. Rodríguez-Gattorno, M.E. Espinosa-Pesqueira, C. Cab, R. de Coss, G. Oskam, Phase-pure  $\text{TiO}_2$  nanoparticles: anatase, brookite and rutile, *Nanotechnology* 19 (2008) 145605 (1–10).
- [4] Y. Zheng, E. Shi, S. Cui, W. Li, X. Hu, Hydrothermal preparation of nanosized brookite powders, *J. Am. Ceram. Soc.* 83 (10) (2000) 2634–2636.
- [5] A. Di Paola, M. Bellardita, L. Palmisano, Brookite, the least known  $\text{TiO}_2$  photocatalyst, *Catalysts* 3 (1) (2013) 36–73.
- [6] J. Xie, X. Lü, J. Liu, H. Shu, Brookite titania photocatalytic nanomaterials: synthesis, properties, and applications, *Pure Appl. Chem.* 81 (12) (2009) 2407–2415.
- [7] A. Di Paola, G. Cufalo, M. Addamo, M. Bellardita, R. Camprostrini, M. Ischia, R. Ceccato, L. Palmisano, Photocatalytic activity of nanocrystalline  $\text{TiO}_2$  (brookite, rutile and brookite-based) powders prepared by thermohydrolysis of  $\text{TiCl}_4$  in aqueous chloride solutions, *Colloid. Surf. A* 317 (2008) 366–376.
- [8] B.I. Lee, X. Wang, R. Bhavne, M. Hu, Synthesis of brookite  $\text{TiO}_2$  nanoparticles by ambient condition sol process, *Mater. Lett.* 60 (2006) 1179–1183.
- [9] J.H. Lee, Y.S. Yang, Synthesis of  $\text{TiO}_2$  nanoparticles with pure brookite at low temperature by hydrolysis of  $\text{TiCl}_4$  using  $\text{HNO}_3$  solution, *J. Mater. Sci.* 41 (2006) 557–559.
- [10] R.C. Bhavne, B.I. Lee, Experimental variables in the synthesis of brookite phase  $\text{TiO}_2$  nanoparticles, *Mater. Sci. Eng. A* 467 (2007) 146–149.
- [11] M.N. Iliiev, V.G. Hadjiev, A.P. Litvinchuk, Raman and infrared spectra of brookite ( $\text{TiO}_2$ ): experiment and theory, *Vib. Spectrosc.* 64 (2013) 148–152.
- [12] Y. Morishima, M. Kobayashi, V. Petrykin, S. Yin, T. Sato, M. Kakihana, K. Tomita, Hydrothermal synthesis of brookite type  $\text{TiO}_2$  photocatalysts using a water soluble Ti-complex coordinated by ethylenediaminetetraacetic acid, *J. Ceram. Soc. Jpn.* 117 (3) (2009) 320–325.
- [13] M. Koelsch, S. Cassaignon, J.F. Guillemoles, J.P. Jolivet, Comparison of optical and electrochemical properties of anatase and brookite  $\text{TiO}_2$  synthesized by the sol–gel method, *Thin Solid Films* 403–404 (2002) 312–319.
- [14] H. Lin, L. Li, M. Zhao, X. Huang, X. Chen, G. Li, R. Yu, Synthesis of high-quality brookite  $\text{TiO}_2$  single-crystalline nanosheets with specific facets exposed: tuning catalysts from inert to highly reactive, *J. Am. Chem. Soc.* 134 (2012) 8328–8331.
- [15] M. Zhao, H. Xu, H. Chen, S. Ouyang, N. Umezawa, D. Wang, J. Ye, Photocatalytic reactivity of {121} and {211} facets of brookite  $\text{TiO}_2$  crystals, *J. Mater. Chem. A Mater. Energy Sustain.* 3 (2015) 2331–2337.
- [16] T.-D. Nguyen-Phan, E. Jung Kim, S. Hong Hahn, W.-J. Kim, E. Woo Shin, Synthesis of hierarchical rose bridal bouquet- and humming-top-like  $\text{TiO}_2$  nanostructures and their shape-dependent degradation efficiency of dye, *J. Colloid Interface Sci.* 356 (1) (2011) 138–144.
- [17] S. Okano, S. Yamamuro, T. Tanaka, Synthesis of brookite-typed titania from titanium chloride solution, *Sci. China. Ser. E Tech. Sci.* 52 (1) (2009) 190–192.
- [18] B. Castañeda, W. Ortiz-Cala, C. Gallardo-Cabrera, N. Sbarbati Nudelman, Stability studies of alprazolam tablets: effect of chemical interaction with some excipients in pharmaceutical solid preparations, *J. Phys. Org. Chem.* 22 (2009) 807–814.
- [19] P. Pérez-Lozano, E. García-Montoya, A. Orriols, M. Miñarro, J.R. Ticó, J.M. Suñé-Negre, Development and validation of a new HPLC analytical method for the determination of alprazolam in tablets, *J. Pharm. Biomed. Anal.* 34 (2004) 979–987.
- [20] K. van der Ven, W. Van Dongen, B.U.W. Maes, E.L. Esmans, R. Blust, W.M. De Coen, Determination of diazepam in aquatic samples by capillary liquid chromatography–electrospray tandem mass spectrometry, *Chemosphere* 57 (2004) 967–973.
- [21] C. Gallardo Cabrera, R. Goldberg de Waisbaum, N. Sbarbati Nudelman, Kinetic and mechanistic studies on the hydrolysis and photodegradation of diazepam and alprazolam, *J. Phys. Org. Chem.* 18 (2005) 156–161.
- [22] J.P. Bound, K. Kitsou, N. Voulvoulis, Household disposal of pharmaceuticals and perception of risk to the environment, *Environ. Toxicol. Phar.* 21 (2006) 301–307.
- [23] V. Calisto, V.I. Esteves, Psychiatric pharmaceuticals in the environment, *Chemosphere* 77 (2009) 1257–1274.
- [24] V. Calisto, M.R.M. Domingues, V.I. Esteves, Photodegradation of psychiatric pharmaceuticals in aquatic environments – kinetics and photodegradation products, *Water Res.* 45 (2011) 6097–6106.
- [25] B.D. Cullity, S.R. Stock, Elements of X-ray Diffraction, third ed., Prentice Hall, New Jersey, 2001.
- [26] S. Brunauer, P.H. Emmett, E. Teller, Adsorption of gases in multimolecular layers, *J. Am. Chem. Soc.* 60 (1938) 309–319.
- [27] S.J. Gregg, K.S.W. Sing, Adsorption, Surface Area and Porosity, Academic Press, London, 1982, p. 126.
- [28] F. Rouquerol, J. Rouquerol, K. Sing, Adsorption by Powders and Porous Solids, Academic Press, London, 1999, p. 111.
- [29] E.P. Barret, L.G. Joyner, P.P. Halenda, The determination of pore volume and area distributions in porous substances. I. Computations from nitrogen isotherms, *J. Am. Chem. Soc.* 73 (1951) 373–380.
- [30] A. Golubović, N. Tomić, N. Finčur, B. Abramović, I. Veljković, J. Zdravković, M. Grujić-Brojčin, B. Babić, B. Stojadinović, M. Šćepanović, Synthesis of pure and La-doped anatase nanopowders by sol–gel and hydrothermal methods and their efficiency in photocatalytic degradation of alprazolam, *Ceram. Int.* 40 (2014) 13409–13418.
- [31] S.-D. Mo, W.Y. Ching, Electronic and optical properties of three phases of titanium dioxide: rutile, anatase, and brookite, *Phys. Rev. B* 51 (1995) 13023–13032.

- [32] W. Hu, L. Li, G. Li, C. Tang, L. Sun, High-quality brookite TiO<sub>2</sub> flowers: synthesis, characterization, and dielectric performance, *Cryst. Growth Des.* 9 (2009) 3676–3682.
- [33] S. El-Sherbiny, F. Morsy, M. Samir, O.A. Fouad, Synthesis, characterization and application of TiO<sub>2</sub> nanopowders as special paper coating pigment, *Appl. Nanosci.* 4 (2014) 305–313.
- [34] B.C. Viana, O.P. Ferreira, A.G. Souza Filho, J. Mendes Filho, O.L. Alves, Structural, morphological and vibrational properties of titanate nanotubes and nanoribbons, *J. Braz. Chem. Soc.* 20 (1) (2009) 167–175.
- [35] J. Rouquerol, D. Avnir, C.W. Fairbridge, D.H. Everett, J.H. Haynes, N. Pemicone, J.D.F. Ramsay, K.S.W. Sing, K.K. Unger, Recommendations for the characterization of porous solids (Technical Report), *Pure Appl. Chem.* 66 (1994) 1739–1758.
- [36] T.A. Kandiel, A. Feldhoff, L. Robben, R. Dillert, D.W. Bahnemann, Tailored titanium dioxide nanomaterials: anatase nanoparticles and brookite nanorods as highly active photocatalysts, *Chem. Mater.* 22 (2010) 2050–2060.
- [37] A.A. Ismail, T.A. Kandiel, D.W. Bahnemann, Novel (and better?) titania-based photocatalysts: brookite nanorods and mesoporous structures, *J. Photochem. Photobiol. A* 216 (2010) 183–193.
- [38] B.C. Viana, O.P. Ferreira, A.G. Souza Filho, A.A. Hidalgo, J. Mendes Filho, O.L. Alves, Alkali metal intercalated titanate nanotubes: a vibrational spectroscopy study, *Vib. Spectrosc.* 55 (2011) 183–187.
- [39] M.C. Ferrara, L. Pilloni, S. Mazzarelli, L. Tapfer, Hydrophilic and optical properties of nanostructured titania prepared by sol–gel dip coating, *J. Phys. D: Appl. Phys.* 43 (2010) 095301 (1–9).
- [40] T.A. Kandiel, L. Robben, A. Alkaima, D. Bahnemann, Brookite versus anatase TiO<sub>2</sub> photocatalysts: phase transformations and photocatalytic activities, *Photochem. Photobiol. Sci.* 12 (2013) 602–609.
- [41] M. Grujić-Brojčin, S. Armaković, N. Tomić, B. Abramović, A. Golubović, B. Stojadinović, A. Kremenović, B. Babić, Z. Dohčević-Mitrović, M. Šćepanović, Surface modification of sol–gel synthesized TiO<sub>2</sub> nanoparticles induced by La-doping, *Mat. Char.* 88 (2014) 30–41.
- [42] M. Šćepanović, B. Abramović, A. Golubović, S. Kler, M. Grujić-Brojčin, Z. Dohčević-Mitrović, B. Babić, B. Matović, Z.V. Popović, Photocatalytic degradation of metoprolol in water suspension of TiO<sub>2</sub> nanopowders prepared using sol–gel route, *J. Sol–Gel Sci. Technol.* 61 (2012) 390–402.
- [43] S. Bakardjieva, V. Stengl, L. Szatmary, J. Subrt, J. Lukac, N. Murafa, D. Niznansky, K. Cizek, J. Jirkovskyc, N. Petrova, Transformation of brookite-type TiO<sub>2</sub> nanocrystals to rutile: correlation between microstructure and photoactivity, *J. Mater. Chem.* 16 (2006) 1709–1716.
- [44] V. Iancu, M. Baia, L. Diamandescu, Zs Pap, A.M. Vlaicu, V. Danciu, L. Baia, Weighting the influence of TiO<sub>2</sub> anatase/brookite ratio in TiO<sub>2</sub>-Ag porous nanocomposites on visible photocatalytic performances, *Mater. Chem. Phys.* 141 (2013) 234–239.



# WO<sub>3</sub>/TiO<sub>2</sub> composite coatings: Structural, optical and photocatalytic properties



Zorana Dohčević-Mitrović<sup>a,\*</sup>, Stevan Stojadinović<sup>c</sup>, Luca Lozzi<sup>d</sup>, Sonja Aškračić<sup>a</sup>, Milena Rosić<sup>e</sup>, Nataša Tomić<sup>a</sup>, Novica Paunović<sup>a</sup>, Saša Lazović<sup>b</sup>, Marko G. Nikolić<sup>b</sup>, Sandro Santucci<sup>d</sup>

<sup>a</sup> Center for Solid State Physics and New Materials, Institute of Physics Belgrade, University of Belgrade, Pregrevica 118, 11080 Belgrade, Serbia

<sup>b</sup> Institute of Physics Belgrade, University of Belgrade, Pregrevica 118, 11080 Belgrade, Serbia

<sup>c</sup> Faculty of Physics, University of Belgrade, Studentski Trg 12-16, 11000 Belgrade, Serbia

<sup>d</sup> Department of Physical and Chemical Sciences, University of L'Aquila, Via Vetoio 67100, L'Aquila, Italy

<sup>e</sup> Laboratory for Material Science, Institute of Nuclear Sciences, Vinča, University of Belgrade, P.O. Box 522, 11001 Belgrade, Serbia

## ARTICLE INFO

### Article history:

Received 24 February 2016

Received in revised form 19 May 2016

Accepted 6 June 2016

Available online 7 June 2016

### Keywords:

- A. Nanostructures
- A. Oxides
- D. Crystal structure
- B. Optical properties
- D. Catalytic properties

## ABSTRACT

WO<sub>3</sub>/TiO<sub>2</sub> and TiO<sub>2</sub> coatings were prepared on titania substrates using facile and cost-effective plasma electrolytic oxidation process. The coatings were characterized by X-ray diffraction, scanning electron microscopy, Raman, UV–vis diffuse reflectance spectroscopy, and X-ray photoelectron spectroscopy. With increasing duration of PEO process, the monoclinic WO<sub>3</sub> phase became dominant and new monoclinic WO<sub>2.96</sub> phase appeared. The optical absorption edge in the WO<sub>3</sub>/TiO<sub>2</sub> samples, enriched with WO<sub>3</sub>/WO<sub>2.96</sub> phase, was shifted to the visible region. The photocatalytic efficiency of WO<sub>3</sub>/TiO<sub>2</sub> and pure TiO<sub>2</sub> samples was evaluated by performing the photodegradation experiments in an aqueous solution of Rhodamine 6G and Mordant Blue 9 under the visible and UV light. The WO<sub>3</sub>/TiO<sub>2</sub> catalysts are much more efficient than pure TiO<sub>2</sub> under visible light and slightly better under UV light. The improvement of photocatalytic activity in the visible region is attributed to better light absorption, higher adsorption affinity and increased charge separation efficiency.

© 2016 Elsevier Ltd. All rights reserved.

## 1. Introduction

Among semiconductor materials, titanium dioxide (TiO<sub>2</sub>) in anatase phase has been shown as excellent and widely used photocatalyst for the degradation of different organic contaminants, because of its physical and chemical stability, high oxidative power, high catalytic activity, long-term photostability, low cost and ease of production. Many organic compounds can be decomposed in an aqueous solution in the presence of TiO<sub>2</sub>, illuminated by photons with energies greater than or equal to the band gap energy of titanium dioxide (3.2 eV for anatase TiO<sub>2</sub>) [1–6]. The major drawback for TiO<sub>2</sub> commercial use lies in its wide band gap, and relatively high recombination rate of photoinduced electron-hole pairs. The modification of TiO<sub>2</sub> by doping with metals and non-metals [7–12] or by Ti<sup>3+</sup> self-doping [13,14] have been extensively performed in order to improve its photocatalytic activity under the visible irradiation.

Another very promising approach is the combination of TiO<sub>2</sub> with metal oxides like V<sub>2</sub>O<sub>5</sub>, ZnS, InVO<sub>4</sub>, WO<sub>3</sub> [15–19] or graphene [20]. Among the metal oxides, WO<sub>3</sub> has smaller band gap (2.8 eV) than TiO<sub>2</sub> and better absorbs visible light. Moreover, WO<sub>3</sub> has a suitable conduction band potential and acts as a trapping site for photoexcited electrons from TiO<sub>2</sub>. The photogenerated holes from the valence band of WO<sub>3</sub> move towards and accumulate in the valence band of TiO<sub>2</sub>. In such a way the efficiency of charge separation is increased, enhancing at the same time the photocatalytic activity of TiO<sub>2</sub> [21]. Additionally, the formation of WO<sub>3</sub> monolayer on TiO<sub>2</sub> increases the acidity of the WO<sub>3</sub>/TiO<sub>2</sub> surface enabling the adsorption of greater amount of hydroxyl groups and organic reactants on the surface [21,22]. In recent years, WO<sub>3</sub>/TiO<sub>2</sub> composites were synthesized using different methods such as sol-gel, ultrasonic spray pyrolysis, ball milling, hydrothermal, sol-precipitation, and impregnation to improve photocatalytic activity of TiO<sub>2</sub> under the visible light [23–28]. Thin films of TiO<sub>2</sub>/WO<sub>3</sub> have also been prepared by dip and spin coating [29,30] or by one-step oxidation method [31]. In most of these reports it was demonstrated that WO<sub>3</sub>/TiO<sub>2</sub> composites were found to have much

\* Corresponding author

E-mail address: [zordoh@ipb.ac.rs](mailto:zordoh@ipb.ac.rs) (Z. Dohčević-Mitrović).

higher photocatalytic activity under the visible light than pure TiO<sub>2</sub> [24,26,28,31]. Therefore, the combination of these two materials can lead to increased charge carrier lifetime and improved photocatalytic activity under the visible irradiation. Among different synthesis routes, plasma electrolytic oxidation (PEO) process is very facile, cost-effective and environmentally benign process for producing of well-adhered and crystalline oxide films, but the studies on structural and photocatalytic properties of WO<sub>3</sub>/TiO<sub>2</sub> films (coatings), produced by PEO process, are limited [32–34].

In this study WO<sub>3</sub>/TiO<sub>2</sub> coatings were synthesized on titanium substrate by using PEO process. Structural and optical properties of the coatings were fully characterized by XRD, SEM, Raman, XPS, and diffuse reflectance spectroscopy. The aim of this work was to tailor the band gap energy of WO<sub>3</sub>/TiO<sub>2</sub> coatings towards the visible spectral region, varying the time of PEO process and to explore the photocatalytic properties of the coatings. The photocatalytic efficiency of WO<sub>3</sub>/TiO<sub>2</sub> coatings was tested under the visible and UV light irradiation using Rhodamine 6G and Mordant Blue 9 as model pollutants. We demonstrated that this approach provides an efficient route for the formation of cost-effective and improved visible-light-driven photocatalysts.

## 2. Experimental

### 2.1. Preparation of WO<sub>3</sub>/TiO<sub>2</sub> coatings

WO<sub>3</sub>/TiO<sub>2</sub> coatings were prepared on titanium substrate using plasma electrolytic oxidation (PEO) process. PEO process is an anodizing process of lightweight metals (aluminum, magnesium, zirconium, titanium, etc.) or metal alloys above the dielectric breakdown voltage, when thick, highly crystalline oxide coating with high corrosion and wear resistance, and other desirable properties are produced. During the PEO process, numerous small sized and short-lived discharges are generated continuously over the coating's surface, accompanied by gas evolution. Due to increased local temperature, plasma-chemical reactions are induced at the discharge sites modifying the structure, composition, and morphology of such oxide coatings. The oxide coatings formed by PEO process usually contain crystalline and amorphous phases with constituent species originating both from metal and electrolyte. WO<sub>3</sub>/TiO<sub>2</sub> coatings were formed on the rectangular titanium samples (99.5% purity, Alfa Aesar) of dimensions 25 mm × 10 mm × 0.25 mm, which were used as working electrodes in the experiment. The working electrodes were sealed with insulation resin leaving only an area of 1.5 cm<sup>2</sup> as an active surface. Before starting the PEO process, titanium samples were degreased in acetone, ethanol, and distilled water, using ultrasonic cleaner and dried in a warm air stream. The anodic oxidation process was conducted in an aqueous solution of 10<sup>-3</sup> M 12-tungstosilicic acid (H<sub>4</sub>SiW<sub>12</sub>O<sub>40</sub>), at constant current density (150 mA/cm<sup>2</sup>). During PEO process, the electrolyte circulated through the chamber-reservoir system. The temperature of the electrolyte was kept fixed at (20 ± 1) °C. Detailed description of PEO process is given in the ref. [33].

After plasma electrolytic oxidation, the samples were rinsed in distilled water to prevent additional deposition of electrolyte components during drying. The WO<sub>3</sub>/TiO<sub>2</sub> samples were obtained by varying the time of PEO process from 90 s up to 300 s. The pure TiO<sub>2</sub> sample was obtained after 300 s of PEO process.

### 2.2. Characterization of WO<sub>3</sub>/TiO<sub>2</sub> coatings

The crystal structure of WO<sub>3</sub>/TiO<sub>2</sub> samples was analyzed by X-ray diffraction (XRD), using a Rigaku Ultima IV diffractometer in Bragg-Brentano geometry, with Ni-filtered CuK $\alpha$  radiation

( $\lambda = 1.54178 \text{ \AA}$ ). Diffraction data were acquired over the scattering angle  $2\theta$  from 15° to 75° with a step of 0.02° and acquisition rate of 2°/min. The XRD spectra refinement was performed with the software package Powder Cell. The TCH pseudo-Voigt profile function gave the best fit to the experimental data.

Scanning electron microscope (SEM) JEOL 840A equipped with an EDS detector was used to characterize the morphology and chemical composition of formed oxide coatings.

Micro-Raman scattering measurements were performed at room temperature in a backscattering geometry, using a Jobin-Yvon T64000 triple spectrometer system and Nd:YAG laser line of 532 nm as an excitation source. The incident laser power was kept less than 10 mW in order to prevent the heating effects.

UV-vis diffuse reflectance spectra were acquired using the Specord M40 Carl Zeiss spectrometer.

X-ray photoelectron spectroscopy (XPS) was used for the surface composition analysis of WO<sub>3</sub>/TiO<sub>2</sub> coatings. XPS was carried out on a VG ESCALAB II electron spectrometer with a base pressure in the analysis chamber of 10<sup>-8</sup> Pa. The X-ray source was monochromatized AlK $\alpha$  radiation (1486.6 eV) and the instrumental resolution was 1 eV. The spectra were calibrated using the C 1 s line (284.8 eV) of the adventitious carbon and corrected by subtracting a Shirley-type background.

### 2.3. Photocatalytic experiments

The photocatalytic activity of WO<sub>3</sub>/TiO<sub>2</sub> samples was evaluated by monitoring the decomposition of Rhodamine 6G (R6G) and Mordant Blue 9 (MB9) under the irradiation of two different light sources: fluorescent and UV lamps. The photocatalytic measurements on R6G solution (initial concentration in water: 10 mg/L) have been performed using a 36W visible fluorescent lamp (Hyundai eagle), whose emission spectrum, compared to sunlight spectrum, is given in Ref. [9]. The cuvette (3 mL) was placed at about 5 cm from the lamp. The evolution of the rhodamine concentration was followed by measuring the variation of the intensity of main absorption peak at ~525 nm. UV-vis absorption measurements as a function of the light exposure time were performed by using USB2000 spectrometer by Ocean Optics. The solution was placed in the dark for 60 min to reach the adsorption/desorption equilibrium before visible light exposure.

The photocatalytic activity of WO<sub>3</sub>/TiO<sub>2</sub> samples under UV light irradiation was evaluated using aqueous solution of MB9 as a model pollutant. Batch type experiments were performed in an open thermostated cell (at 25 °C). The cell was equipped with a water circulating jacket to maintain the solution at room temperature. A mercury lamp (125 W) was used as a light source and was placed 13 cm above the surface of the dye solution. The initial concentration of MB9 in an aqueous suspension was 50 mg/L and the working volume was 25 mL. Before the lamp was switched on, the cell was kept in dark for 60 min in order to achieve the adsorption-desorption equilibrium. At regular time intervals the aliquots were taken and the concentration of the dye was determined by UV-vis spectrophotometer (Super Scan) at  $\lambda_{max} = 516 \text{ nm}$ . The photocatalytic experiments were conducted at the natural pH of the dyes (pH = 7 in a case of R6G solution and at pH = 6 in a case of MB9 solution). All photocatalytic measurements were repeated at least twice to check their reproducibility.

In order to detect the formation of free hydroxyl radicals (OH $\cdot$ ) on the UV illuminated WO<sub>3</sub>/TiO<sub>2</sub> surface, photoluminescence (PL) measurements were performed using terephthalic acid, which is known to react with OH $\cdot$  radicals and produces highly fluorescent 2-hydroxyterephthalic acid. The experiment was conducted at ambient temperature. The WO<sub>3</sub>/TiO<sub>2</sub> photocatalyst (TW300) was placed in open thermostated cell filled with 20 mL of the  $5 \times 10^{-4} \text{ mol L}^{-1}$  terephthalic acid in a diluted NaOH aqueous solution with

a concentration of  $2 \times 10^{-3} \text{ mol L}^{-1}$ . UV lamp (125 W) was used as a light source. Sampling was performed after 15, 30, 60 and 90 min. PL spectra of reaction solution, using excitation wavelength of 315 nm, were measured on a Spex Fluorolog spectrofluorometer system at wavelength of 425 nm for which the 2-hydroxyterephthalic acid exhibits intense PL peak.

### 3. Results and discussion

#### 3.1. Crystal structure and morphology

XRD patterns of the  $\text{WO}_3/\text{TiO}_2$  samples obtained for 90 (TW90), 120 (TW120), and 300 s (TW300) of PEO process are presented in Fig. 1. The diffraction peaks which appear in TW90 sample at  $2\theta = 23.3^\circ, 33.4^\circ, 54.2^\circ$  belong to (002), (022) and (042) planes of monoclinic  $\text{WO}_3$  phase, which crystallizes in  $P2_1/c$  (No. 14) space group. Besides these XRD peaks, the XRD pattern also shows peak at  $25.3^\circ$  which belongs to  $\text{TiO}_2$  anatase crystal phase (space group  $I4_1/amd$  (No. 141)) and intense peaks of elemental Ti (space group  $P6_3/mmc$  (No. 194)). This indicates that Ti substrate is not completely oxidized to form  $\text{TiO}_2$  during the PEO process. With increasing duration of PEO process, for the TW120 and TW300 samples, the XRD peaks of  $\text{WO}_3$  phase became more intense. The spectra refinement, using Powder Cell program, showed that besides  $\text{WO}_3$  phase a monoclinic  $\text{WO}_{2.96}$  phase appeared (space group  $P2/c$  (No. 13)). Furthermore, the intensities of XRD peaks which belong to  $\text{TiO}_2$  phase and elemental Ti decreased implying that the  $\text{WO}_3/\text{TiO}_2$  coatings were enriched with  $\text{WO}_3/\text{WO}_{2.96}$  phase. According to the JCPDS database for  $\text{WO}_3$ ,  $\text{WO}_{2.96}$ ,  $\text{TiO}_2$ , and elemental Ti (JCPDS: 43-1035 ( $\text{WO}_3$ ), 30-1387 ( $\text{WO}_{2.96}$ ), 16-0934 ( $\text{TiO}_2$ ) and 44-1294 (elemental Ti)) very good agreement is obtained between experimental and calculated diffraction patterns of the  $\text{WO}_3/\text{TiO}_2$  samples. In Fig. 1 are marked main XRD peaks of  $\text{WO}_3$  and  $\text{WO}_{2.96}$  phases for clarity. The lattice parameters and the estimated volume fractions (%) of different phases for the  $\text{WO}_3/\text{TiO}_2$  samples are given in Table 1.

In Fig. 2 are presented SEM images of  $\text{WO}_3/\text{TiO}_2$  samples. In the TW90 sample produced with shorter PEO time, certain number of microdischarge channels together with molten regions was present because of the rapid cooling of the electrolyte. With increasing time of PEO process, when the thickness of the oxide coating was increased, the number of microdischarge channels and

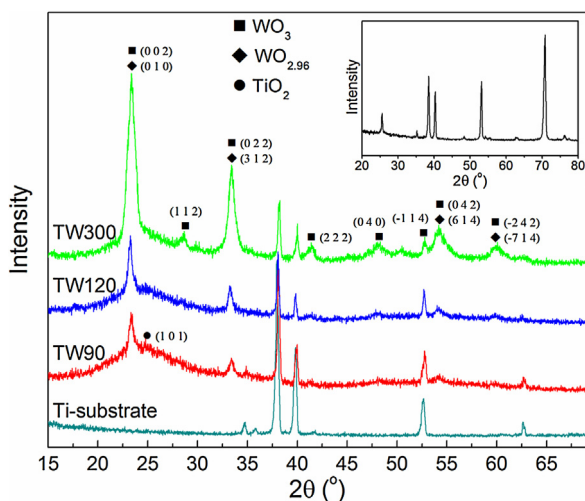


Fig. 1. XRD patterns of TW90, TW120 and TW300 samples formed in various stages of PEO process, together with the XRD spectrum of Ti-substrate. In the inset is given XRD spectrum of anatase  $\text{TiO}_2$  obtained on Ti-substrate after 300 s of PEO process.

Table 1  
Phase fraction (vol%) and cell parameters (Å) of  $\text{WO}_3/\text{TiO}_2$  samples.

Phase	TW90	TW120	TW300
$\text{WO}_3$	$a = 7.4060$	$a = 7.3026$	$a = 7.4060$
	$b = 7.6400$	$b = 7.5398$	$b = 7.5177$
	$c = 7.6455$	$c = 7.6933$	$c = 7.5920$
	29.6%	29.1%	54.5%
$\text{WO}_{2.96}$	/	$a = 11.9006$	$a = 11.8000$
		$b = 3.8258$	$b = 3.8098$
		$c = 59.6312$	$c = 59.7400$
		36.70%	20.90%
$\text{TiO}_2$	$a = 3.7778,$	$a = 3.7841,$	$a = 3.7790$
	$c = 9.4440,$	$c = 9.5105,$	$c = 9.4124$
	66.0%	32.2%	23.8%
Ti	$a = 2.9481$	$a = 2.9594$	$a = 3.0510$
	$c = 4.7325$	$c = 4.7254$	$c = 4.7820$
	4.3%	2.0%	0.9%

micropores decreased followed by increased roughness of the coating's surface.

The quantitative elemental analysis confirmed the presence of Ti, O and W and the elemental composition of the samples is shown in Table 2. EDS analysis confirmed the increasing trend of W content with increasing of PEO time.

#### 3.2. Raman and diffuse reflectance spectra

The Raman spectra of  $\text{WO}_3/\text{TiO}_2$  samples produced for different duration of PEO process are shown in Fig. 3a. Several modes originating from two crystalline oxide phases can be identified (marked on Fig. 3a as T and W).

The Raman modes positions were determined using Lorentzian fit procedure and the deconvoluted spectra of TW90, TW120 and TW300 samples are presented in Fig. 3b. Besides the modes at about  $144 \text{ cm}^{-1}$  ( $E_{g(1)}$ ),  $197 \text{ cm}^{-1}$  ( $E_{g(2)}$ ),  $393 \text{ cm}^{-1}$  ( $B_{1g(1)}$ ),  $516 \text{ cm}^{-1}$  ( $A_{1g}$ ,  $B_{1g(2)}$ ) and  $638 \text{ cm}^{-1}$  ( $E_{g(3)}$ ) which belong to anatase phase of  $\text{TiO}_2$  [35], several modes characteristic for monoclinic  $\text{WO}_3$  phase are present [22,36,37]. The broad band at  $\sim 703 \text{ cm}^{-1}$  and strong band at  $\sim 793 \text{ cm}^{-1}$  are assigned to the stretching (O–W–O) modes of the bridging oxygen of the  $\text{WO}_6$  octahedra. The bands observed at  $\sim 272 \text{ cm}^{-1}$  and at  $\sim 316 \text{ cm}^{-1}$  are assigned to the bending (O–W–O) vibrations of bridging oxygen in monoclinic  $m\text{-WO}_3$  [22,37]. The band positioned at  $\sim 989 \text{ cm}^{-1}$  is assigned to the dioxo ( $\text{W}=\text{O})_2$  symmetric vibration of the isolated surface  $\text{WO}_4$  structure, whereas its weak shoulder at  $\sim 942 \text{ cm}^{-1}$  represents asymmetric vibration of the same atomic group [22,37]. The low frequency mode at  $58 \text{ cm}^{-1}$  belongs to the lattice modes of monoclinic  $\text{WO}_3$  phase [38].

Further, from the Lorentzian fit procedure it was obtained that the ratio between the intensity of the peak positioned at  $639 \text{ cm}^{-1}$  and the sum of the intensities of the  $703 \text{ cm}^{-1}$  and  $793 \text{ cm}^{-1}$  peaks decreased with the increase of PEO time. This fact supports the XRD results that  $\text{WO}_3$  content increases with prolonged duration of PEO process.

In Fig. 4 are presented the Raman spectra of TW90, TW120 and TW300 samples in the C–H and O–H region. The Raman band at around  $2885 \text{ cm}^{-1}$  originates from the overlapped  $\text{CH}_3$  and  $\text{CH}_2$  stretching vibrations [39]. Broad Raman peak in the  $3000\text{--}3600 \text{ cm}^{-1}$  frequency range can be assigned to the O–H stretching vibration of water molecules adsorbed on the surface of the  $\text{WO}_3/\text{TiO}_2$  coatings [3,5].

The absorption spectra of TW90, TW120 and TW300 samples are given in Fig. 5a. With increasing content of  $\text{WO}_3$  phase the absorption edge shifts to higher wavelengths. In the spectra of TW120 a structure around  $380\text{--}400 \text{ nm}$  can be observed, which is

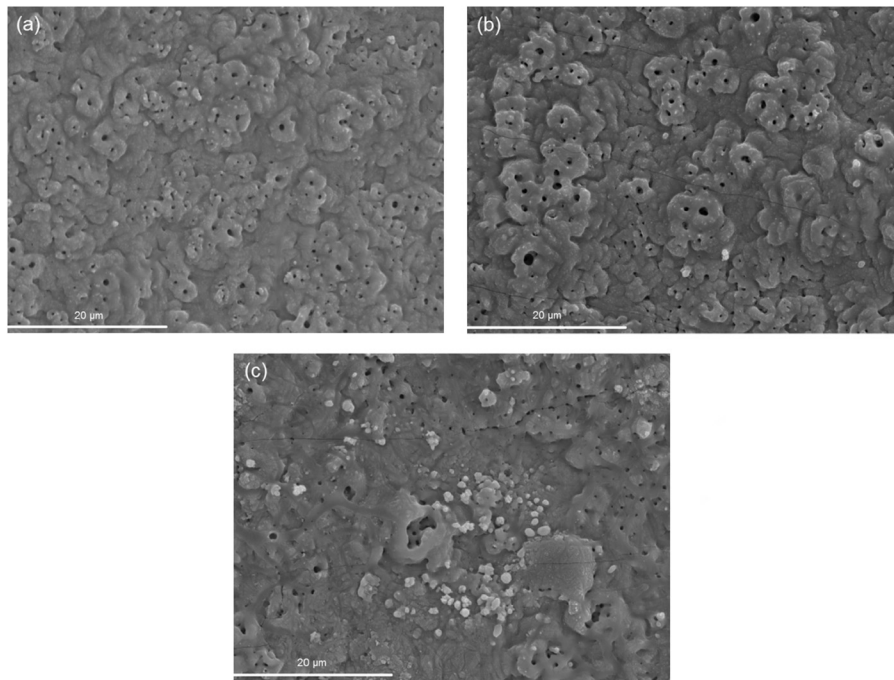


**Fig. 2.** SEM micrographs of  $\text{WO}_3/\text{TiO}_2$  samples formed in various stages of PEO process: (a) TW90, (b) TW120 and (c) TW300 sample.

very pronounced in the TW300 sample. The appearance of this absorption structure can be attributed to the electronic population of  $\text{WO}_3$  conduction band [40]. From the absorption spectra from Fig. 4a, applying the same procedure as Ghobadi in his work [41], the band gap energies for pure  $\text{TiO}_2$  and  $\text{WO}_3/\text{TiO}_2$  samples were estimated. In Fig. 5b are presented the Tauc plots for indirect transition, as  $\text{TiO}_2$  and  $\text{WO}_3$  are indirect band gap semiconductors [26]. The band gap ( $E_g$ ) energies are 3.19 eV for pure  $\text{TiO}_2$ , and 2.84, 2.77 and 2.6 eV for TW90, TW120 and TW300 samples, respectively. It is obvious that with increasing  $\text{WO}_3$  content the band gap decreases compared to pure  $\text{TiO}_2$  and shifts to the visible spectral range. Patrocínio et al. [40] have shown that in  $\text{TiO}_2/\text{WO}_3$  films, the  $\text{WO}_3$  conduction band introduces new low lying electronic levels with respect to the conduction band of  $\text{TiO}_2$ , causing the lowering of the band gap energy of composite samples compared to pure  $\text{TiO}_2$ . This finding is in accordance with the band gap behavior of our  $\text{WO}_3/\text{TiO}_2$  samples from Fig. 5b.

### 3.3. XPS analysis

The XPS study was further used to confirm the chemical binding states of W 4f. The W 4f XPS spectra of the TW90 and TW300 samples and the results of their decomposition into peaks are shown in Fig. 6. The W 4f spectrum of TW90 sample (Fig. 6a) can be deconvoluted into one doublet with binding energies of 35.8 (W  $4f_{7/2}$ ) and 38.1 eV (W  $4f_{5/2}$ ), respectively. The energy position of this doublet corresponds to the  $\text{W}^{6+}$  oxidation state [42].

In the TW300 sample (Fig. 6c) the contribution of  $\text{W}^{5+}$  states from nonstoichiometric oxide phase can be seen. The W 4f

spectrum can be deconvoluted with two doublets. The first two characteristic peaks at 36 (W  $4f_{7/2}$ ) and 38.3 eV (W  $4f_{5/2}$ ) correspond to  $\text{W}^{6+}$  state as in the case of TW90. The binding energies of these peaks are somewhat higher than that for TW90 sample. The up-shift in binding energy can be ascribed to the presence of defects and OH-groups on the surface [43], existence of

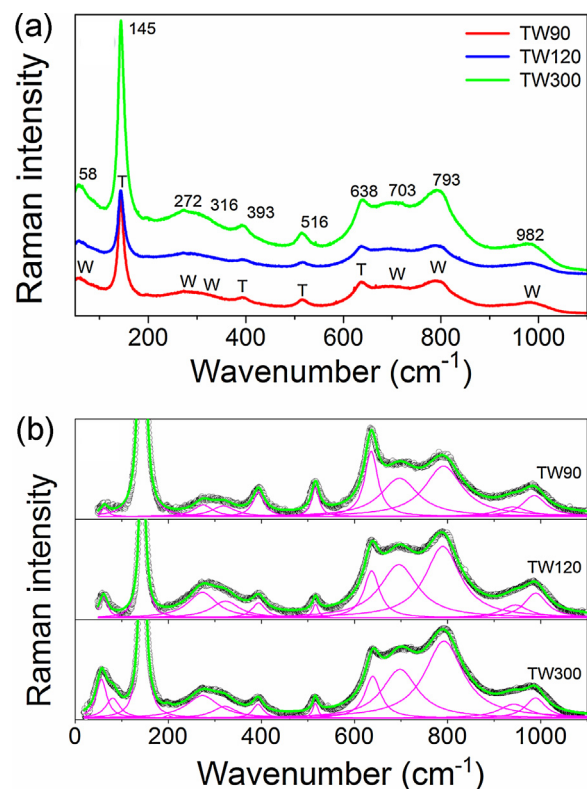


**Fig. 3.** Room-temperature Raman spectra of  $\text{WO}_3/\text{TiO}_2$  samples (a). The  $\text{TiO}_2$  and  $\text{WO}_3$  Raman modes are marked as T and W. Deconvoluted Raman spectra of TW90, TW120 and TW300 samples (b).

**Table 2**  
EDS analysis of the  $\text{WO}_3/\text{TiO}_2$  composites.

Sample	EDS data			
	Ti (at%)	W (at%)	O (at%)	W/Ti
TW90	6.98	14.17	78.85	2.03
TW120	6.22	16.12	77.66	2.59
TW300	4.09	17.16	78.75	4.1

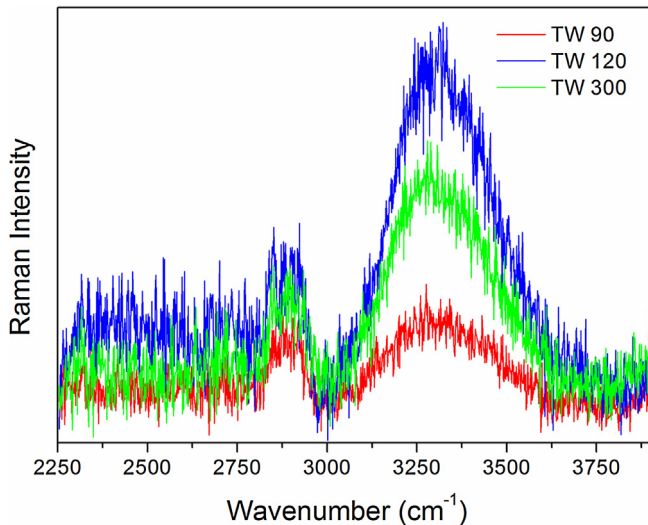


Fig. 4. Raman spectra of  $\text{WO}_3/\text{TiO}_2$  samples in the C–H and O–H spectral region.

which is confirmed by Raman analysis (Fig. 4). The binding energies of the second doublet at 34.5 ( $\text{W } 4f_{7/2}$ ) and 36.5 eV ( $\text{W } 4f_{5/2}$ ) correspond to  $\text{W}^{5+}$  state [42]. These results are in accordance with XRD analysis.

The O 1s spectra of TW90 and TW300 samples (Fig. 6b, d) are decomposed into three peaks. The major peak at binding energy of 531.2 eV can be assigned to the oxygen atoms in  $\text{WO}_3$  and to the OH-groups present on the surface [32,44]. The second peak observed at 530.6 eV has been attributed to oxygen bound to Ti [26], whereas the binding energy of the third peak at 533.1 eV corresponds to the oxygen in water molecules bound in the coating's structure or adsorbed on its surface [45]. The relative intensity of the XPS peaks at 531.2 eV and 533.1 eV was increased in the TW300 sample. The intensity increase of these peaks can be related to the presence of sub-stoichiometric  $\text{WO}_{3-x}$  phase ( $\text{WO}_{2.96}$ ). Similar behavior was reported in the paper of Shpak et al. [44] in which these peaks were more intense in  $\text{WO}_{3-x}$  oxides than in stoichiometric  $\text{WO}_3$ . This finding is also supported by the Raman spectrum of TW300 sample (Fig. 4), for which the intensity of the Raman mode, corresponding to the water molecules adsorbed on the surface, is higher than in TW90 sample.

#### 3.4. Photocatalytic performances of $\text{WO}_3/\text{TiO}_2$ coatings

Fig. 7a shows the kinetics of degradation of R6G for pure  $\text{TiO}_2$  and  $\text{WO}_3/\text{TiO}_2$  samples under the visible light. No detectable

degradation of R6G was registered without the presence of  $\text{WO}_3/\text{TiO}_2$  samples (black circles on Fig. 7a). As can be seen from Fig. 7a, both  $\text{TiO}_2$  and  $\text{WO}_3/\text{TiO}_2$  coatings adsorbed the dye in the equilibrium period of 60 min before the exposure to visible light. It is known from the literature that the zero point charge ( $\text{pH}_{zpc}$ ) of  $\text{TiO}_2$  lies between 6 and 6.8 [46–48], whereas the isoelectric point of  $\text{WO}_3$  is even lower and lies in the range 1.5–2.5 [49]. At higher pH values than these  $\text{WO}_3$  and  $\text{TiO}_2$  surfaces should be negatively charged. Therefore, the adsorption of the R6G as cationic dye at  $\text{pH} = 7$ , points out that the surfaces of  $\text{WO}_3/\text{TiO}_2$  and  $\text{TiO}_2$  coatings are negative and attract the positively charged R6G. The dye adsorption ability can be crucial for the high catalytic activity of the catalyst, because it can enhance the electron/hole transfer efficiency and contact with photogenerated active species.

When  $\text{TiO}_2$  and  $\text{WO}_3/\text{TiO}_2$  samples were subjected to visible radiation, composite coatings have shown much better photo-efficiency and demonstrated to be far superior than pure  $\text{TiO}_2$ . The highest activity was observed for the TW90 and TW120 samples for which the photodegradation of R6G reached almost 80% after 60 min. With further increase of  $\text{WO}_3$  content, the photocatalytic efficiency slightly decreased, but is still much higher than for pure  $\text{TiO}_2$ .

Further, the photocatalytic activity of  $\text{WO}_3/\text{TiO}_2$  coatings for degradation of MB9 was tested under the UV light. In Fig. 7b is presented the photodegradation of MB9 in the presence of  $\text{WO}_3/\text{TiO}_2$  samples. In the dark,  $\text{WO}_3/\text{TiO}_2$  coatings showed no adsorption of MB9. The absence of adsorption can be explained by highly anionic character of MB9 and electrostatic repulsion between the dye and negatively charged surface of  $\text{WO}_3/\text{TiO}_2$  coatings.

The photocatalytic activity of  $\text{WO}_3/\text{TiO}_2$  samples was improved with increased content of  $\text{WO}_3$  phase, and the TW300 sample exhibited better activity than pure  $\text{TiO}_2$ . As can be seen from Fig. 7b, after 240 min more than 80% of dye was degraded in the presence of  $\text{WO}_3/\text{TiO}_2$  coatings.

Photocatalytic degradation of both dyes can be well described by first-order kinetic equation,  $\ln(C/C_0) = kt$ , where  $C_0$  is the initial dye concentration and  $C$  is the dye concentration at time  $t$ . The first order kinetic constant  $k$  is obtained from the slope of the  $\ln(C/C_0)$  versus  $t$  for both dyes. In Table 3 are given the first order rate constants for R6G and MB9 ( $k_{\text{R6G}}$ ,  $k_{\text{MB9}}$ ), together with the corresponding linear correlation coefficient ( $R^2$ ). In a case of R6G degradation under the visible light, the highest  $k$  value ( $k_{\text{R6G}}$ ) was obtained for the TW90 sample. In a case of MB9 degradation under UV light, value of  $k_{\text{MB9}}$  increased with increasing amount of  $\text{WO}_3$ .

The degradation rate constant  $k$  of  $\text{WO}_3/\text{TiO}_2$  coatings under visible light is almost five times higher than that of  $\text{TiO}_2$ , whereas its value under UV light are comparable with  $\text{TiO}_2$ , suggesting that

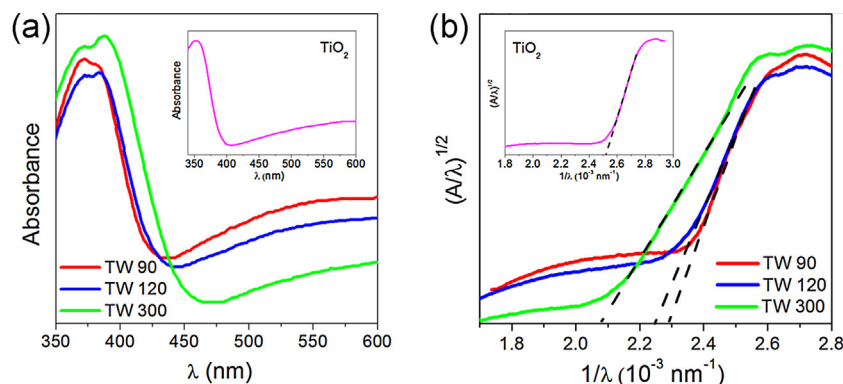


Fig. 5. Absorbance spectra (a) and Tauc plots for indirect band gap for  $\text{WO}_3/\text{TiO}_2$  samples (b). In the inset is given Tauc plot for indirect band gap for pure  $\text{TiO}_2$ .



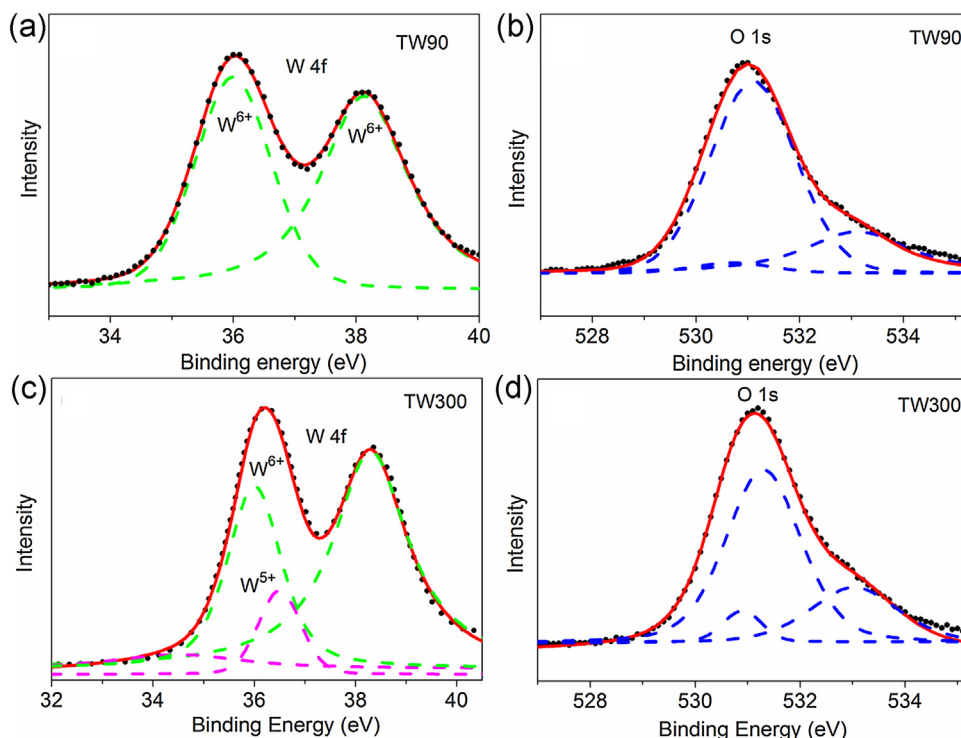


Fig. 6. XPS spectra of W 4f and O 1s regions for TW90 and TW300 samples.

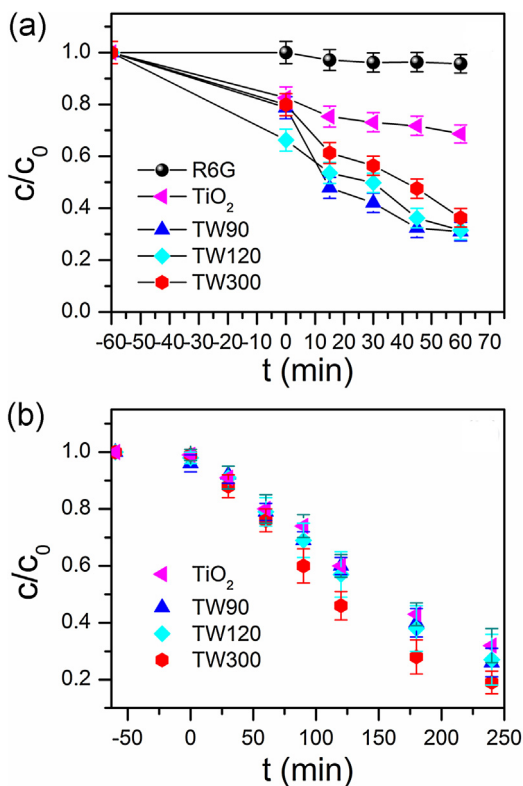


Fig. 7. Photocatalytic degradation of R6G under visible light (a) and MB9 under UV light (b) in the presence of  $\text{WO}_3/\text{TiO}_2$  and  $\text{TiO}_2$  coatings.

composite coatings are very efficient photocatalysts under visible light.

### 3.5. Hydroxyl radical analysis

The formation of free hydroxyl radicals ( $\text{OH}^*$ ) was tested on the surface of TW300 photocatalyst under UV irradiation and detected by PL method. Applying similar procedure as described in the paper of Su et al. [50], TW300 sample was placed in terephthalic acid solution and illuminated by UV light. PL spectra of the reaction solution were measured at room temperature after 15, 30, 60 and 90 min, and these spectra are presented in Fig. 8. The terephthalic acid reacts with  $\text{OH}^*$  producing 2-hydroxyterephthalic acid, which exhibits PL peak at 425 nm [51]. The intensity of this peak is proportional to the amount of  $\text{OH}^*$  produced in water [50,51]. As can be seen from Fig. 8, gradual increase of PL intensity at 425 nm with prolonged illumination time points at increasing amount of  $\text{OH}^*$  radicals produced at the surface of TW300 sample.

### 3.6. Mechanism of the reaction

The photocatalytic degradation of R6G or MB9 is initiated by the photoexcitation of the  $\text{WO}_3/\text{TiO}_2$  coatings when the electron-hole pairs are formed on the catalyst's surface. According to the

Table 3  
The pseudo-first rate constants for R6G and MB9 together with  $R^2$ .

Sample	$k_{\text{R6G}} \times 10^{-2} \text{ (min}^{-1}\text{)}$	$R^2$	$k_{\text{MB9}} \times 10^{-2} \text{ (min}^{-1}\text{)}$	$R^2$
TW90	1.52	0.975	0.44	0.990
TW120	1.24	0.957	0.47	0.982
TW300	1.20	0.963	0.65	0.966
$\text{TiO}_2$	0.28	0.888	0.41	0.963

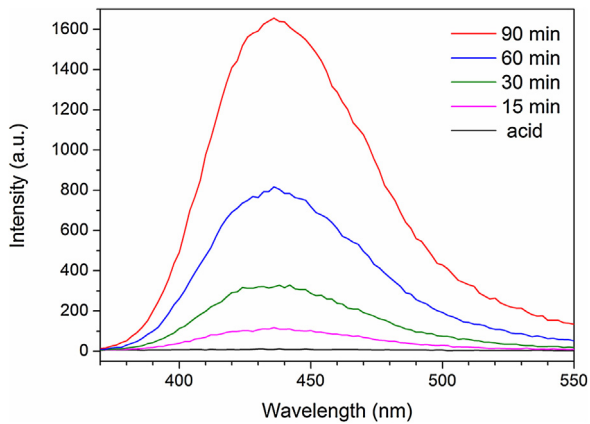
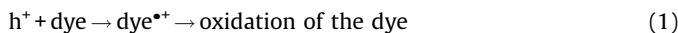


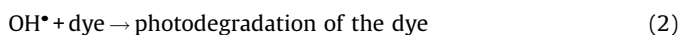
**Fig. 8.** PL spectral changes observed during UV illumination of TW300 sample in the solution of terephthalic acid after 15, 30, 60 and 90 min. The PL spectra of pure terephthalic acid is also presented.

generally accepted photoexcitation mechanism, electrons from the conduction band of  $\text{TiO}_2$  can easily diffuse into the conduction band of  $\text{WO}_3$  [40,52]. Since W(VI) can be easily reduced to W(V),  $\text{WO}_3$  acts as an acceptor of conduction band electrons from  $\text{TiO}_2$ , whereas the photogenerated holes migrate in the opposite direction, i.e. from the lower-lying valence  $\text{WO}_3$  band to the valence band of  $\text{TiO}_2$ . In such a way the charge separation efficiency can be increased.

In Fig. 9 is given an illustration of photo-induced electron-hole separation and reacting radicals formation. The presence of holes in the dye solution permits a direct oxidation of the dye, due to high oxidative potential of the holes ( $h^+$ ):



Further, hydroxyl radicals ( $\text{OH}^*$ ) are usually formed by the reaction between the holes and  $\text{OH}^-$  or water molecules present on the surface of the catalyst. The  $\text{OH}^*$  radicals attack the dye in aqueous solution leading to its degradation:



The photo-induced electrons can also react with dissolved oxygen to form superoxide ions ( $\text{O}_2^{\cdot-}$ ) which in contact with  $\text{H}_2\text{O}$  molecules form  $\text{OH}^-$  ions and finally  $\text{OH}^*$  radicals.

It is known from the literature that  $\text{WO}_3$  is almost 15 times more acidic than  $\text{TiO}_2$  [21,22,31], so it is expected that the surface of PEO produced  $\text{WO}_3/\text{TiO}_2$  coatings is more acidic than that of  $\text{TiO}_2$ , and has a higher affinity for chemical species having unpaired electrons. Because of higher acidity, the surface of  $\text{WO}_3/\text{TiO}_2$  coatings can absorb more  $\text{H}_2\text{O}$  and  $\text{OH}^-$  generating more  $\text{OH}^*$  radicals. The XPS and Raman spectra of  $\text{WO}_3/\text{TiO}_2$  composite coatings gave an evidence that adsorbed  $\text{H}_2\text{O}$  and hydroxyls are present on the surface of  $\text{WO}_3/\text{TiO}_2$  coatings, existence of which is important for the formation of  $\text{OH}^*$  radicals. PL measurements, performed on TW300 sample, (Fig. 8) clearly demonstrated that with increasing illumination time the increasing amount of  $\text{OH}^*$  radicals is formed on the surface of photocatalysts, which manifests through higher photocatalytic activity of TW300 sample.

The absorption measurements have shown that the band gap energy of  $\text{TiO}_2$  is higher than that of  $\text{WO}_3/\text{TiO}_2$  coatings. Namely, with prolonged time of PEO process, the  $\text{WO}_3$  content increases followed by an appearance of  $\text{WO}_{2.96}$  phase. As the conduction band of nonstoichiometric  $\text{WO}_{3-x}$  oxides is lower with respect to  $\text{WO}_3$  and  $\text{TiO}_2$  (Fig. 9) [53], the presence of  $\text{WO}_{2.96}$  phase will further reduce the band gap of  $\text{WO}_3/\text{TiO}_2$  samples towards the visible spectral range, as already noticed from the Tauc plots from Fig. 5. As a result, the electron-hole recombination will be more difficult and more reactive radicals can be produced at the  $\text{WO}_3/\text{TiO}_2$  surface. Therefore,  $\text{WO}_3/\text{TiO}_2$  coatings should be more efficient as catalysts under the visible light. The photocatalytic degradation of R6G and kinetics of the reaction confirmed that  $\text{WO}_3/\text{TiO}_2$  coatings are efficient photocatalysts in the visible region. Slight decrease of photocatalytic activity of TW300 sample in a case of R6G photodegradation (Fig. 7a) can be explained by the occurrence of photochromism [27,40]. Namely, the electron accumulation at the  $\text{WO}_3$  conduction band can be more pronounced with increased  $\text{WO}_3$  content. The accumulated electrons can react with  $\text{OH}^*$  radicals forming  $\text{OH}^-$  ions or can reduce the number of superoxide radicals [27,40] degrading at some extent the photocatalytic activity of  $\text{WO}_3/\text{TiO}_2$  coatings. The presence of pronounced absorption feature around 380–400 nm in the absorbance spectrum of TW300 sample confirms this assumption. Another reason can be found in the formation of small polarons, appearance of which is characteristic for  $\text{WO}_3$  and  $\text{WO}_{3-x}$  phases. The photoexcited electron-hole pairs can be rapidly quenched by recombination of photoexcited holes with electrons from localized polaron states, whereas photoexcited electrons

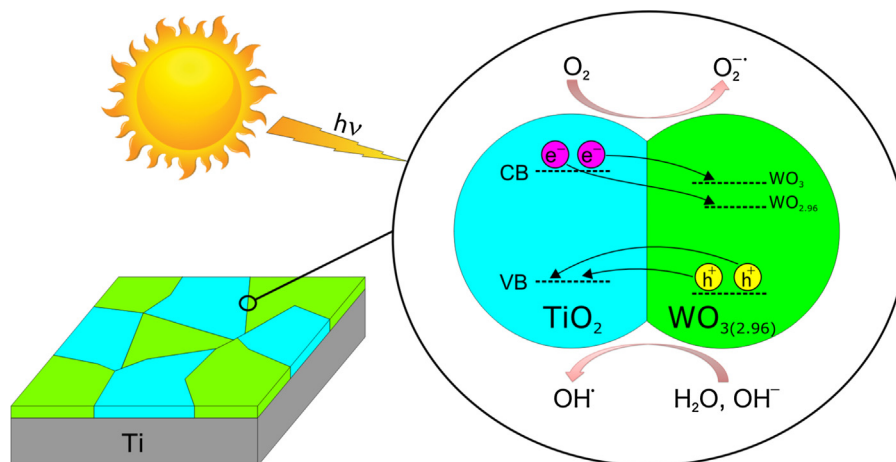


**Fig. 9.** Schematic diagram of electron-hole pairs separation and proposed mechanism of photodegradation over  $\text{WO}_3/\text{TiO}_2$  photocatalysts.

populate polaron states [54], reducing on the other side the photocatalytic efficiency of the catalyst.

#### 4. Conclusion

WO<sub>3</sub>/TiO<sub>2</sub> composite and pure TiO<sub>2</sub> coatings have been prepared on titania substrates using facile and cost-effective PEO process. The structural, morphological, optical properties and chemical composition of these samples were investigated by different methods such as XRD, SEM, Raman, UV–vis diffuse reflectance spectroscopy and XPS. XRD and Raman analysis revealed that the coatings are mainly composed of monoclinic WO<sub>3</sub> and anatase TiO<sub>2</sub>. With increasing duration of PEO process the crystallinity of the samples was improved, the WO<sub>3</sub> phase become dominant and a certain amount of monoclinic WO<sub>2.96</sub> phase appeared. XPS analysis confirmed the XRD results and revealed the presence of OH-groups and adsorbed H<sub>2</sub>O on the surface of WO<sub>3</sub>/TiO<sub>2</sub> coatings. The increasing amount of WO<sub>3</sub>/WO<sub>2.96</sub> phase caused a decrease of optical band gap, i.e. shift from near UV to visible spectral region. The photocatalytic activity of WO<sub>3</sub>/TiO<sub>2</sub> samples has been measured by monitoring photodecolouration of two model pollutants in aqueous solution, R6G under visible and MB9 under UV light irradiation. The WO<sub>3</sub>/TiO<sub>2</sub> samples have shown enhanced photocatalytic activity compared to pure TiO<sub>2</sub> under the visible light irradiation. Slight decrease of photocatalytic activity under the visible light in the sample enriched with WO<sub>3</sub>/WO<sub>2.9</sub> phase can be ascribed to the occurrence of photochromism and/or small polaron formation. Under the UV light, the WO<sub>3</sub>/TiO<sub>2</sub> photocatalysts have shown slightly better photocatalytic activity than pure TiO<sub>2</sub>. PL measurements demonstrated the correlation between photoactivity and the formation rate of OH• radicals under UV light irradiation, i.e. higher amount of OH• radicals formed, the better photoactivity of WO<sub>3</sub>/TiO<sub>2</sub> photocatalysts was achieved. The kinetics of the reaction in the case of both azo dyes followed the pseudo-first order. The degradation rate constant *k* of WO<sub>3</sub>/TiO<sub>2</sub> coatings under the visible light is almost five times higher than that of TiO<sub>2</sub>. Much better photocatalytic activity of the WO<sub>3</sub>/TiO<sub>2</sub> samples compared to pure TiO<sub>2</sub> in the visible range can be attributed to better light absorption, higher adsorption affinity and increased charge separation efficiency with increasing content of WO<sub>3</sub>/WO<sub>2.96</sub> phase.

#### Acknowledgements

This work was financially supported by the Ministry of Education, Science and Technological Development of the Republic of Serbia under the projects OI171032, III45018 and bilateral project Serbia-Italy No. RS13MO11.

#### References

- [1] L. Ren, Y. Li, J. Hou, X. Zhao, C. Pan, *ACS Appl. Mater. Interfaces* 6 (2014) 1608–1615.
- [2] F. Ruggieri, A.A. D'Archivio, M. Fanellia, S. Santucci, *RSC Adv.* 1 (2011) 611–618.
- [3] M. Šćepanović, B. Abramović, A. Golubović, S. Kler, M. Grujić-Brojčin, Z. Dohčević-Mitrović, B. Babić, B. Matović, Z.V. Popović, *J. Sol-Gel Sci. Technol.* 61 (2012) 390–402.
- [4] A. Golubović, B. Abramović, M. Šćepanović, M. Grujić-Brojčin, S. Armaković, I. Veljković, B. Babić, Z. Dohčević-Mitrović, Z.V. Popović, *Mater. Res. Bull.* 48 (2013) 1363–1371.
- [5] S. Watson, D. Beydoun, J. Scott, R. Amal, *J. Nanoparticle Res.* 6 (2004) 193–207.

- [6] A.N. Banerjee, *Nanotechnol. Sci. Appl.* 4 (2011) 35–65.
- [7] M. Xing, D. Qi, J. Zhang, F. Chen, *Chem. Eur. J.* 17 (2011) 11432–11436.
- [8] Y. Niu, M. Xing, J. Zhang, B. Tian, *Catal. Today* 201 (2013) 159–166.
- [9] F. Ruggieri, D. Di Camillo, L. Maccaroni, S. Santucci, L. Lozzi, *J. Nanopart. Res.* 15 (2013) 1–11.
- [10] W. M. Xing, Y. Li, J. Wu, X. Gong Zhang, *J. Phys. Chem. C* 115 (2011) 7858–7865.
- [11] M. Janus, B. Tryba, E. Kusiak, T. Tsumura, M. Toyoda, M. Inagaki, A.W. Morawski, *Catal. Lett.* 128 (2009) 36–39.
- [12] M. Takeuchi, M. Matsuoka, M. Anpo, *Res. Chem. Intermed.* 38 (2012) 1261–1277.
- [13] X. Chen, L. Liu, P.Y. Yu, S.S. Mao, *Science* 331 (2011) 746–750.
- [14] W. Fang, M. Xing, J. Zhang, *Appl. Catal. B: Environ.* 160–161 (2014) 240–246.
- [15] Y. Wang, J. Zhang, L. Liu, C. Zhu, X. Liu, Q. Su, *Mater. Lett.* 75 (2012) 95–98.
- [16] Y. Xiaodan, W. Qingyin, J. Shicheng, G. Yihang, *Mater. Charact.* 57 (2006) 333–341.
- [17] J. Rashid, M.A. Barakat, S.L. Pettit, J.N. Kuhn, *Environ. Technol.* 35 (2014) 2153–2159.
- [18] B. Gao, Y. Ma, Y. Cao, W. Yang, J. Yao, *J. Phys. Chem. B* 110 (2006) 14391–14397.
- [19] X. Luo, F. Liu, X. Li, H. Gao, G. Liu, *Mat. Sci. Semicon. Proc.* 16 (2013) 1613–1618.
- [20] N.R. Khalid, E. Ahmed, Z. Hong, M. Ahmad, Y. Zhang, S. Khalid, *Ceram. Int.* 39 (2013) 7107–7113.
- [21] Y. Li, P.C. Hsu, S.M. Chen, *Sensor. Actuat. B-Chem.* 174 (2012) 427–435.
- [22] K.K. Akurati, A. Vital, J.P. Dellemann, K. Michalowa, T. Graule, D. Ferri, A. Baiker, *Appl. Catal. B: Environ.* 79 (2008) 53–62.
- [23] D. Ke, H. Liu, T. Peng, X. Liu, K. Dai, *Mater. Lett.* 62 (2008) 447–450.
- [24] H. Song, H. Jiang, X. Liu, G. Meng, *J. Photoch. Photobio. A* 181 (2006) 421–428.
- [25] C. Shifu, C. Lei, G. Shen, C. Gengyu, *Powder Technol.* 160 (2005) 198–202.
- [26] F. Riboni, L.G. Bettini, D.W. Bahnemann, E. Selli, *Catal. Today* 209 (2013) 28–34.
- [27] J. Yang, X. Zhang, H. Liu, C. Wang, S. Liu, P. Sun, L. Wang, *Y. Liu Catal. Today* 201 (2013) 195–202.
- [28] S. Bai, H. Liu, J. Sun, Y. Tian, S. Chen, J. Song, R. Luo, D. Li, A. Chen, C.-C. Liu, *Appl. Surf. Sci.* 338 (2015) 61–68.
- [29] A. Rampaul, I.P. Parkin, S.A. O'Neill, J. DeSouza, A. Mills, N. Elliott, *Polyhedron* 22 (2003) 35–44.
- [30] J.H. Pan, W. In Lee, *Chem. Mater.* 18 (2006) 847–853.
- [31] M. Long, B. Tan, P. Hu, B. Zhou, Y. Zhou, *J. Mater. Chem. A* 3 (2015) 10195–10198.
- [32] J. He, Q. Luo, Q.Z. Cai, X.W. Li, D.Q. Zhang, *Mater. Chem. Phys.* 129 (2011) 242–248.
- [33] S. Stojadinović, N. Radić, R. Vasilic, M. Petković, P. Stefanov, Lj. Zeković, B. Grbić, *Appl. Catal. B: Environ.* 126 (2012) 334–341.
- [34] S. Petrović, S. Stojadinović, Lj. Rožić, N. Radić, B. Grbić, R. Vasilic, *Surf. Coat. Technol.* 269 (2015) 250–257.
- [35] T. Ohsaka, F. Izumi, Y. Fujiki, *J. Raman Spectrosc.* 7 (1978) 321–324.
- [36] Y. Djaoued, S. Balaji, N. Beaudoin, *J. Sol-Gel Sci. Technol.* 65 (2013) 374–383.
- [37] C. Santato, M. Odziemkowski, M. Ulmann, Jan Augustynski, *J. Am. Chem. Soc.* 123 (2001) 10639–10649.
- [38] E. Cazzanelli, C. Vinegoni, G. Mariotto, A.J. Purans, *Solid State Ionics* 123 (1999) 67–74.
- [39] Y. Yu, K. Lin, X. Zhou, H. Wang, S. Liu, X. Ma, *J. Phys. Chem. C* 111 (2007) 8971–8978.
- [40] A.O.T. Patrocínio, L.F. Paula, R.M. Paniago, J. Freitag, D.W. Bahnemann, *ACS Appl. Mater. Interfaces* 6 (2014) 16859–16866.
- [41] N. Ghobadi, *Int. Nano Let.* 3 (2013) 1–4.
- [42] K. Senthil, K. Yong, *Nanotechnology* 18 (2007) 395604 (1–7).
- [43] H. Ling, J. Lu, S. Phua, H. Liu, L. Liu, Y. Huang, D. Mandler, P.S. Lee, X. Lu, *J. Mater. Chem. A* 2 (2014) 2708–2717.
- [44] A.P. Shpak, A.M. Korduban, V.O. Medvedskij, *J. Electron. Spectrosc. Relat. Phenom.* 156–158 (2007) 172–175.
- [45] H.Y. Wong, C.W. Ong, R.W.M. Kwok, K.W. Wong, S.P. Wong, W.Y. Cheung, *Thin Solid Films* 376 (2000) 131–139.
- [46] A.A. Khodja, A. Boulkamh, C. Richard, *Appl. Catal. B: Environ.* 59 (2005) 147–154.
- [47] C.C. Wang, J.Y. Ying, *Chem. Mater.* 11 (1999) 3113–3120.
- [48] M.D. Hernández-Alonso, F. Fresno, S. Suarez, J.M. Coronado, *Energy Environ. Sci.* 2 (2009) 1231–1257.
- [49] M. Anik, T. Cansizoglu, *J. Appl. Electrochem.* 36 (2006) 603–608.
- [50] T.M. Su, Z.L. Liu, Y. Liang, Z.Z. Qin, J. Liu, Y.Q. Huang, *Catal. Comm.* 18 (2012) 93–97.
- [51] K. Ishibashi, A. Fujishima, T. Watanabe, K. Hashimoto, *Electrochem. Commun.* 2 (2000) 207–210.
- [52] H. Park, A. Bak, T.H. Jeon, S. Kim, W. Choi, *Appl. Catal. B: Environ.* 115–116 (2012) 74–80.
- [53] A.K.L. Sajjad, S. Shamaila, B. Tian, F. Chen, J. Zhang, *Appl. Catal. B: Environ.* 91 (2009) 397–405.
- [54] M.B. Johansson, G.A. Niklasson, L. Österlund, *J. Mater. Res.* 27 (2012) 3130–3140.

First International Conference

**PROCESSING, CHARACTERIZATION  
AND APPLICATION OF  
NANOSTRUCTURED MATERIALS AND  
NANOTECHNOLOGY**

**PROGRAMME  
&  
BOOK of ABSTRACTS**

*The Conference is organized within the scope of the FP7  
NANOTECH FTM project “Reinforcing of Nanotechnology  
and Functional Materials Centre” (No: 245916).*



FP7-REGPOT-2009-1



PP15

**An influence of La<sup>3+</sup>-dopant on anatase nanopowders synthesized by  
sol-gel and hydrothermal methods**

Natasa Tomić<sup>1</sup>, Aleksandar Golubović<sup>1</sup>, Marko Radović<sup>1</sup>, Jelena Tanasijević<sup>2</sup>,  
Ivana Veljković<sup>2</sup>

*Institute of Physics, University of Belgrade, Belgrade  
Innovation Center, Faculty of Technology & Metallurgy, University of Belgrade  
[natasat@ipb.ac.rs](mailto:natasat@ipb.ac.rs)*

Titanium dioxide (anatase) is very well known as the best photocatalyst due to its chemical stability, no toxicity and low cost. Anatase acts as photocatalyst under UV irradiation at around 360 nm ( $E_g = 3.2$  eV) by excitation of electrons at conduction band. Ion doping is an effective method to improve the properties of anatase by modifying its structure and microstructure which can result with band gap,  $E_g$ , decreasing. The lower band gap facilitates activation of anatase by light of higher wavelengths, desirable visible light irradiation. Besides, rare earth elements have larger radii than  $Ti^{4+}$ , they are mainly deposited onto surface of anatase so that way keep its large surface areas when heated at high temperatures. Nanopowders of pure and  $La^{3+}$ -doped  $TiO_2$  in anatase phase are synthesized by sol-gel and hydrothermal methods starting from  $TiCl_4$  as a precursor. The concentrations of  $La^{3+}$  dopants were 0.1, 0.3, 0.5 and 1 mol %. Structural properties of obtained nanopowders were analyzed by X-ray diffraction (XRD) while crystallite sizes and microstrains were calculated by Williamson-Hall method (WH). Spectroscopic ellipsometry method was used for optical properties determinations. Dielectric function of doped and undoped anatase samples has been investigated the dopant influence on the energy of different interband electronic transitions. Analyzed by spectroscopic ellipsometry in the energy range from 1.5-6 eV in order to influence of doping on anatase phase transition to rutile and thermal behaviour of prepared nanopowders was investigated using TG/DSC analysis. Obtained results from both methods of synthesis are compared and discussed.

**The Serbian Ceramic Society  
The Academy of Engineering Sciences of Serbia  
Institute for Multidisciplinary Research-University of Belgrade  
Institute of Physics-University of Belgrade  
Vinča Institute of Nuclear Sciences-University of Belgrade**

# **PROGRAMME AND THE BOOK OF ABSTRACTS**

**2<sup>nd</sup> Conference of The Serbian Ceramic Society**

**June 5-7, 2013  
Belgrade, Serbia  
2CSCS-2013**

Edited by:  
**Snežana Bošković  
Vladimir Srdić  
Zorica Branković**

O-3

**INVESTIGATION OF DEFECT ELECTRONIC STATES IN CeO<sub>2</sub> NANOCRYSTALS SYNTHESIZED BY SPRT, HYDROTHERMAL AND PRECIPITATION METHOD**

Marko Radović<sup>1</sup>, Bojan Stojadinović<sup>1</sup>, Nataša Tomić<sup>1</sup>, Ivana Veljković<sup>2</sup>,  
Sonja Aškračić<sup>1</sup>, Aleksandar Golubović<sup>1</sup>, Branko Matović<sup>3</sup>,  
Zorana Dohčević-Mitrović<sup>1</sup>

<sup>1</sup>*Institute of Physics, University of Belgrade, Belgrade, Serbia*

<sup>2</sup>*Institute for Multidisciplinary Research, University of Belgrade, Serbia*

<sup>3</sup>*Institute of Nuclear sciences "Vinča", University of Belgrade, Belgrade, Serbia*

The present work examines the influence of various synthesis methods on the formation of defect electronic states in the band structure of CeO<sub>2-y</sub> nanocrystals. Characterization of structural properties and determination of average crystallite size was performed using X-ray diffraction spectroscopy. Raman spectroscopy technique provides an insight into the concentration of oxygen vacancies and vibrational properties of ceria nanocrystals. Scanning tunneling microscopy and scanning tunneling spectroscopy measurements were performed on the CeO<sub>2-y</sub> nanocrystals and the measurements were compared with available literature data for the electronic band structure of cerium dioxide. The differences in defect electronic states within the band gap were detected among the differently prepared CeO<sub>2-y</sub> nanocrystals. Optical properties of CeO<sub>2-y</sub> nanocrystals were investigated by spectroscopic ellipsometry. Through the critical points analysis of ellipsometric data we were able to establish direct relationship between observed variations in electronic structure and optical transitions. This study revealed that synthesis process strongly influences the formation of different oxygen vacancy complexes which, on the other side, have dominant influence on optical, transport and magnetic properties of ceria based materials. In order to reach full potential of these materials it is of great importance to elucidate which type of synthesis process provides better ceria performances.

obtained. No obvious reflections that would indicate the existence of orthorhombic  $\text{YMnO}_3$  or other phases were detected. However, the TEM analysis indicates that small amount of o-YMO is present in the powder. Magnetic measurements show that  $T_N$  is 42 K, which suggests the presence of mixed valence manganese state in the obtained samples. The minor magnetic hystereses and very low coercive fields indicate that the samples are basically antiferromagnetic with weak ferromagnetism.

P-20

**THE EFFICIENCY OF PURE AND La-DOPED ANATASE  
NANOPOWDERS SYNTHESIZED BY SOL-GEL AND  
HYDROTHERMAL METHOD IN PHOTOCATALYTIC  
DEGRADATION OF ALPRAZOLAM**

Nataša Tomić<sup>1</sup>, Nina L. Finčur<sup>2</sup>, Ivana Veljković<sup>3</sup>, Maja Šćepanović<sup>1</sup>,  
Aleksandar Golubović<sup>1</sup>, Biljana Abramović<sup>2</sup>

<sup>1</sup>*Institute of Physics, University of Belgrade, Serbia*

<sup>2</sup>*Department of Chemistry, Biochemistry and Environmental Protection, Faculty  
of Sciences, University of Novi Sad, Serbia*

<sup>3</sup>*Institute for Multidisciplinary Research, University of Belgrade, Serbia*

Nanopowders of pure and  $\text{La}^{3+}$ -doped anatase were synthesized by sol-gel and hydrothermal methods. In both methods the hydrogel was synthesized by hydrolysis of  $\text{TiCl}_4$  at 0 °C. The doping of  $\text{TiO}_2$  was performed by using of  $\text{LaCl}_3 \cdot 7\text{H}_2\text{O}$  with 0.5 and 1 mol %. The sol-gel route involves the hydrogel conversion into its ethanol-gel, drying of obtained alcogel at 280°C and calcination at temperature of 550°C for 4 h. In hydrothermal method the hydrogel was placed in autoclave at 200°C for 24 h.

Structural properties of nanopowders were analyzed by X-ray diffraction (XRD) spectroscopy. Dependence of structural and morphological characteristics of nanopowders on synthesis methods and  $\text{La}^{3+}$  content is also investigated by the Raman spectroscopy. Very intensive modes observed in the Raman spectra of all nanopowder samples are assigned to anatase phase of  $\text{TiO}_2$ .

Synthesized nanopowders ( $1 \text{ mg cm}^{-3}$ ) were tested for their photocatalytic activity in the degradation of alprazolam ( $0.03 \text{ mmol dm}^{-3}$ ), a benzodiazepine derived from 1,4-benzodiazepine of new generation mainly used to treat anxiety disorders. Nanopowders synthesized by hydrothermal method showed a higher photocatalytic activity and a little dependence on the content of  $\text{La}^{3+}$ , in contrast to nanopowders synthesized by sol-gel method.



# BULLETIN

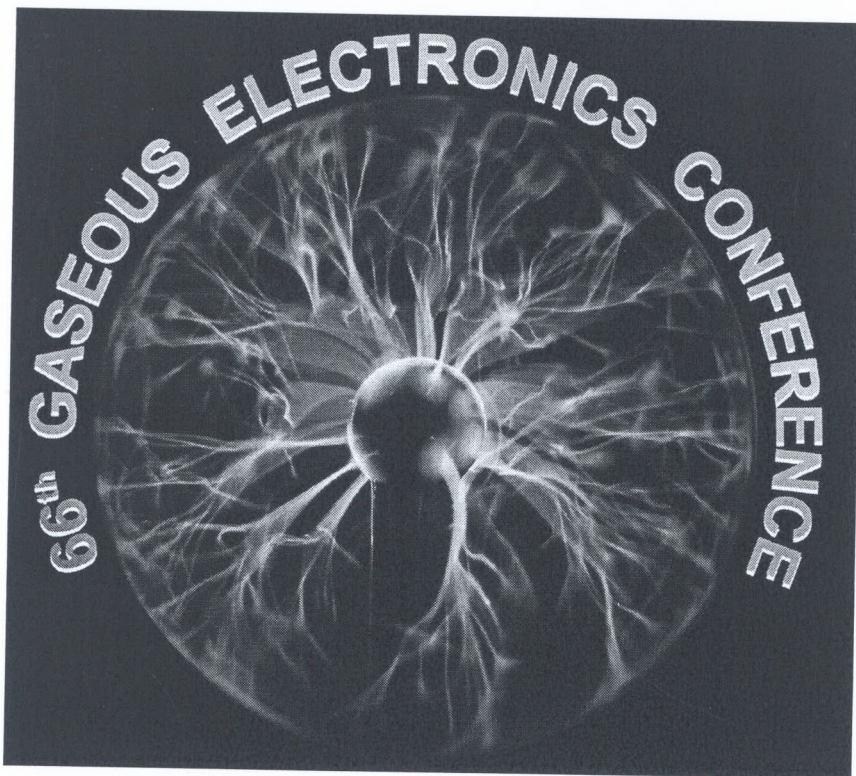
OF THE AMERICAN PHYSICAL SOCIETY

---

## 66th Annual Gaseous Electronics Conference

---

September–October, 2013  
Princeton, New Jersey



Volume 58, Number 8

APS  
physics™

either by increasing the production of specific species (like molecular hydrogen) or by decreasing pollutant emission. One typical issue observed in plasma assisted combustion is the increase of inflammability limits, i.e the observation of combustion and flame in situation where it is not observed in conventional combustion. To study the effect of a non-stationary discharge in flame generation and maintenance in a mixture for air and natural gas, the air mass flow rate was fixed in 0.80 g/s and the natural gas flow rate was varied between 0.02 and 0.14 g/s, resulting in a variation of equivalence ratio from 0.4 to 3.0. It is observed a dependence of inflammability limits with the applied power. The analysis by mass spectrometry indicates that the increase of inflammability limits with plasma is due not only applied power, but also to hydrogen production in the discharge. Visual analysis together with high speed camera measurements show a modification in spatial distribution of the flame, probably due to modifications both in flow velocity and flame velocity.

\*Supported by FAPESP PRONEX project grant 11/50773-0.

**CT1 68 Decolorization of azodyes using the atmospheric pressure plasma jet\*** SASA LAZOVIC, DEJAN MALETIC, NATASA TOMIC, GORDANA MALOVIC, *Institute of Physics, University of Belgrade, Serbia* UROS CVELBAR, *Jozef Stefan Institute, Ljubljana, Slovenia* ZORANA DOHCEVIC-MITROVIC, ZORAN LJ. PETROVIC, *Institute of Physics, University of Belgrade, Serbia* Atmospheric pressure plasma jet operated in air/argon mixture is tested for decolorization of Bezactiv Orange V-3R dye used in the textile industry. The decolorization efficiency is determined by spectrophotometric measurements at 493.7 nm which corresponds to the breaking of dye N=N bond. The initial concentration of 50 mg/L of dye is reduced 50 times after 120 minutes of treatment by plasma. The results are compared to the efficiency of the suspended TiO<sub>2</sub> powder and activated by an UV lamp (300 W). The radicals responsible for removal of the dye are OH and super-anion radical. It is found that efficiency of the plasma and TiO<sub>2</sub>+ UV is quite similar for the treatment times up to 60 min. After that, TiO<sub>2</sub> shows higher decolorization rates (100 times reduction after 90 min). However, when plasma and TiO<sub>2</sub> (but without the UV lamp) are applied together, it is found that there are synergetic effects and that the efficiency is increased. Plasma (less than 2 W) is not expected to produce high amounts of UV light in the atmospheric pressure.

\*Supported by MESTD, RS, III41011 and ON 171037.

**CT1 69 Numerical modeling of CF<sub>4</sub> decomposition in low pressure inductively coupled plasma: influence of the O<sub>2</sub> concentration** MAHSA SETAREH, *University of Tehran* University of Antwerp MORTEZA FARNIA, ALI MAGHARI, *University of Tehran* ANNEMIE BOGAERTS, *University of Antwerp* Perfluorinated compounds (PFCs), which are stable and difficult to decompose, are widely utilized in microelectronic manufacturing. The global warming potential of PFCs is so high in comparison with CO<sub>2</sub> that finding a solution for abating PFC emission is crucial. For this purpose, we performed a numerical simulation of the CF<sub>4</sub> decomposition in an inductively coupled plasma reactor with radio frequency power supply, which is used in semiconductor chamber cleaning process. A zero dimensional modeling code Global\_kin developed by Kushner is applied to model the reaction set of CF<sub>4</sub>/O<sub>2</sub> in typical plasma reactor conditions, such as 2kW power with frequency of 4 MHz, a pressure of 600 mTorr, and a typical residence time of 0.25 s. The model predicts that the reaction products of

the CF<sub>4</sub> decomposition are mostly COF<sub>2</sub>, CO<sub>2</sub> and CO. COF<sub>2</sub> is a toxic compound, but it can be hydrolyzed easily into HF and CO<sub>2</sub> using the scrubber in the reactor. By carefully altering the ratio between CF<sub>4</sub>/O<sub>2</sub>, the optimum ratio of the CF<sub>4</sub>/O<sub>2</sub> gas mixture can be achieved, leading to more than 80% of CF<sub>4</sub> decomposition. The numerical modeling results for CF<sub>4</sub> decomposition are validated based on experimental data from literature.

**CT1 70 Plasmas in conducting solutions for treatment of contaminated water** COLIN KELSEY, BILL GRAHAM, *Centre for Plasma Physics, Queens University of Belfast* AHMAD MASHAL, DAVID ROONEY, ROBERT GAMEZ SANS, *School of Chemistry and Chemical Engineering, Queens University of Belfast* A plasma produced in a conducting liquid is compared with more conventional advanced oxidation processes currently used in wastewater treatment such as the Fenton Process. The plasma was produced using a four electrode setup with driving circuitry producing 100 kHz bipolar square waves of approximately 300 V. We compare the effectiveness of the two processes by comparing the reduction in chemical oxygen demand achieved by each. Results indicate that for treatment times of 40 seconds our bench system can achieve a 50% COD reduction across a wide range of input COD concentrations, which is better than the reduction achieved by the single dose Fenton treatment process. Using electrical measurements the efficiency of the plasma process is determined to enable initial estimates of the feasibility of the process for industrial use. Chemical measurements on the plasma system are used to gain insight into the mechanisms underlying the process. These measurements include hydrogen peroxide production rate, which was determined to be 0.5 mg per minute, pH change, which increases with time, but tended to values of 1-3 pH units for characteristic treatment times, and temperature.

**CT1 71 Optimization of Industrial Ozone Generation with Pulsed Power** JOSE LOPEZ, DANIEL GUERRERO, ALFRED FREILICH, *Seton Hall University* LUCA RAMOINO, *Degremont Technologies - Ozonia* SETON HALL UNIVERSITY TEAM,\* DEGREMONT TECHNOLOGIES - OZONIA TEAM† Ozone (O<sub>3</sub>) is widely used for applications ranging from various industrial chemical synthesis processes to large-scale water treatment. The consequent surge in world-wide demand has brought about the requirement for ozone generation at the rate of several hundreds grams per kilowatt hour (g/kWh). For many years, ozone has been generated by means of dielectric barrier discharges (DBD), where a high-energy electric field between two electrodes separated by a dielectric and gap containing pure oxygen or air produce various microplasmas. The resultant microplasmas provide sufficient energy to dissociate the oxygen molecules while allowing the proper energetics channels for the formation of ozone. This presentation will review the current power schemes used for large-scale ozone generation and explore the use of high-voltage nanosecond pulses with reduced electric fields. The created microplasmas in a high reduced electric field are expected to be more efficient for ozone generation. This is confirmed with the current results of this work which observed that the efficiency of ozone generation increases by over eight times when the rise time and pulse duration are shortened.

\*Department of Physics, South Orange, NJ, USA.

†Research & Development, Dubendorf, Switzerland.

**CT1 72 Plasma Acid Formation from the Interaction of a Gliding Arc Plasmatron and Water** RYAN ROBINSON, *A.J. Drexel Plasma Institute, Mechanical Engineering & Mechanics, Drexel*

*3<sup>rd</sup> Conference of The Serbian Society for Ceramic Materials*

---

**The Serbian Society for Ceramic Materials  
The Academy of Engineering Sciences of Serbia  
Institute for Multidisciplinary Research-University of Belgrade  
Institute of Physics-University of Belgrade  
Vinča Institute of Nuclear Sciences-University of Belgrade**

# **PROGRAMME AND THE BOOK OF ABSTRACTS**

**3<sup>rd</sup> Conference of The Serbian Society for  
Ceramic Materials**

**June 15-17, 2015  
Belgrade, Serbia  
3CSCS-2015**

Edited by:  
**Branko Matović  
Zorica Branković  
Dušan Bućevac  
Vladimir V. Srdić**

P-14

## EFFICIENT PHOTOCATALYTIC DEGRADATION OF AZO-DYE RO16 BY PURE AND Eu-DOPED Pr(OH)<sub>3</sub> NANOSTRUCTURES

Nataša Tomić<sup>1</sup>, Sonja Aškračić<sup>1</sup>, Vinicius Dantas de Araújo<sup>2</sup>,  
Marijana Milićević<sup>1</sup>, Saša Lazović<sup>1</sup>, Zoran Petrović<sup>1</sup>,  
Zorana Dohčević-Mitrović<sup>1</sup>

*Institute of Physics, University of Belgrade, 11080 Belgrade, Serbia*  
*Instituto de Física, Universidade de São Paulo-USP, 13560-970, São Carlos-  
SP, Brasil*

Mixed nanorods/nanopowders of pure Pr(OH)<sub>3</sub> and doped with Eu<sup>3+</sup> (1, 3, and 5 mol %) were synthesized by microwave-assisted hydrothermal method. The oxides Pr<sub>6</sub>O<sub>11</sub> and Eu<sub>2</sub>O<sub>3</sub> were dissolved in aqueous HNO<sub>3</sub> and used as the precursors.

Structural properties of synthesized nanomaterials were analyzed by X-ray diffraction (XRD) spectroscopy. The influence of Eu<sup>3+</sup> content on structural and morphological characteristics of nanorods/nanopowders was also investigated by Raman spectroscopy and Field Emission Scanning Electron Microscopy (FESEM).

Synthesized nanostructures were tested for photocatalytic degradation of azo-dye Reactive Orange 16 since azo-dyes belong to the most toxic ones among various types of dyes. Eu-doped Pr(OH)<sub>3</sub> nanostructures showed very good photocatalytic performances, higher than pure Pr(OH)<sub>3</sub>.

P-15

## PREPARATION OF CARBONACEOUS MICROSPHERES BY HYDROTHERMAL TREATMENT OF FRUCTOSE WITH PHOSPHORIC ACID AND DIAMETER SIZE COMPARISON

Sanja Krstić<sup>1</sup>, Branka Kaluđerović<sup>1</sup>, Vladimir Dodevski<sup>1</sup>,  
Anđelika Bjelajac<sup>2</sup>

<sup>1</sup>*Institute of Nuclear Sciences Vinča, Laboratory for Material Science,  
University of Belgrade, P.O.B. 522, Mike Alasa 14, 11001 Belgrade, Serbia*  
<sup>2</sup>*Faculty of Technology and Metallurgy, University of Belgrade, Karnegijeva 4,  
P.O.B, 3503, 11001 Belgrade, Serbia*

Carbonaceous microspheres have been prepared by hydrothermal treatment of fructose. Parameters such as concentration of carbohydrate, reaction time, treatment temperature and concentration of phosphoric acid have been changed. Obtained